Exploring the stellar populations and the star formation history of the Carina OB1 association

Christiane Justine Göppl

München 2026

Exploring the stellar populations and the star formation history of the Carina OB1 association

Christiane Justine Göppl

Dissertation
an der Fakultät für Physik
der Ludwig–Maximilians–Universität
München

vorgelegt von
Christiane Justine Göppl
aus München

München, den 13.01.2026

Erstgutachter: Prof. Dr. Thomas Preibisch
Zweitgutachter: Prof. Dr. Andreas Burkert
Tag der mündlichen Prüfung: 25.02.2026

CONTENTS

LIST OF FIGURES

LIST OF TABLES

ZUSAMMENFASSUNG

Die meisten Sterne werden als Mitglieder von Sternhaufen und -assoziationen geboren. Eine Charakterisierung dieser Regionen ist demnach notwendig, um mehr über die Umgebungen zu lernen, in denen Sterne entstehen. Insbesondere Informationen über die genauen Positionen von massereichen Sternen sind von Bedeutung, da diese die Entwicklung und Entstehung von Sternen mit geringer Masse, protoplanetaren Scheiben und Exoplaneten beeinflussen. Eine der prominentesten Regionen, in der Sternentstehung heute stattfindet, ist die Carina-OB1-Assoziation. In dieser Arbeit werde ich eine detaillierte Charakterisierung der Car OB1-Assoziation über ihre vollständige räumliche Ausdehnung von $5^\circ \times 5^\circ$ durchführen, die die Sternhaufen und eine massereiche Sternpopulation beinhaltet, und ein Szenario für die Sternentstehungsgeschichte der Assoziation vorstellen.

Zuerst führen wir eine unvoreingenommene Suche nach stellaren Haufen und Gruppen innerhalb der Assoziation durch, indem wir einen Clustering-Algorithmus auf die astrometrischen Daten der Sterne in der *Gaia* DR3-Durchmusterung anwenden. Wir klassifizieren Haufen und Gruppen als Assozationsmitglieder, wenn ihre Distanz und ihr Alter mit Car OB1 kompatibel sind, und finden insgesamt 15 stellare Haufen und Gruppen, die diesen Kriterien entsprechen.

Um die Größe der geclusterten und verteilten Populationen zu quantifizieren, stellen wir zunächst einen Katalog massereicher Sterne zusammen, die spektroskopisch bestätigt wurden, und erweitern diesen, indem wir nach massereichen Sternkandidaten suchen. Dafür kombinieren die astrometrischen Daten mit der stellaren astrophysikalischen Parametertabelle von *Gaia* DR3 und wählen alle Sterne mit einer kompatiblen Distanz in der Car OB1-Region aus, wodurch der bisher größte Katalog massereicher Sterne in Car OB1 mit 770 OB-Sternen und 604 neuen OB-Sternkandidaten entsteht. Da 74% der massereichen Sterne Teil der verteilten Population sind, stellt dies einen signifikanten Anstieg von bisher ermittelten Anteilen von $\approx 50\%$ dar.

Unter Verwendung der exakt ermittelten Positionen, Distanzen und Bewegungen der Sternhaufen ist es uns möglich, das erste Sternentstehungsszenario für die gesamte Assoziation zu erstellen. Wir verfolgen die Sternhaufenposition über die letzten 13 Myr zurück und

berechnen anhand der Extrapolation aus der IMF der älteren Sternhaufen, wie viele Supernovae bisher stattgefunden haben. Unsere Analyse lässt darauf schließen, dass der älteste Sternhaufen der Assoziation, NGC 3293, im Sagittarius-Carina-Spiralarm entstanden ist und die Superblase um NGC 3293 zur Entstehung der massereichen Sternhaufen Trumpler 14, 15 und 16 geführt hat.

ABSTRACT

Most stars are born as part of star clusters and associations. A characterization of these regions is therefore crucial to learn more about the environments in which stars form. In particular, knowledge about the exact positions of high-mass stars is of importance as these stars exert a strong influence on the evolution and formation of low-mass stars, protostellar disks, and exoplanets. One prominent region where star formation is still ongoing is the Carina OB1 association. In this thesis, I will provide a detailed characterization of the Car OB1 association over its full spatial extent of $5^\circ \times 5^\circ$, including its clusters and high-mass star population, and propose a formation scenario for the association.

We first carry out an unbiased search for stellar clusters and groups within the whole association by applying a clustering algorithm to the astrometric data of stars from the *Gaia* DR3 survey. We then classify the clusters and groups as members of the association if their distance and age are compatible with Car OB1, and find in total 15 stellar clusters and groups that fulfill the criteria.

To quantify the size of clustered and distributed high-mass populations, we first compile a sample of spectroscopically confirmed high-mass stars and then complement the sample by searching for high-mass star candidates. For this, we combine the astrometric data with the stellar astrophysical parameters table from *Gaia* DR3 and select all stars with compatible distances in the Car OB1 region, which results in the so far largest catalog of high-mass stars in Car OB1 with 770 OB stars and 604 new OB star candidates. As 74% of the high-mass are part of the distributed population, this fraction is a significant increase from previously determined values of $\approx 50\%$.

With accurate cluster positions, distances, and motions available, we can now construct the first star formation scenario for the entire association. We trace back the positions of the clusters over the last 13 Myr and calculate how many supernovae have already occurred based on the older clusters' IMF extrapolation. Our analysis suggests that the oldest cluster of the association, NGC 3293, was formed in the Sagittarius-Carina spiral arm and that its surrounding superbubble led to the formation of other massive clusters, Trumpler 14, 15, and 16.

CHAPTER 1

INTRODUCTION

1.1 Properties of star clusters

Most stars are born as part of stellar groups and clusters in star-forming regions. These regions contain molecular clouds, which constitute the building blocks for stars. A deeper understanding of star-forming regions allows for better constraints on how star-forming regions impact individual young stars and the evolution of their protoplanetary disks, which in turn influences the formation of exoplanets. In the following introduction, I will describe how stars and clusters form, the characteristics of stellar clusters, including their initial mass distribution, as well as the evolution of high-mass stars and their impact on their cluster environment.

1.1.1 Star formation

Star formation occurs in Giant Molecular Clouds (GMC), which mostly consist of hydrogen molecules at temperatures of $T \sim 10$ K and densities of $n > 10^3\,\mathrm{cm}^{-3}$. First, dense clumps ($\sim$ 1 pc) form in the GMC, which themselves contain even denser cores with sizes of ~ 0.1 pc and densities of $n > 10^5\,\mathrm{cm}^{-3}$ (Rosen et al., 2020). The cores collapse under self-gravity when their mass exceeds the critical mass.

This collapse proceeds initially isothermally, as the gravitational energy can be fully radiated away, but turns adiabatic as soon as the core becomes optically thick due to its increased density. The core temperature starts to increase, and once it reaches temperatures of ≈ 2000 K, a second isothermal phase sets in. In this phase, the gravitational energy is mostly used to dissociate hydrogen molecules, and the core temperature rises again once the dissociation process is complete. At core temperatures of $> 10^7$ K, hydrogen fusion in the protostellar core starts, and the star is born. The time of the protostellar phase depends on the mass of the star and ranges from $10^4 - 10^5$ yr for massive stars ($M > 8\,M_\odot$) to $> 10^6$ yr for stars with $M < 1\,M_\odot$. Massive stars, therefore, have a very short protostel-

lar phase and almost immediately start the hydrogen fusion in their core (Padmanabhan, 2001). The lower mass limit for stars is 0.08 $M_\odot$. Some of the most massive stars detected so far in our Galaxy are W51-57 in W51a with a mass of $\approx 120\,M_\odot$ (Bik et al., 2019) and η Carina in the Carina Nebula with a mass of $\approx 100\,M_\odot$ (Strawn et al., 2023).

1.1.2 Clusters and Associations

Clumps contain multiple cores, which collapse and form coeval stars. As the stars share position and proper motion properties, inherited from their natal molecular cloud, and have high densities, they constitute a stellar cluster.

The cluster is still embedded in gas at the beginning of its lifetime and is only visible in infrared light. After $1-2$ Myr, the gas in clusters is expelled by stellar feedback, such as the winds of high-mass stars, and the clusters transition to open clusters, becoming visible at optical wavelengths. As the potential well of the cluster is reduced, open clusters are expected to expand and dissipate over time due to galactic tidal forces (Krumholz et al., 2019). Most open clusters contain a few tens to a few thousand members and have ages in the range of $10^6 - 10^8$ yr (Padmanabhan, 2001).

OB associations are conglomerations of stars that consist of several O- and B-type stars and young stars. As they have low star densities ($< 0.1\,M_\odot\,\mathrm{pc}^{-3}$ pc), they are not gravitationally bound and are therefore expected to disperse over time. They often contain large amounts of substructure, including stellar groups and clusters (Wright et al., 2023).

1.1.3 Initial mass function

As low-mass cores are more numerous in clouds, more stars with lower masses are born than high-mass stars. Salpeter (1955) was the first to postulate a fit for the stellar mass distribution in a cluster, also called the initial mass function (IMF) or shortened as $\xi(M)$. Salpeter (1955) defined the IMF as a probability distribution following a power-law as

$$\xi(M) = \frac{\mathrm{d}N}{\mathrm{d}\,M} \propto M^{-\alpha} \tag{1.1}$$

and determined the exponent to be $\alpha = 2.35$ by fitting the power-law to observational data. The IMF is also often written in logarithmic form as

$$\xi(\log M) = \frac{\mathrm{d}N}{\mathrm{d}\log M} \propto M^{-\alpha'} \,\mathrm{with}\, \alpha' = \alpha - 1. \tag{1.2}$$

Figure 1.1 shows the Salpeter IMF in blue and compares it to more recently proposed IMF fits by Kroupa (2001) and Chabrier (2005). While the Salpeter IMF slope is still considered a good fit for stellar masses above $1\,M_\odot$, it heavily overestimates the number of stars in the low-mass regime. The Kroupa and Chabrier IMF agree well for stars with masses above the brown dwarf limit, but start to diverge more strongly for masses below, as the data for sub-stellar objects is incomplete due to observational limitations (Kroupa et al., 2013).

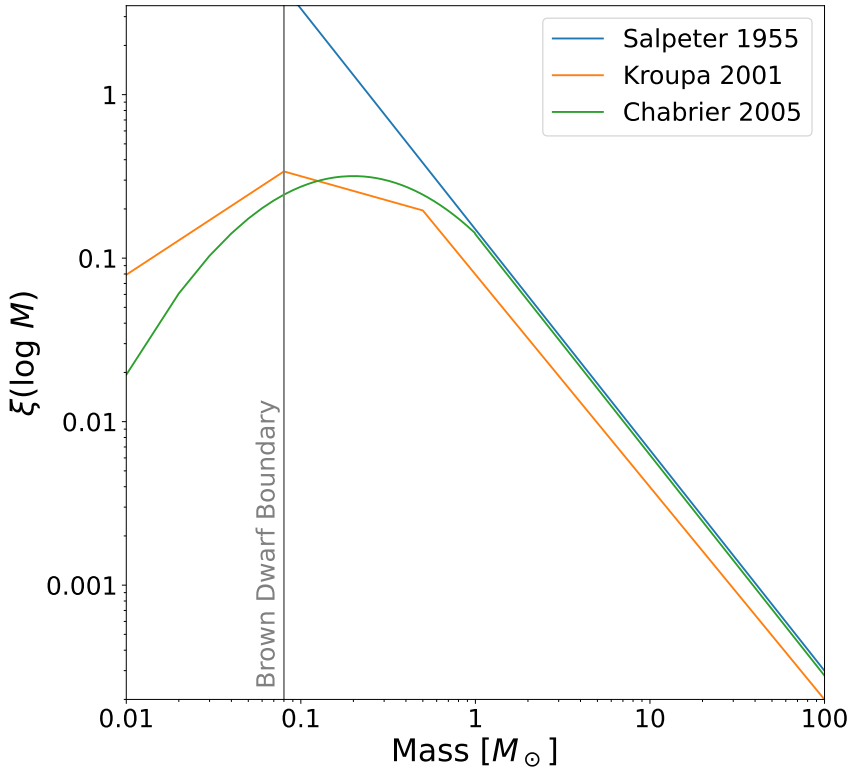

Figure 1.1: Comparison of IMF fits from different authors. The Kroupa (Kroupa, 2001) and Chabrier (Chabrier, 2005) IMFs are normalized.

For further analyses in this thesis, I will use the Kroupa IMF, which is defined as

$$\begin{aligned} \xi(M) &\propto M^{-0.3} && \text{for } 0.01 \leq M/M_\odot \leq 0.08 \\ &\propto M^{-1.3} && \text{for } 0.08 \leq M/M_\odot \leq 0.5 \\ &\propto M^{-2.3} && \text{for } 0.5 \leq M/M_\odot. \end{aligned} \tag{1.3}$$

The more massive a cluster, the higher is also the mass of its most massive star, $M_{*,max}$. As these quantities are related, Weidner et al. (2013) determined a fit for the $M_{*,max} - M_{cl}$ relation as

$$\begin{aligned} \log(M_{*,max}) &= a_0 + a_1 \log(M_{cl}) + a_2 \log(M_{cl})^2 + a_3 \log(M_{cl})^3 && \text{for } 3 \leq M_{cl}/M_\odot \leq 2.5 \times 10^5 \\ &= \log(150\, M_\odot) && \text{for } 2.5 \times 10^5 \leq M_{cl}/M_\odot \end{aligned} \tag{1.4}$$

where $a_0 = -0.66 \pm 0.18$, $a_1 = 1.08 \pm 0.22$, $a_2 = -0.150 \pm 0.075$, and $a_3 = 0.0084 \pm 0.0078$.

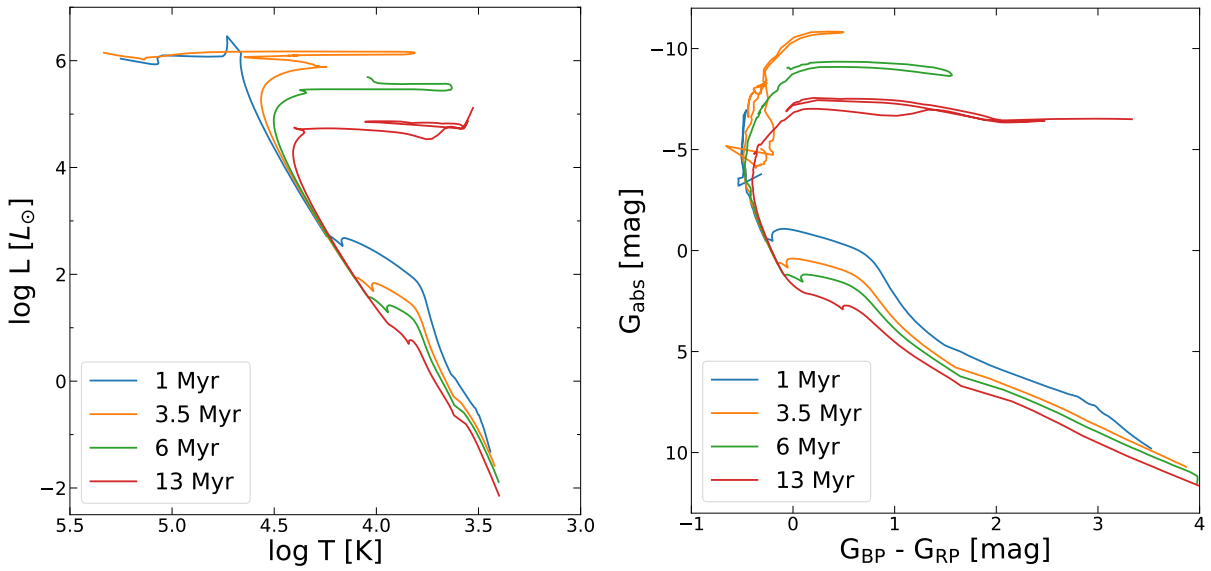

Figure 1.2: HRD and CMD for PARSEC v3.7 isochrones (Bressan et al., 2012) with ages of 1, 3.5, 6, and 13 Myr.

1.1.4 Lifetime of stars

The effective temperature and luminosity of stars are indicators of the star's evolutionary state. If both are plotted against each other, called a Hertzsprung-Russell diagram (HRD), it can be seen that most stars populate a thin line on the diagram, the Main Sequence. Figure 1.2 shows an example of an HRD on the left, with isochrones for ages of 1, 3, 6.5, and 13 Myr. Considering spectroscopic observations and fits are necessary to determine the luminosity and effective temperature of stars, color-magnitude diagrams (CMDs) are more commonly used to infer cluster ages, as the magnitude and color of stars can be directly observed (Mahy, 2026). An example for Gaia bands is shown in Fig. 1.2 on the right.

Stars spend most of their lifetime on the Main Sequence and fuse hydrogen to helium in their core during this phase. Stars with lower temperature and luminosity occupy the lower end of the sequence, and the temperature and luminosity of the stars increase along it. The differences in luminosity and temperature in stars arise from their difference in mass. More massive stars have a higher gravitational pressure in their core and therefore have to fuse more hydrogen to keep the hydrostatic equilibrium. While massive stars have more hydrogen available, they burn through it at a faster rate, and the star's mass and lifetime are therefore inversely correlated (Mahy, 2026). Parravano et al. (2003) determined the fit of the relation between a star's mass and its time on the Main Sequence as

$$
\begin{aligned}
t_{\mathrm{MS}}\,(\mathrm{Myr}) &\approx 7.65 \times 10^3\, M^{-2.80} && \text{for } 1.2 \leq M/M_\odot \leq 3 \\
&\approx 4.73 \times 10^3\, M^{-2.36} && \text{for } 3 \leq M/M_\odot \leq 6 \\
&\approx 2.76 \times 10^3\, M^{-2.06} && \text{for } 6 \leq M/M_\odot \leq 9 \\
&\approx 1.59 \times 10^3\, M^{-1.81} && \text{for } 9 \leq M/M_\odot \leq 12 \\
&\approx 7.60 \times 10^3\, M^{-1.57} + 2.30 && \text{for } 12 \leq M/M_\odot \leq 120.
\end{aligned}
\tag{1.5}
$$

When the stars run out of enough hydrogen to keep the hydrostatic equilibrium through hydrogen fusion, they move away from the Main Sequence. Their path beyond depends on the star's initial mass. Intermediate and low mass stars ($< 8\,M_\odot$) first evolve into giants, then into planetary nebulae, and then into white dwarfs, which is their final evolutionary state. More massive stars, on the other hand, evolve into supergiants and explode as supernovae, which either leave a neutron star or black hole as a remnant behind (Padmanabhan, 2001), which will be described in more detail in Sect. 1.2.

The spectral type alone is insufficient to describe a star's evolutionary state, as temperature and luminosity are degenerate. The spectral type is therefore complemented by the star's luminosity class, which uses the Roman numerals from I to V as notation. Main Sequence stars have the luminosity class V, while giants and supergiants are luminosity classes III and I, respectively. The lower the luminosity class number, the higher the star's luminosity (Mahy, 2026).

The position of a star on the color-magnitude diagram gives information about its evolutionary state. Combining the fact that stars in a cluster are formed at the same time and that more massive stars leave the Main Sequence earlier than lower mass stars, the point where stars turn off the Main Sequence can be used to determine the age of a cluster. Based on theoretical stellar evolution models, it is possible to predict the curve at a fixed age, i.e., the isochrone, on which stars are located on the CMD (Mahy, 2026). Figure 1.2 on the right shows multiple isochrones at different ages. The higher the age of the isochrone, the lower the turnoff point as less massive stars leave the Main Sequence. It can also be seen that the isochrones differ for lower mass stars. As discussed in Sect. 1.1.1, the less massive a star is, the longer its protostellar phase lasts, during which a protostar follows the Hayashi tracks (Hayashi, 1961) on the CMD. Therefore, the older a cluster is, the more low-mass stars have reached the Main Sequence, which extends then to lower magnitudes.

While age determinations with CMDs work very well for older and isolated clusters, the situation becomes more difficult for younger clusters, which are still surrounded by molecular clouds. Unresolved binaries, extinction, and young stellar objects, which have not yet reached the Main Sequence, lead to scatter in the CMD, which impedes the age determination and can mimic age spreads (see, e.g., Preibisch, 2012, for a review).

1.2 Post Main Sequence evolution of high-mass stars

As described in Sect. 1.1.3, low-mass stars are much more ubiquitous than high-mass stars. But while only $\approx 0.6\%$ of stars in a cluster have masses higher than $8\,M_\odot$, these stars contain $\approx 21\%$ of the stellar cluster mass. O- and early B-type stars strongly impact the cluster and its evolution through winds and radiation during their lifetime, and through supernovae at the end. All these influences can either trigger or suppress further star formation, depending on the surroundings of the high-mass star. The more massive a star is, the shorter its protostellar phase as well as its Main Sequence lifetime. While stars with $M \geq 8\,M_\odot$ end their life as supernovae, they do not all follow the same evolutionary path to that point. Ekström & Georgy (2025) list the evolutionary sequence based on the star's initial mass as follows:

$$
\begin{aligned}
M \geq 60\,M_\odot: &\quad \text{O} \rightarrow \text{Of/WR} \rightarrow \text{LBV} \rightarrow \text{WR} \rightarrow \text{SN} \\
M \approx 40 - 60\,M_\odot: &\quad \text{O} \rightarrow \text{BSG} \rightarrow \text{LBV} \rightarrow \text{WR} \rightarrow \text{SN} \\
M \approx 30 - 40\,M_\odot: &\quad \text{O} \rightarrow \text{BSG} \rightarrow \text{RSG} \rightarrow \text{WR} \rightarrow \text{SN} \\
M \approx 25 - 30\,M_\odot: &\quad \text{O} \rightarrow (\text{BSG}) \rightarrow \text{RSG} \rightarrow (\text{YSG? LBV?}) \rightarrow \text{SN} \\
M \approx 8 - 25\,M_\odot: &\quad \text{O/B} \rightarrow \text{RSG} \rightarrow (\text{Cepheid loop}) \rightarrow \text{RSG} \rightarrow \text{SN}.
\end{aligned}
$$

where BSG stands for blue supergiant, RSG for red supergiant, LBV for luminous blue variable, WR for Wolf-Rayet stars, Of stars for O stars with pronounced emission lines, and SN for supernova.

1.2.1 Supergiants

As stars evolve from the Main Sequence, they start burning helium in their core. This leads to an increase in the stellar radius, which gives these stars the name giants. Massive stars evolve into very luminous and hot giants, which earned them the title supergiants and are given the luminosity class I. In this phase, stars undergo strong mass loss (Patrick, 2026).

Supergiants are sorted into categories based on their color and can be blue, yellow, or red supergiants. Blue supergiants (BSGs) have the spectral type B, yellow supergiants (YSGs) have spectral types between A and G, while red supergiants (RSGs) have spectral types K and M. While RSGs burn helium in their cores, BSGs and YSGs can be either a pre-RSG phase and fusion hydrogen or helium in their core, or be a post-RSG phase in a blue loop on the HRD (Patrick, 2026). More massive BSGs ($M \geq 40\,M_\odot$) can also directly transition to the LBV evolutionary state and skip the RSG phase.

1.2.2 Wolf-Rayet stars

Stars with initial masses larger than $30\,M_\odot$ evolve into Wolf-Rayet (WR) stars either after the supergiant phase or directly after the Main Sequence for even more massive stars

($\geq 60\,M_\odot$). WR stars show broad, strong emission lines, especially He II, in their spectra caused by powerful stellar winds driven by radiation pressure as the luminosity of the stars approaches the Eddington Limit. Classical WR stars have depleted their hydrogen and have high mass loss rates of $10^{-5} - 10^{-4}\,M_\odot\,\mathrm{yr}^{-1}$ (Shenar, 2026).

There are three types of WR stars: WN, WC, and WO stars, which are differentiated by their spectra. WN stars show strong helium and nitrogen lines, WC carbon lines, and WO oxygen lines (Shenar, 2026). As WR stars have their hydrogen envelope stripped, their helium layer is exposed, leading to strong helium lines appearing in the spectrum. As the mass loss continues, more outer layers of the stars are removed, and the very massive WR stars transition from WN to WC over to WO. Lower mass WR stars do not reach the WO phase and evolve into supernova after the WC phase (Ekström & Georgy, 2025; Shenar, 2026).

1.2.3 Luminous Blue Variables

Luminous blue variables (LBV) are a post Main Sequence evolutionary stage, in which the stars are characterized by extreme mass-loss, which often happens as sporadic eruptions, and irregular variability (Smith, 2026). An extreme case and the best-studied LBV is η Carina. During its Great Eruption in the 19th century, the mass-loss rate reached up to $1\,M_\odot\,\mathrm{yr}^{-1}$ and its luminosity increased by a factor of ≈ 20 (Smith, 2014). The eruption led to the formation of a N-enriched bipolar shell around η Car (Smith, 2026), called the Homunculus, which can be seen in Figure 1.3.

1.2.4 Core-collapse supernovae

After a star has depleted the hydrogen in its core, it starts contracting, and pressure and temperature increase in the core until helium burning sets in. This phase lasts until helium is depleted and continues with carbon, neon, oxygen, and silicon until an iron core is formed.

As iron burning does not release energy, it cannot contribute to the radiation pressure to maintain the hydrostatic equilibrium, and the cycle cannot be continued. The core therefore contracts, and as soon as the temperature is high enough, photodisintegration sets in. This reduces the radiation pressure even further and leads to more contraction, which causes a runaway process. When the core exceeds the density threshold, it becomes incompressible due to strong force repulsion by degenerate neutron pressure, and rebounds. This leads to an outward pressure wave and an explosion, i.e., a supernova. During the explosion, a supernova releases energy of $\approx 10^{51}$ ergs and has a luminosity of $10^9\,L_\odot$, which is comparable to the brightness of a galaxy. The remnant of the inner core is either a neutron star or a black hole, if the core mass exceeds $3\,M_\odot$ (Jerkstrand et al., 2026).

The supernova creates a shock wave, which experiences four stages: free expansion phase, adiabatic expansion phase, snowplow phase, and merging phase. Initially, the shock expands freely with a nearly constant shock velocity of $> 10^4\,\mathrm{km\,s}^{-1}$ as the ejected material is much larger than the swept-up material. As soon as the mass of the swept-up material

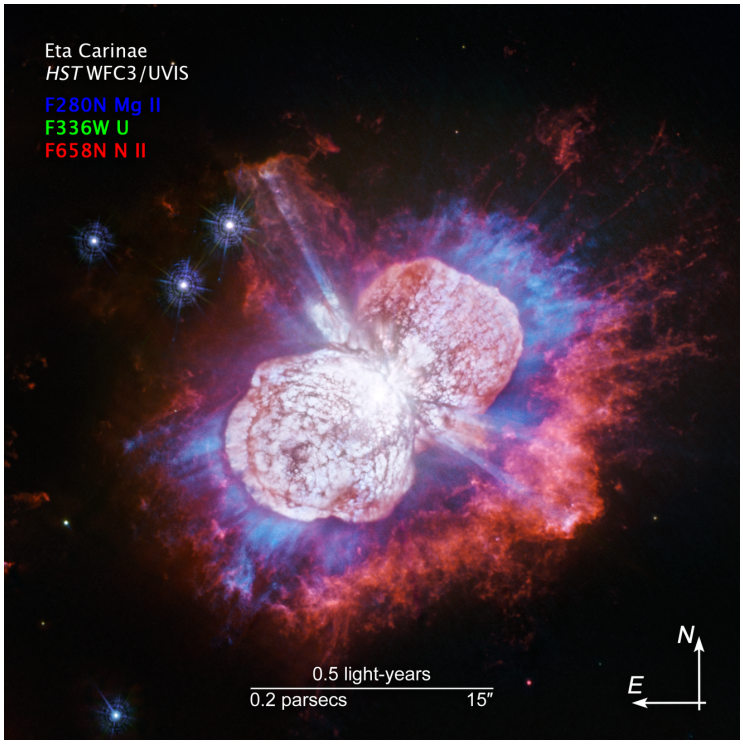

Figure 1.3: Color-composite of the homunculus around η Car. Image Credit: NASA, ESA, N. Smith (University of Arizona), and J. Morse (BoldlyGo Institute).

is non-negligible, the shock decelerates and enters the adiabatic phase. When the shock has slowed to a velocity of $\approx 200\ \mathrm{km\,s^{-1}}$, it has reached the slowplow or radiative phase. At this point, a dense shell is created behind the shock front, whose mass increases by the continuous sweeping-up of material. The shock wave continues to decelerate, and when the shock velocity is close to the environment's sound speed, the shock wave has reached its last phase, the merging phase, and dissipates (Bamba & Williams, 2022; Micelotta et al., 2018).

1.3 Influence of stellar feedback

As mentioned in Sect. 1.2, high-mass stars can suppress star formation. After high-mass stars are born, their stellar feedback leads to the expulsion of the residual gas in clusters, which stops the formation of new stars (Colín et al., 2013; Krumholz et al., 2019). Similarly, supernovae can lead to dispersal of their surrounding molecular clouds and prevent star formation (Iffrig & Hennebelle, 2015).

High-mass stars can also trigger star formation through three main modes: radiation, the expansion of an H II region (collect & collapse model), and superbubbles. These methods are described in more detail in the following text.

1.3.1 Triggered star formation

Radiation

One way to trigger star formation is through the ionization of the molecules in the clouds by the radiation from massive stars. The clouds are being irradiated, which leads to the exposure of the clumps inside as the gas surrounding them is getting ionized and blown away. The resulting ionization front then compresses the clump, which leads to star formation.

Figure 1.4 shows a sketch of triggered star formation over time, in which the high-mass stars are located above the cloud outside of the figure. In the first panel, the radiation from the massive stars creates an ionization front, which compresses the clumps in the pillar. They collapse under their self-gravity and form protostars, i.e., young stellar objects (YSOs). The stage gives information about its evolutionary stage, with Stage III YSOs being more evolved than Stage I YSOs.

In the second and third panels, the YSOs formed in the previous panels have now evolved to Stage II and III. They are starting to disperse, while the pillar has been even further eroded and accelerated by the ionization front from the massive stars, forming the next generation of new YSOs. This process continues until the pillar is completely dissipated (Smith et al., 2010; Posch et al., 2023).

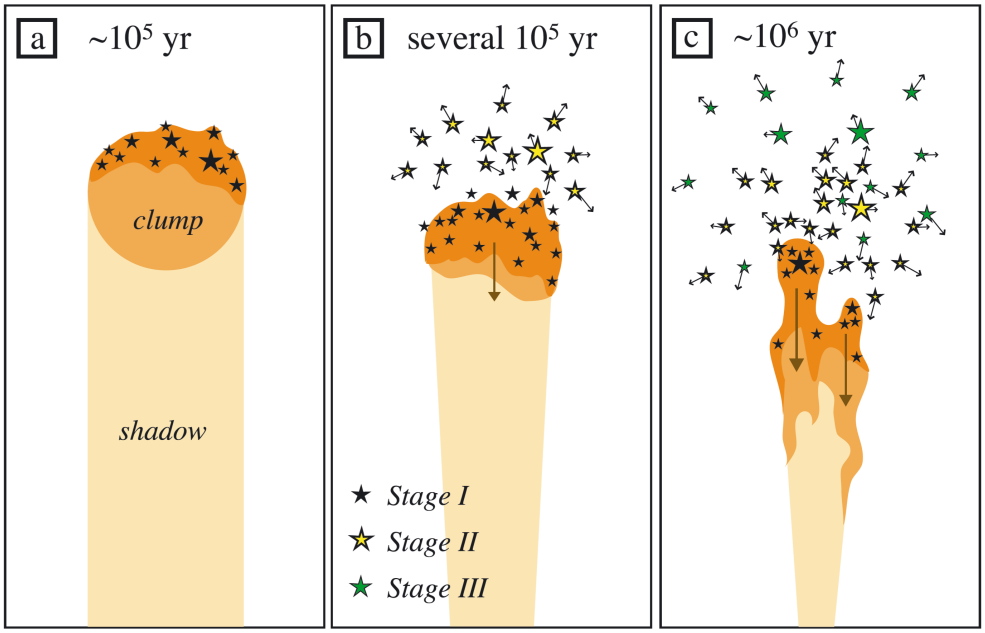

Figure 1.4: The sketch shows how radiation from massive stars can trigger star formation in the Southern Pillars of the Carina Nebula. Taken from Smith et al. (2010).

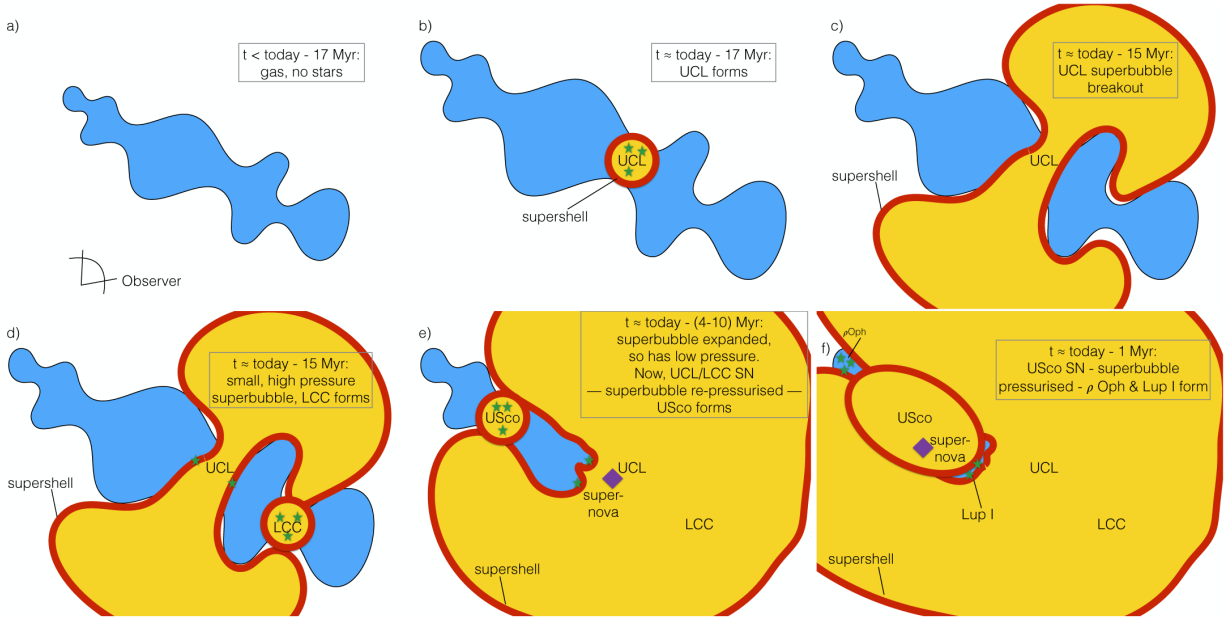

Figure 1.5: Sketch of the star formation scenario proposed for Sco-Cen through the "surround and squash" model. Taken from Krause et al. (2018).

Collect & collapse model

Another way massive stars can trigger star formation is through the expansion of H II regions caused by ionization fronts due to the radiation from massive stars. The ionization front drives the gas radially outwards from the stars, and an H II bubble is formed around the massive stars. This leads to the accumulation and compression of gas in dense shells as the bubble expands. The compressed gas then collapses under its own self-gravity, and stars are formed. This is called the "collect & collapse" model was first proposed by Elmegreen & Lada (1977). Today, this can be, e.g., seen in the H II region Gum 31 in the Carina Nebula Complex (CNC), where stars have formed at the outer edges of the H II bubble (Ohlendorf et al., 2013).

Superbubbles

A third way to trigger star formation is through superbubbles. Superbubbles are created by the stellar feedback of high-mass stars. Supernovae increase the pressure in the bubble, and the resulting dense shell of the superbubble can compress clouds and lead to the formation of stars. Multiple studies (see, e.g., Preibisch & Zinnecker, 1999; Krause et al., 2018) have suggested that superbubbles and their subsequent supernovae inside have triggered star formation in the Scorpius-Centaurus (Sco-Cen) OB association.

Figure 1.5 shows the sketch for a star formation scenario in Sco-Cen, in which a superbubble triggered star formation in Lower Centaurus Crux (LCC) and Upper Sco (USco). In this scenario, the superbubble is formed through the feedback of high-mass stars in Upper

Centaurus Lupus (UCL), and its pressure is increased by multiple supernovae. The superbubble expands and surrounds dense clouds, leading to their gravitational collapse and subsequent star formation. This is known as the "surround and squash" model (Krause et al., 2018).

1.3.2 FUV radiation

Two of the closest star-forming regions to us are Taurus and Sco-Cen. Both harbor multiple clusters at an average distance of ≈ 140 pc with individual molecular clouds with masses of about $10^3 - 10^4\,M_\odot$ and stellar clusters with $10 - 10^3$ member stars. The total stellar population is ≈ 500 stars for Taurus and $\approx 10^4$ stars for Sco-Cen (Zucker et al., 2020; Ratzenböck et al., 2023b; Posch et al., 2025; Luhman, 2018). Due to their small distance, these regions are ideally suited for observations of YSOs, as the substructure of their proto-planetary disks can be resolved. This has been done in the Disk Substructures at High Angular Resolution Project (DSHARP, see Andrews et al., 2018), in which 20 proto-planetary disks were observed with ALMA to resolve substructure and investigate how it affects planet formation. The most common substructures found were rings and gaps, with other disks also displaying spiral patterns and warps.

However, most stars are not born in low-irradiation regions like Taurus or Sco-Cen. Figure 1.6 shows the number of member stars in a star-forming region versus its overall FUV luminosity, while the color-coding visualizes the relative fraction of stars formed within such a star-forming region. It demonstrates that most stars are born in regions with a high member count and strong FUV luminosity and that fewer than 1% of stars are born in low-irradiation regions similar to Taurus. Instead, a large fraction of stars are born in regions with $10^4 - 10^5$ member stars and much higher FUV luminosity, like NGC 6357, the Carina OB1 association, or the cluster Westerlund 1.

The strong FUV luminosity field created by the emission of high-mass stars has a strong impact on protoplanetary disks. The photoevaporation leads to disk truncation, which in turn influences the chemical evolution of the inner disk, and reduces the disk lifetime (Sellek et al., 2020). To study the effect of strong FUV irradiation on the evolution and chemistry of disks, Ramírez-Tannus et al. (2023) observed mid-infrared (IR) spectra of 15 proto-planetary disks with JWST in the young star-forming region NGC 6357 as part of the eXtreme UV Environments (XUE) program. The first disk to be analyzed was XUE 1, which is close to the binary Pismis 24 1 with spectral type O3.5 If*+O4 III(f+) (Sota et al., 2014) and has been exposed to FUV radiation field of $\approx 10^5\,G_0$ (Ramírez-Tannus et al., 2023). The results for eleven additional young (≈ 1 Myr) disks are presented in Ramírez-Tannus et al. (2025). Their analysis suggests that the XUE disks are likely truncated, as they show no signs of external irradiation, and that the chemical inventory of the observed irradiated inner disks is similar to that of non-irradiated inner disks. They have also observed hot water in most inner disks, suggesting that rocky planets can still be formed despite the high irradiation.

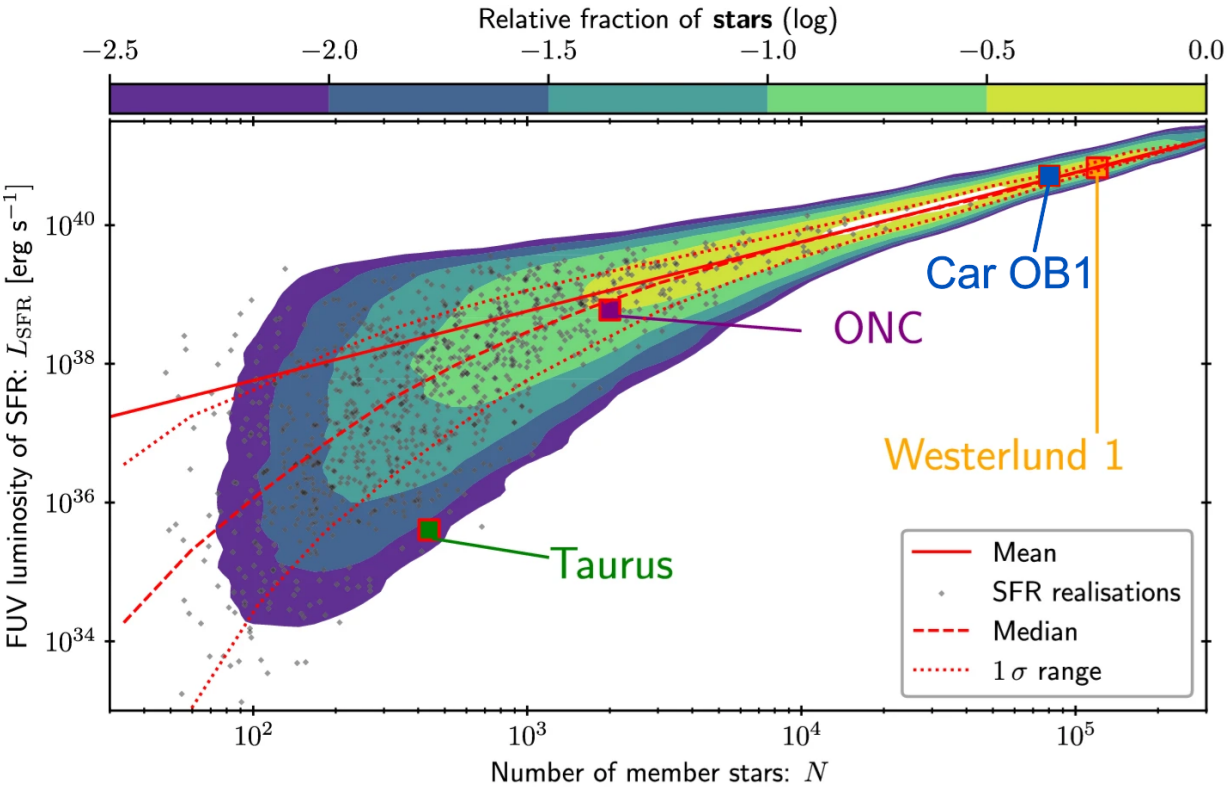

Figure 1.6: The number of member stars versus the FUV luminosity in a star-forming region, with the color bar showing the relative fraction of stars formed in the region. Taken from Winter & Haworth (2022) and modified by adding the Car OB1 association.

CHAPTER 2

THE CARINA OB1 ASSOCIATION

The Carina OB1 (Car OB1) association is one of the brightest star-forming regions on our night sky with a size of $\approx 5^\circ \times 5^\circ$. It is located in the Carina-Sagittarius arm of the galactic plane and contains numerous star clusters, at least 135 O-type and Wolf-Rayet stars, a total stellar population of $\approx 10^5$ stars (Feigelson et al., 2011; Göppl & Preibisch, 2025) and $\approx 10^6$ $M_\odot$ of dust and molecular clouds (Smith & Brooks, 2007; Preibisch et al., 2012).

The most prominent part of the Car OB1 association is the Carina Nebula with the famous star, η Carina, shown in Fig. 1.3. η Carina is one of the most massive and luminous stars in our Galaxy and part of the stellar cluster Trumpler 16 (Tr 16). Tr 16 and Tr 14 are the most massive clusters of the Nebula, with both hosting several O-type stars. The Carina Nebula, the H II region Gum 31, which hosts the cluster NGC 3324, and the cluster NGC 3293, constitute the Carina Nebula Complex (CNC). Figure 2.1 shows optical images of the five largest clusters in the CNC.

Mel'Nik & Efremov (1995) divided the Car OB1 into six subgroups based on the distribution of the stellar population, which extended Car OB1 beyond the CNC even further north-west up to the cluster IC 2581. The analysis of the cluster distances using *Gaia* DR3 revealed that IC 2581 has a compatible distance to the CNC (Göppl & Preibisch, 2025).

As Car OB1 is one of the most massive star-forming regions in our Galaxy, comparable to 30 Doradus in the Large Magellanic Cloud, but at a much closer distance, it is the perfect laboratory to study the influence of massive stars on their surroundings. The following chapter gives a brief overview of the multi-wavelength observations that have been done in the last decades of the Car OB1 association to study its young stellar population, along with their main results.

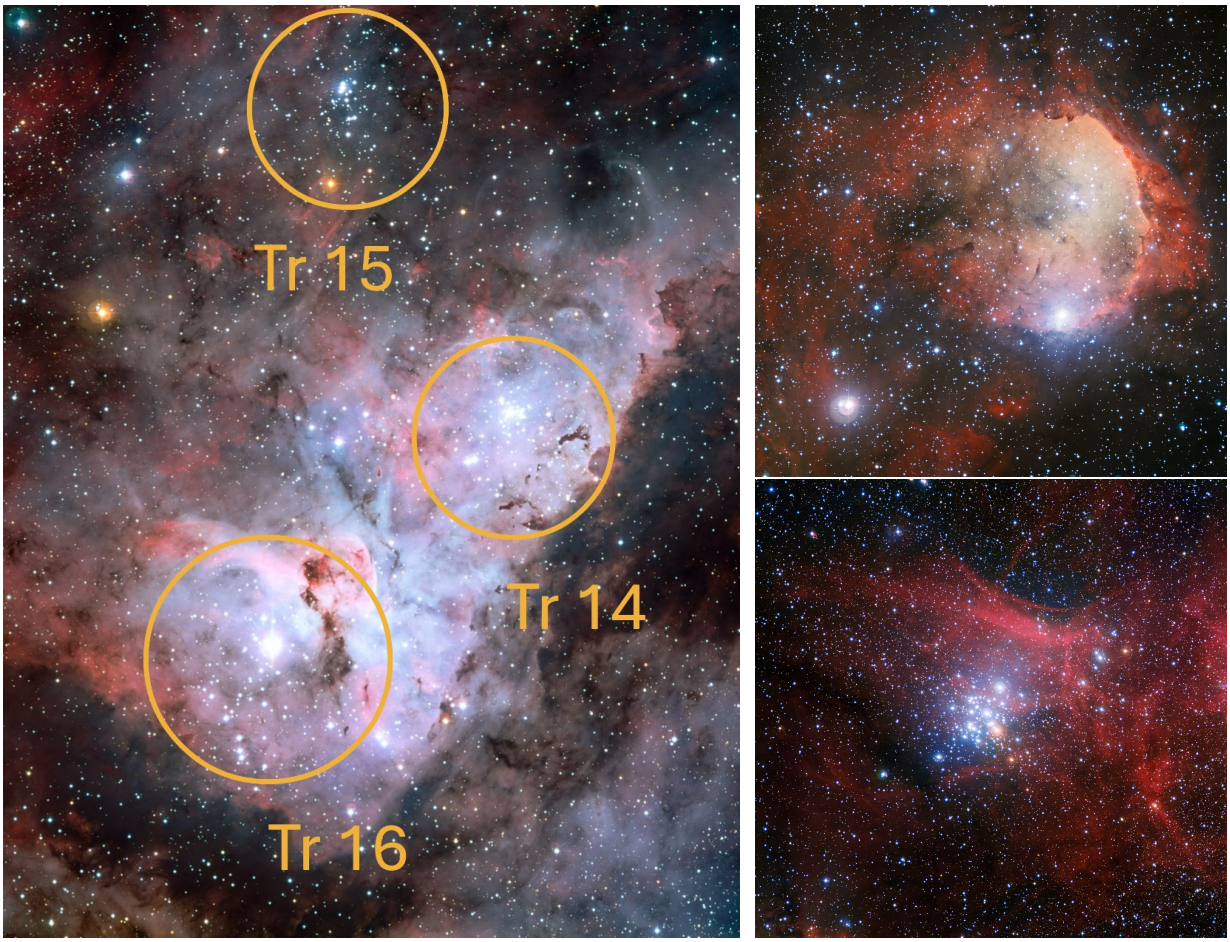

Figure 2.1: Optical color-composite images of clusters in Car OB1 taken with the Wide Field Imager (WFI) on the MPG/ESO 2.2-metre telescope. Left panel: The clusters Tr 14, 15, and 16 of the inner Carina Nebula are highlighted. The B and U bands are shown in blue, the V band in green, and the R band, S II emission, and Hα emission in red. The field of view is $0.43^\circ \times 0.55^\circ$. Top right panel: The image contains the H II region Gum 31 with the cluster NGC 3324. The V band is shown in blue, the O III emission in green, the R band in yellow, and the Hα emission in red. The field of view is $0.44^\circ \times 0.44^\circ$. Lower right panel: The image shows the cluster NGC 3293. The B band is shown in blue, the V band in green, the I band in orange, and the Hα emission in red. The field of view is $0.57^\circ \times 0.57^\circ$. North is up and east to the left in all three images. Image credits: ESO/G. Beccari.

2.1 The MSX survey

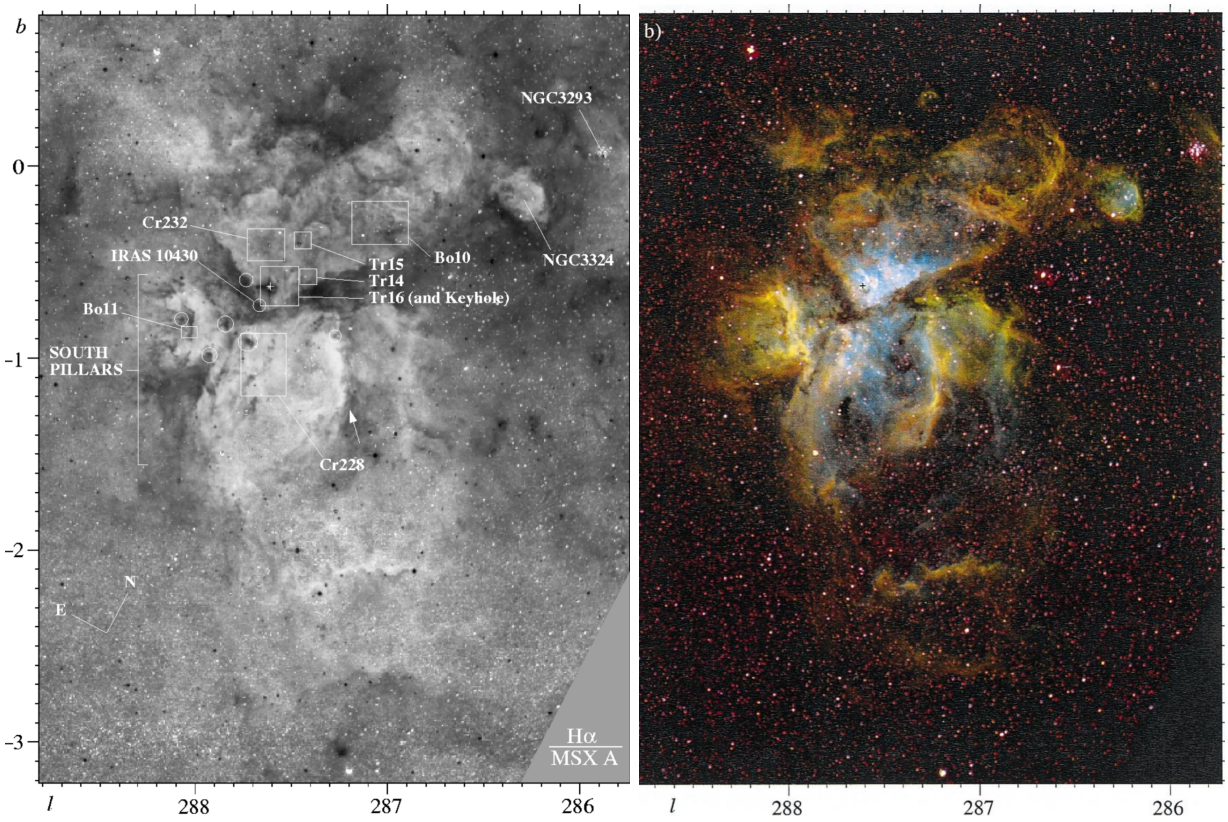

Figure 2.2: Left panel: image of the ratio between Hα and the MSX A band. Right panel: color-composite with O III emission in blue, Hα in green, and S II emission in red. Both images are taken from Smith et al. (2000).

Until the beginning of this century, observations of the inner part of the Carina Nebula indicated that it was an evolved H II region with no active star formation. The analysis of mid-IR observations from the Midcourse Space Experiment (MSX) satellite by Smith et al. (2000) challenged this assumption as they used observations of the full Carina Nebula and discovered embedded IR sources, which are signs of ongoing star formation. They discovered that most of the current star formation is happening at the outskirts of the Carina Nebula, while the bright center of the Carina Nebula is mostly devoid of star-forming activity (Smith & Brooks, 2008). This is illustrated in Fig. 2.2, where the right image shows an optical image from the Mount Stromlo and Siding Spring Observatories (MSSSO) Hα Survey, while the left image shows an ratio of between Hα (from MSSSO) and the MSX A band ($\Delta\lambda$ = 6.8–10.8 µm), in which the dark dots indicate compact IR sources out of which some are highlighted by circles. It can be seen that they mostly lie outside the bright center in the Southern Pillars, which are located south of Tr 16 and around clusters Bochum 11 (Bo 11) and Collinder 228 (Cr 228).

2.2 The *Spitzer* survey

Following the discovery of ongoing star formation, the Southern Pillars were observed in more detail using the Infrared Array Camera at the *Spitzer* space telescope at wavelengths of 3.6, 4.5, 5.8, and 8.0 µm. This can be seen in Fig. 2.3, which shows Spitzer IR observations (Smith et al., 2010) of the Southern Pillars. The image shows several dust pillars, which are sites of triggered star formation as described in Sect. 1.3.1. In total, there were 909 YSOs identified in the region based on their SEDs. Combining this with the IMF, Smith et al. (2010) extrapolated that the Southern Pillars host more than 5000 YSOs, which have formed over the last 3 Myr.

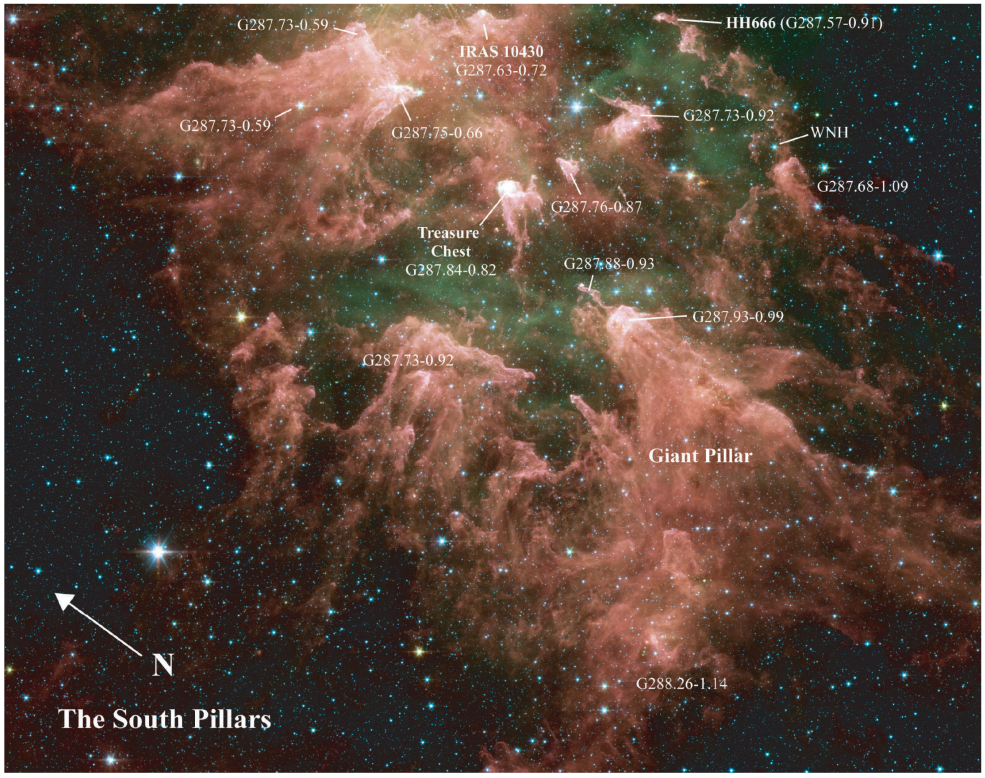

Figure 2.3: Color-composite image of the Southern Pillars at wavelengths of 3.6 µm (blue), 4.5 µm (green), 5.8 µm (orange), and 8.0 µm (red) taken by the *Spitzer* space telescope. The field of view is $1.3^\circ \times 0.9^\circ$. Taken from Smith et al. (2010)

2.3 The LABOCA survey

Sub-millimeter observations of the Carina Nebula were carried out using LABOCA at the APEX telescope (Preibisch et al., 2011c). A region of $1.25^\circ \times 1.25^\circ$ was observed at 870µm over a total time of $\approx$ 10h, and it revealed a total gas and dust mass of $\approx 60\,000\,M_\odot$. About 10% of the gas is in clouds, which are dense enough for star formation. As most

observed clouds in the sample have masses smaller than a few 1000 $M_\odot$, this suggests that they will most likely not form any high-mass stars.

2.4 The *Chandra* Carina Complex Project

The *Chandra* Carina Complex Project (CCCP, see Townsley et al., 2011b) was a X-ray survey of 1.4 square-degrees in the Carina Nebula. It consisted of 38 observations at 22 pointings with a total exposure time of 1.2 Megaseconds as shown in Fig. 2.4. In total, there were 14 368 individual X-ray sources detected in the field, out of which 10 714 were classified as likely Carina Nebula members based on their strong X-ray emission, which made it possible to differentiate them from extragalactic sources (Broos et al., 2011). This enabled the compilation of the first statistically complete sample of young stars in Carina, as samples from IR and optical observations contain stars from all ages, including fore- and background stars. While the X-ray observations detect stars down to 0.1 $M_\odot$, the sample is complete for masses above 1 $M_\odot$.

Further analysis of the distribution of the X-ray sources by Feigelson et al. (2011) revealed that the Carina Nebula hosts 20 clusters and 31 groups of X-ray detected stars, with the clusters Tr 14 and 15 showing a centrally concentrated distribution of their stellar populations, while the stellar distribution in Tr 16 is highly substructured, with the stars being divided into several subclusters. Combining the sample completeness down to 1 $M_\odot$ with the IMF, Feigelson et al. (2011) determined a total population of $\approx$ 104 000 young stars in the Carina Nebula.

2.5 The HAWK-I survey

Following this, Preibisch et al. (2011b) observed the inner part of the Carina Nebula, including the clusters Tr 14, 15, and 16, and the Southern Pillars, using the HAWK-I instrument at the VLT with a total exposure time of 14 h. Figure 2.5 shows a color-composite image of the inner Carina Nebula, a small part of the full observation. This survey revealed 600 000 individual IR sources down to 0.1 $M_\odot$ in a 0.36 square-degree area. As the clusters are strongly obscured, the observations with HAWK-I, which is able to detect sources at magnitudes down to $J \approx 23$, $H \approx 22$, and $K_s \approx 21$, made it possible to construct CMDs and constrain the ages of the individual clusters. This revealed that the clusters in the Carina Nebula are very young, with ages ranging from 1 Myr for Tr 14 and $3 - 4$ Myr for Tr 16 to $5 - 8$ Myr for Tr 15. Analysis of the young star population unveiled that their near-infrared excess fraction is lower than in quiescent star-forming regions, possibly due to the high levels of stellar feedback.

Combining the HAWK-I objects with the X-ray-selected CCCP objects made it possible to study the young stellar population more closely. This revealed that the classification of objects to be members of the Carina Nebula, which was done as part of the CCCP (Broos et al., 2011), suffered only from small contamination and that the IMF of the Carina Nebula

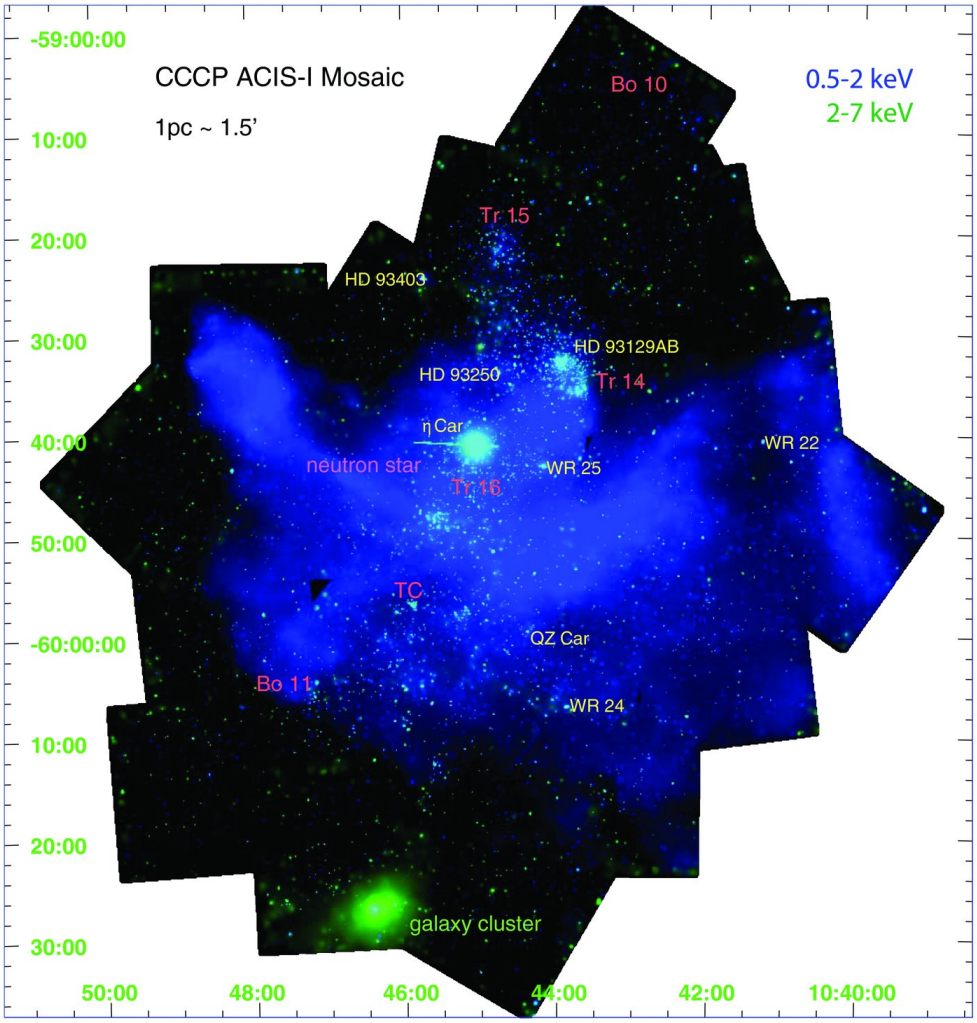

Figure 2.4: Observed mosaic of the Carina Nebula as part of the *Chandra* Carina Complex Project. The $0.5 - 2$ keV emission is shown in blue, the $2 - 7$ keV emission is shown in green. Taken from Townsley et al. (2011b).

is consistent with the field IMF (Preibisch et al., 2011a).

2.6 The *Herschel* survey

While the previous observations focused on the young stellar population of the Carina Nebula, the observations with the *Herschel* telescope aimed at characterizing the dust and clouds in the CNC, including the Carina Nebula and the cluster NGC 3324 with its H II region Gum 31 (Preibisch et al., 2012). The area spanning 5.3 square-degrees was mapped at far-IR (FIR) wavelengths ranging from 70 µm to 500 µm over an observation time of 6.9 h. The images at 70 µm, 160 µm, and 250 µm were taken to create a color-composite image

Figure 2.5: Color-composite image of the inner Carina Nebula taken by HAWK-I at the VLT using the J band (blue), H band (green), and K band (red). The field of view is $0.39^\circ \times 0.26^\circ$. The bright star at the bottom is η Car, and Tr 14 is visible to the north-west of it. North is up and east to the left. Image Credit: ESO/T. Preibisch.

of the Carina Nebula and Gum 31, as shown in Fig. 2.6. The observations revealed that the cloud morphology is dominated by the stellar feedback of high-mass stars. Preibisch et al. (2012) also concluded that the central 1 degree radius region has a total gas and dust mass of $\approx 650\,000 - 890\,000\,M_\odot$ including several cool clouds with masses of $\approx 10\,000\,M_\odot$ and column densities that are compatible with further star formation. An analysis of the Gum 31 region indicated signs of triggered star formation as stars have formed at the outer edges of the H II bubble (Ohlendorf et al., 2013), as described in Sect. 1.3.1.

2.7 The VISTA survey

The previously mentioned observations of the stellar population have so far focused on the inner part of the association, i.e., the Carina Nebula. The 4m Visible and Infrared Survey Telescope for Astronomy (VISTA) survey (Preibisch et al., 2014b) was the first near-IR (NIR) survey to cover the full spatial extent of the CNC. In the survey, over 3.9 million sources were detected in at least two bands down to magnitudes of $J \approx 21.2$, $H \approx 19.9$, and $K_s \approx 19.3$ over an area of 6.7 square-degrees. The survey is the first spatially complete IR observation of the stellar population down to 0.1 $M_\odot$ in the CNC. In-depth analysis of the 8781 YSO candidates in the CNC revealed that about half are part of the non-clustered, distributed population (Zeidler et al., 2016).

Figure 2.6: Color-composite image of the Carina Nebula and Gum 31 at wavelengths of 70 µm (blue), 160 µm (green), and 250 µm (red) taken by *Herschel*. The field of view is 2.1° × 2.3°. North is to the upper left and east to the lower left. Image Credit: ESA/PACS/SPIRE/T. Preibisch.

2.8 The *Chandra* survey of NGC 3324

Preibisch et al. (2014a) observed the H II region Gum 31 in the X-ray regime ($[0.5-8]$ keV) using *Chandra* with a total exposure time of ≈ 19.1 h. They detected 679 individual X-ray point sources with a completeness of 80% down to $1\,M_{\odot}$. Based on these results, they extrapolated a total population of 4000 young stars in Gum 31 and estimated an age of $1-2$ Myr for NGC 3324.

2.9 The *Chandra* survey of NGC 3293

Following the observations of NGC 3324, Preibisch et al. (2017) complemented these with *Chandra* X-ray observations of NGC 3293 over a total exposure time of ≈ 19.7 h. This revealed NGC 3293 to be one of the most populous clusters of the CNC aside from Tr 14 and Tr 16, as they detected 1026 individual X-ray sources and estimated a completeness of 90% down to masses of 1 $M_{\odot}$. At a determined age of ≈ 10 Myr, NGC 3293 is one of the oldest clusters in the complex. The X-ray observations of Gum 31 and NGC 3293 showed that a significant portion of the stellar population of the CNC resides outside the inner Carina Nebula.

2.10 The JWST survey of the Cosmic Cliffs

Figure 2.7: Color-composite image of the cosmic cliffs in NGC 3324 taken by the JWST NIRCam. The filters are assigned colors as F444W in red, F335M in orange, F470N in yellow, F200W in green, F187N in cyan, and F090W in blue. The field of view is 0.12° × 0.07°. North is to the lower right and east to the upper right. Image Credit: NASA, ESA, CSA, STScI.

Recent observations of the cosmic cliffs in NGC 3324 by the JWST NIRCam, see Fig. 2.7, show the edge of the H II region Gum 31 with multiple pillars and cavities visible, which are sites of ongoing star formation. Analyses of this area revealed several previously unknown outflows and Herbig-Haro objects (Reiter et al., 2022), and a significant amount of newly discovered YSO-candidates (Crompvoets et al., 2024).

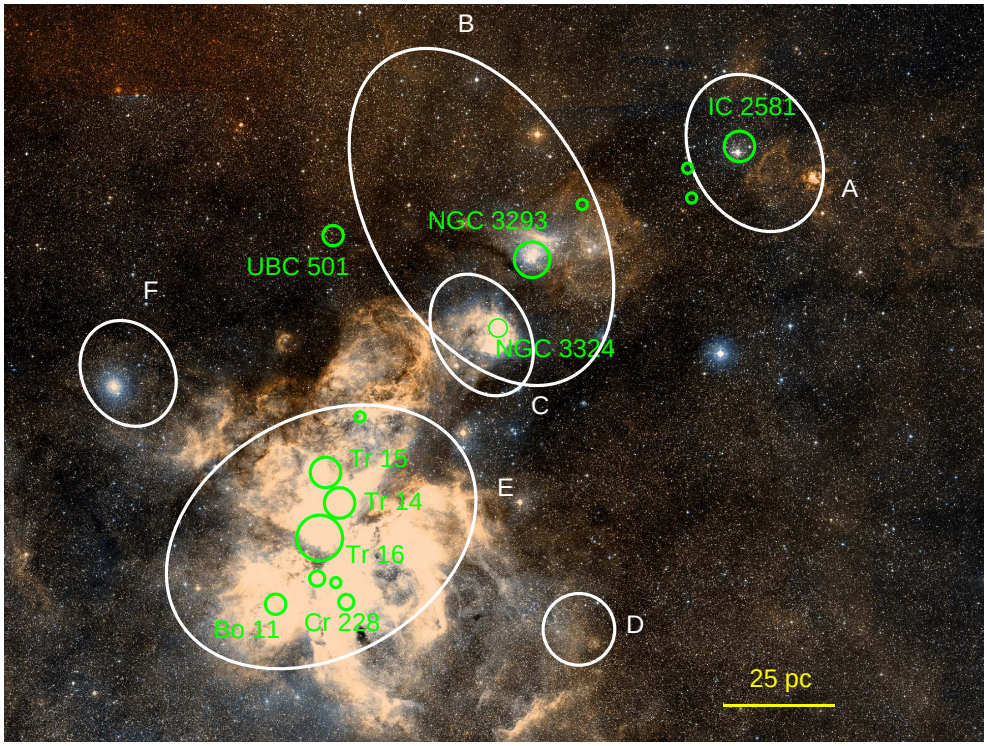

Figure 2.8: Optical color-composite DSS2 image of the Carina OB1 association with its subgroups (Mel'Nik & Efremov, 1995) and stellar groups and clusters highlighted. The field of view is $5.4° \times 4.0°$. North is up, and east is to the left.

2.11 Distance to the Car OB1 association

Prior to *Gaia*, the analysis of η Carina's expanding homunculus provided an accurate distance estimate of 2.3 kpc to the star, while distance estimations of the individual clusters reached from 2 kpc up to $6 - 8$ kpc (Smith, 2006b; Smith & Brooks, 2008). As these distances were based on photometric distance estimations, the strong nebulosity in the Carina Nebula, resulting in high extinction and reddening of stars, introduced large uncertainties. With these uncertain distances and the location of Car OB1 in the Galactic plane, the perceived complex could have been the result of projection. This is visualized in Fig. 2.9, which shows the face-on view of the Milky Way with the position of Car OB1 on the Carina-Sagittarius arm highlighted.

With *Gaia* EDR3 and its astrometric data, it is now possible to determine distances to each cluster in the association with unprecedented accuracy. This analysis was done in Göppl & Preibisch (2022), where a catalog of high-mass stars in the CNC was compiled, and the *Chandra* X-ray catalogs of the CCCP, NGC 3324, and NGC 3293 were matched to the *Gaia* data. The cluster distances were estimated by applying the Maximum Likelihood method and Bayesian inference model to the parallaxes of the stars, and it was determined that the clusters in the CNC lie at similar distances of 2.35 ± 0.05 kpc. The clusters,

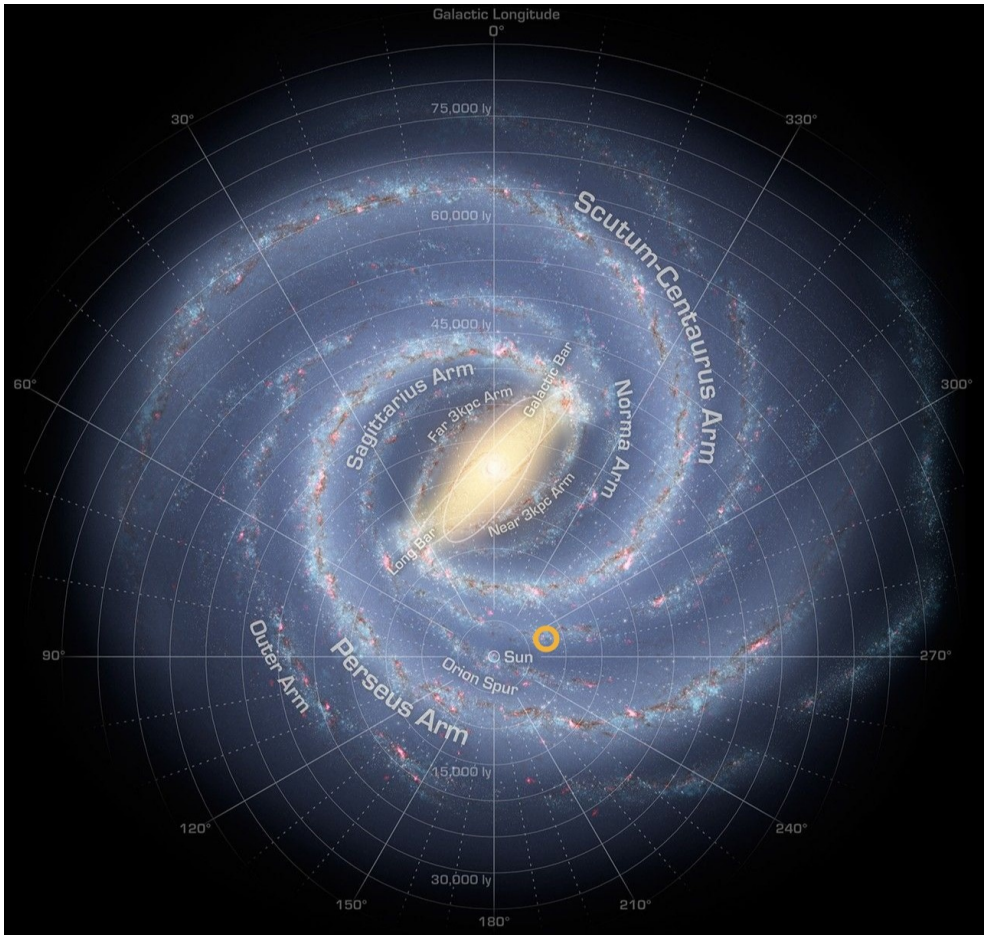

Figure 2.9: Artist's concept of the face-on view of the Milky Way. The position of Car OB1 is highlighted as an orange circle. Image Credit: NASA/JPL-Caltech/R. Hurt (SSC/Caltech).

therefore, do constitute a complex and are not a chance projection. In Göppl & Preibisch (2025), we have also extended our area of interest to IC 2581, located at the north-western edge of Car OB1, in our cluster analysis, and found that it has a compatible distance to the CNC. The full Car OB1 with its subgroups as determined in Mel'Nik & Efremov (1995) and its clusters is shown in Fig. 2.8.

STRUCTURE OF THE THESIS

A large fraction of stars is born in regions with strong FUV radiation, like the Carina OB1 association, which hosts a large number of massive stars that influence the whole region. Detailed knowledge of the whole association, i.e., the stellar cluster population and distributed massive star population, is therefore not only necessary for the learn more about the star-forming region itself but is also the basis for future studies which focus on the evolution and formation of young stellar objects, their disks, and exoplanets in the association.

In Chapter 3, we characterize the cluster population of Car OB1 by carrying out an unbiased search for stellar clusters using astrometric *Gaia* DR3 data and the clustering algorithm DBSCAN (Ester et al., 1996). We then determine distances and ages of these in order to select the ones that belong to the association, and analyze the internal kinematics of the clusters. In order to learn more about the massive stars, we combine *Gaia* DR3 astrometric data with massive stars from the literature and the *Gaia* DR3 `astrophysical_parameters` table to search for the distributed massive star population.

In Chapter 4, we use simulated cluster data to determine the reliability of the method used in Chapter 3 to analyze the cluster's internal kinematics, i.e., to detect expansion or contraction in a cluster.

In Chapter 5, we apply our knowledge about stellar clusters and the massive star population in Car OB1 and combine it with the IMF to determine the cluster population and how many supernovae have already exploded per cluster. We perform a traceback of the cluster positions using the galactic dynamics package `galpy` (Bovy, 2015) to calculate the inter-cluster distances at the time of their formation. As discussed in Sect. 1.3.1, expanding superbubbles can trigger cluster formation. In Car OB1, older clusters have already experienced supernova explosions at the time younger clusters were formed, and combining this with the inter-cluster distances, we propose a star formation scenario for the association.

A summary of this thesis and an outlook to future projects pertaining to the Car OB1 are presented and discussed in Chapter 6.

CHAPTER 3

SPATIAL DISTRIBUTION AND CLUSTERING PROPERTIES OF THE YOUNG STELLAR POPULATIONS IN THE CARINA NEBULA COMPLEX AND CAR OB1

C. Göppl and T. Preibisch, *Astronomy & Astrophysics* 695, A48

3.1 Introduction

Most stars form in large complexes consisting of giant molecular clouds, open clusters, and OB associations (see, e.g., Wright et al., 2023, for a recent review). The spatial distribution of the young stellar populations in these complexes is often highly substructured. The young stars concentrated in open clusters, which are often prominently featured in optical or infrared images, are rather easy to identify, but the population of young stars in a "widely distributed" configuration with a low average stellar space density is much more difficult to identify and study. The relation between the clusters and the distributed population bears important implications about the formation and evolution of OB associations (see, e.g., Ward et al., 2020). The spatial configuration of the stellar populations also sets the environment in which stars form and their protoplanetary disks evolve. The disk evolution and planet formation processes can be strongly affected by environmental influences such as photoevaporation driven by external UV irradiation from nearby O-type stars (e.g., Winter & Haworth, 2022; Ramírez-Tannus et al., 2023). Even for models of the origin of the Solar System, the spatial distribution of stellar populations in the birth environment

of the Sun plays an important role (e.g., Adams, 2010; Arakawa & Kokubo, 2023).

The Car OB1 association (see Mel'Nik & Efremov, 1995) contains several hundred OB stars and extends over ≈ 5 degrees on the sky, corresponding to a physical diameter of ≈ 200 pc (see Fig. 3.1). The optically most prominent part of Car OB1 is the famous Carina Nebula (NGC 3372, see, e.g., Smith & Brooks, 2008), a large H II region that is located in a giant molecular cloud complex (Smith et al., 2000; Rebolledo et al., 2016), which we refer to as the Carina Nebula complex (CNC, hereafter). The CNC has a total cloud mass of $\approx 10^6$ $M_\odot$ (Smith & Brooks, 2007; Preibisch et al., 2012), extends over ≈ 3 square-degrees on the sky, and harbors more than 100 high-mass (i.e., O-type, WR, and supergiant) stars (e.g., Smith, 2006a; Berlanas et al., 2023).

Our knowledge of the stellar populations in the CNC and Car OB1 is still very inhomogeneous. For the central area of the CNC, the young stellar populations down to ≈ 1 $M_\odot$ were uncovered by the X-ray imaging survey of the *Chandra* Carina Complex Project (CCCP; see Townsley et al., 2011b, for an overview). Outside the CCCP field, studies of the stellar populations are largely restricted to patchy regions around a few prominent clusters. The clusters Trumpler 14, 15, 16 in the central Carina Nebula, NGC 3324 to the north, and NGC 3293 near the northwestern edge of the cloud complex, have been well studied at optical, infrared (e.g., Smith et al., 2010; Preibisch et al., 2011a; Damiani et al., 2017; Povich et al., 2019; Hur et al., 2023; Itrich et al., 2024), and X-ray wavelengths (Townsley et al., 2011b; Wolk et al., 2011; Wang et al., 2011; Preibisch et al., 2014a, 2017). Analysis of the *Gaia* DR3 data for the known OB stars and the X-ray selected stars in the CNC has yielded a common and well-defined distance of (2.35 ± 0.05) kpc (Göppl & Preibisch, 2022). From the above mentioned studies, ages ranging from $\approx$1–2 Myr (Tr 14 and NGC 3324), over $\approx$3–4 Myr (Tr 16), and up to $\approx$8–10 Myr (Tr 15 and NGC 3293) have been estimated. In some parts of the CNC, such as the "Southern Pillars" region south of Tr 16 (e.g., Smith et al., 2010) or the H II bubble rim[1] around NGC 3324 (Ohlendorf et al., 2013), star formation is still ongoing.

The cluster IC 2581 (subgroup A of Car OB1, at the northeastern edge of the association) is located outside the CNC and has received much less attention so far. Its distance of $\simeq 2.4$ kpc and age of $\simeq 12$ Myr derived from *Gaia* data by Tarricq et al. (2021), and confirmed in this study, fits well within the range of values for the large clusters in the CNC.

In addition to these prominent and rather well-studied clusters, a variety of further smaller clusters and stellar groups have been found in searches of selected regions in the CNC (e.g., Smith et al., 2005, 2010; Feigelson et al., 2011; Preibisch et al., 2014b, 2021). However, most of these clusters and groups have been identified by visual inspection of various image data, and thus, the resulting cluster sample is very inhomogeneous. No systematic and homogeneous search for clusters over the full spatial extent of the CNC or Car OB1 has been performed so far.

A further complication arises from the fact that the CNC is located directly on the

[1]including the "Cosmic Cliffs" region imaged as part of the Webb Early Release Observations (see Crompvoets et al., 2024).

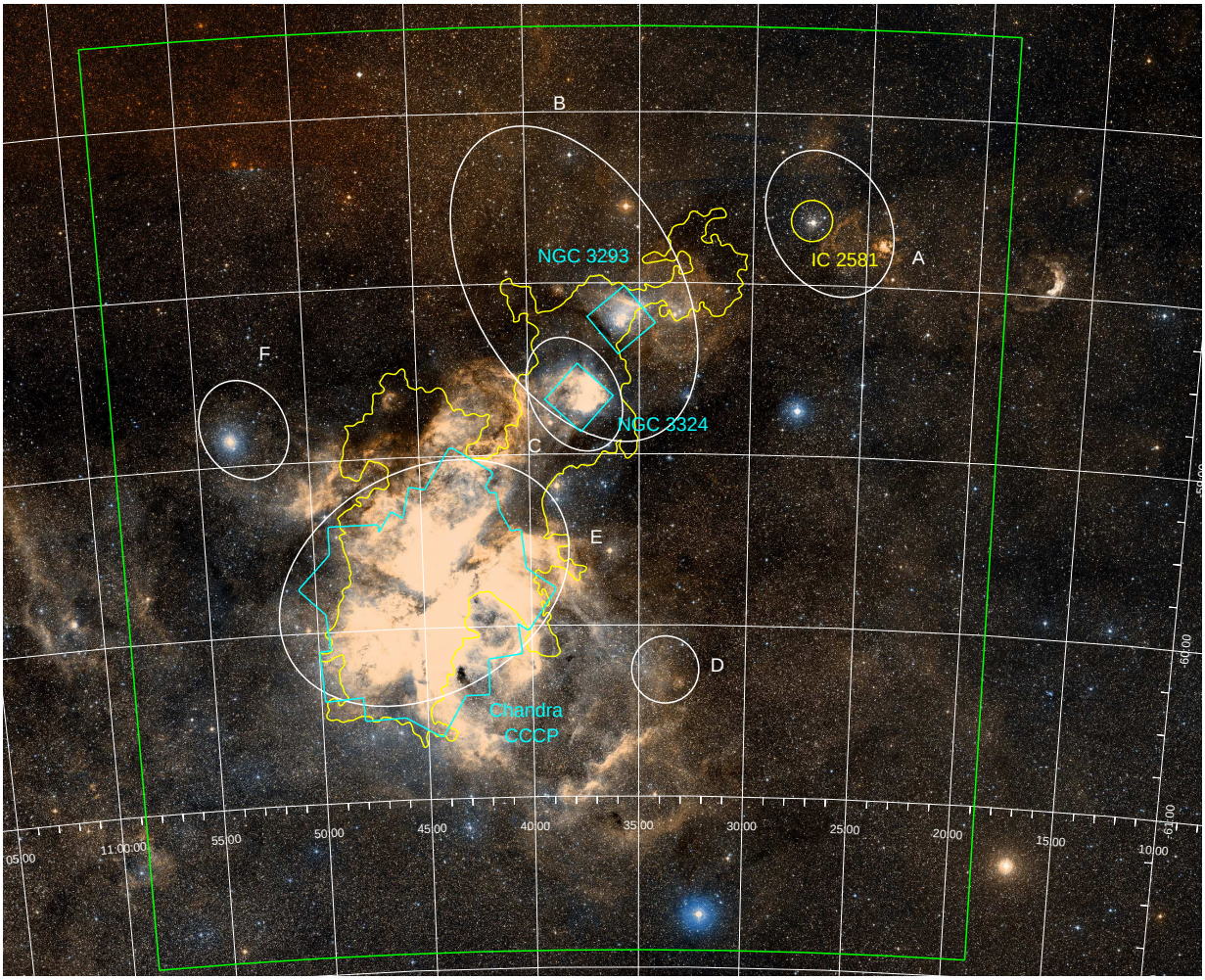

Figure 3.1: DSS2 optical image of the area around the Carina Nebula, with outlines illustrating the spatial extent of the cloud complex (CNC, yellow) and the subgroups of the Car OB1 association. North is up and east to the left. The white grid shows the J2000 celestial coordinates. The yellow line shows the boundary of the cloud emission related to the CNC as traced by the contour for a surface brightness of ≥ 7.4 mJy/(arcsec)^2 in the *Herschel* 160 μm map. The X-ray survey region of the *Chandra* Carina Complex Project (CCCP) as well as the areas of the additional *Chandra* observations of NGC 3324 and NGC 3293 are marked with cyan outlines and labeled, the cluster IC 2581 is highlighted in yellow, and the white ellipses show the subgroups in Car OB1 as defined in Mel'Nik & Efremov (1995). The area for our cluster search with DBSCAN is marked in green.

galactic plane and near the tangent point of the Carina-Sagittarius spiral arm. The sky field around Car OB1, therefore, shows galactic clusters over a wide range of different distances. To mention just two examples, the famous star cluster Westerlund 2 in the galactic background ($D \approx 4.2 - 6$ kpc, see Hur et al., 2015; Zeidler et al., 2018) is seen just next to Car OB1 subgroup A, and the foreground cluster vdBH 99 ($D = 440$ pc) is seen in front of the western part of the CNC (see Göppl & Preibisch, 2022).

The astrometric data from *Gaia*, for the first time, now allow for a systematic and unbiased search for clusters to be performed over the full area of Car OB1 ($\approx 5 \times 5$ square-degrees). The approach of identifying clusters in the five-dimensional [position – proper motion – distance] space is completely independent of the previous cluster searches by visual image inspection. This search also provides an objective basis for the distinction between the stellar populations in clusters and the distributed stellar population. Furthermore, the spectral type information available for a subset of the stars in the *Gaia* catalog can be used to search for further and yet unidentified high-mass stars over the full spatial extent of Car OB1.

In this chapter, we address the following questions:

1. How many known clusters and stellar groups (identified by visual inspection) can be confirmed as coherent stellar groupings, and how many of them are only chance-alignments of actually unrelated stars?

2. Which of the clusters seen in the Car OB1 area are actually in Car OB1 (i.e., at a distance of 2.35 kpc), and which are in the galactic background?

3. Can we find more clusters in Car OB1?

4. Can we find evidence for the expansion of the individual clusters?

5. Can we confirm and quantify the expansion of the whole OB association?

6. Can we obtain more quantitative information about the distributed population of young stars, in particular, how large this population is in comparison to the population of clustered stars, and how far it extends in comparison to the extent of the cloud complex and the currently known association subgroups?

7. Can we improve the census of high-mass stars in the CNC and Car OB1 by using *Gaia* data?

In the following, we denote as "Carina Nebula" the central visually bright nebulosity in Fig. 1 (diameter $\approx 2°$), we identify the "CNC" as the extended (diameter $\approx 3.7°$) cloud complex as approximately traced by the far-infrared emission contour shown in Fig. 1, and we designate as "Car OB1" the area comprising the five OB subgroups marked in Fig. 1 (diameter $\approx 5°$).

3.2 A catalog of spectroscopically identified high-mass stars in Car OB1

As an initial step of our analysis, we collected literature data in order to compile a comprehensive catalog of stars with spectroscopically determined spectral types in the area of Car OB1, and checked their *Gaia* DR3 parallaxes for consistency of being members of Car OB1. Our aim was to create a catalog of high-mass stars that can serve as an update and an extension (in search area) of the stellar census of high-mass stars in the Carina Nebula by Smith (2006a). We therefore considered stars with spectral types O and B, Wolf-Rayet (WR) stars, as well as supergiants.

For this, we combined the list of 241 previously known OB stars in the area of the CNC collected from the literature in Göppl & Preibisch (2022) (comprising 80 O-type, 2 WR, 154 B-type stars, and 5 supergiants) with 203 OB stars from Berlanas et al. (2023) (14 O-type, 1 LBV, 181 B-type stars, and 7 supergiants), 35 OB stars (3 O-type, 31 B-type stars, and 1 supergiant) from Alexander et al. (2016), 82 stars (15 O-type, 41 B-type stars and 26 supergiants) from Melnik & Dambis (2020), 40 stars (38 B-type stars and 2 supergiants) from Damiani et al. (2017), 10 stars (9 B-type stars and 1 supergiant) from Lim et al. (2019), 2 M-type supergiants from Humphreys (1978), and 5 stars (3 B-type stars and 2 supergiants) from Mel'Nik & Efremov (1995). This resulted in a sample of 618 OB stars. The use of the word "star" here refers to resolved objects and does not differentiate between single stars and spectroscopic binaries. If both parts in a spectroscopic binary are taken into account (as in Sect. 3.5.3), it is explicitly mentioned. For 617 of these stars, we could identify a reliable *Gaia* DR3 match (in almost all cases at a matching radius of $\leq 1''$), and 613 of these have a full astrometric solution in *Gaia* DR3.

As found in Göppl & Preibisch (2022), the stellar population in the CNC has a well-defined and common distance of 2.35 kpc. At this distance, the $\approx 5^\circ$ angular diameter of Car OB1 corresponds to a physical diameter of ≈ 200 pc. We therefore define the interval of ± 100 pc around 2.35 kpc (i.e., from 2.25 kpc to 2.45 kpc) as the likely distance interval for Car OB1. We exclude stars from the Car OB1 sample if their $\pm 2\sigma$ distance uncertainty interval (calculated from their inverted parallax) is incompatible with the $[2.25\,, 2.45]$ kpc distance interval for Car OB1. This selection leads to a final sample of 517 stars (including 22 spectroscopic binaries), which we denote as Car OB1 high-mass star sample in the following. This sample includes 88 O-type, 3 WR, 36 supergiant stars, and 1 luminous blue variable (η Car). The complete list of these stars is provided in Table 3.6 labeled with 'L' in the column 'Selection' (also available at the CDS).

3.3 A systematic search for clusters over the full extent of Car OB1

3.3.1 Cluster search with DBSCAN

Gaia astrometry can be utilized for the identification of star clusters, distance estimations, and kinematic and structural analysis of the found clusters. We used the algorithm DBSCAN (Density Based Spatial Clustering of Applications with Noise, Ester et al., 1996) to search for clusters in the five-dimensional space defined by position, proper motion, and parallax. The algorithm identifies star clusters based on their overdensity in the 5D-space compared to the field star density. It has two input parameters: $minPts$ and the density parameter ϵ. DBSCAN assigns each source one of three designations: core point, non-core point, or noise point. Sources are classified as a core point if there are at least $minPts - 1$ other points inside a hypersphere with radius ϵ around that source. Non-core points can reach at least one core point in a hypersphere with radius ϵ, but not enough other sources to be considered a core point themselves. Noise points have no core points lying inside a hypersphere with radius ϵ centered around them. Advantages of DBSCAN are that it can identify clusters with arbitrary shape and that the number of clusters does not need to be specified beforehand, but the results depend heavily on its input parameters, especially ϵ.

We applied the method devised by Castro-Ginard et al. (2018) to determine ϵ. This method exploits the fact that cluster members have shorter nearest neighbor distances compared to field stars, which is then used to determine the density parameter ϵ that separates the cluster and field populations.

First, the kth nearest neighbor distance (with $k = minPts - 1$) for all stars in the sample is calculated, and the minimum is saved as ϵ_{kNN}. Then the sources are resampled using a Gaussian kernel density estimator that creates a new sample with the same amount of stars that mimics a field without any clusters and only field stars. Then the kth nearest neighbor distance is again computed and the minimum is saved. Since each resampling leads to a different realization, this step is carried out thirty times in order to minimize the impact of outliers. The mean of the resampled minimum kth nearest neighbor distance is then taken as ϵ_{GKDE}. The final ϵ value is calculated as $\epsilon = (\epsilon_{kNN} + \epsilon_{GKDE})/2$.

For our analysis, we used a five-dimensional approach based on position (l, b), parallax (ϖ), and proper motion $(\mu^*_\alpha, \mu_\delta)$ of the stars. We rescaled our data to have a mean of zero and a standard deviation of one. The input parameter $minPts$ was chosen as $minPts = 10$, which is twice the number of dimensions as recommended in Sander et al. (1998).

For our cluster search in Car OB1, we utilized the *Gaia* DR3 catalog (Gaia Collaboration et al., 2016, 2023). We chose a rectangular field centered around $(\alpha, \delta) = (10^{\mathrm{h}}38^{\mathrm{m}}48^{\mathrm{s}}, -59°12')$ with dimensions of $\approx 5° \times 5.4°$ to analyze the whole Car OB1 region. The chosen search field can be seen as a green box in Fig. 3.1. This area contains 9 295 328 objects in the *Gaia* DR3 database, out of which 8 236 565 (88.6%) have full astrometry (position, proper motions, and parallax) available. Following the results by Lindegren et al. (2018), we excluded all sources with RUWE > 1.4, which removes sources with very

uncertain astrometry and minimizes the impact of bad astrometric fits. This left us with 7 807 017 (84%) sources to which we applied the parallax offset correction provided by Lindegren et al. (2021). Since only 1.6% of the objects in our sample have a radial velocity measurement in the *Gaia* DR3 catalog, a cluster search in full position-velocity space (6D) was not feasible.

We divided the selected field into 90 individual sections with $L \times H \approx 0.5^\circ \times 0.6^\circ$. In order to not miss any clusters at the edges of a section or overlapping between several sections, we vary the sections by $L/2$ and/or $H/2$, and run DBSCAN on the additional fields. Finally, we compiled a merged sample of 462 unique clusterings, identified by DBSCAN as overdensities, in the full area.

We classify the 365 overdensities with fewer than 20 members as stellar groups, and the 97 overdensities with 20 or more members as stellar clusters. The locations of all identified clusters and groups are visualized in Fig. 3.2.

Distances of the clusters and groups were determined in a two-step procedure. In the first step, we computed a maximum likelihood estimate of the mean distance, that is, the inverted error-weighted mean value of the parallaxes of the member stars. In a second step, we then applied the Bayesian inference code *Kalkayotl* (Olivares et al., 2020), which determines the mean distance values and associated confidence intervals for the clusters, using the Maximum Likelihood estimate as a prior for the distance. In the subsequent analysis, we used the distance estimates based on *Kalkayotl* for all clusters with distances less than 5 kpc; for clusters with larger distances, we used the Maximum Likelihood inferred mean distance since *Kalkayotl* is less reliable for cluster distances greater than 5 kpc (see discussion in Olivares et al., 2020).

A substantial number of groups or clusters are located very close to another group or cluster, and are therefore probably subparts of a larger group/cluster. We assume that a group or cluster is a substructure of another cluster if it lies inside a cluster's $2 \times r_{90}$ radius (with r_{90} being the radius in which 90% of the DBSCAN members of the cluster lie) and if their $\pm 1\sigma$ distance intervals (derived from inverting the mean parallax) overlap.

This leads to 38 clusters, including Tr 14, 15, 16, Bo 11, NGC 3324, and IC 2581, containing in total 93 subclusters. Cluster Tr 16 was found to be divided into six individual subclusters by DBSCAN, similar to the result of the cluster analysis in Feigelson et al. (2011). The full list of found stellar clusters and groups can be found in the Appendix in Table 3.5.

3.3.2 Relation to previously known clusters

We cross-checked our list of DBSCAN clusters and groups with a list of previously known cluster in the area compiled from the literature (Cantat-Gaudin et al., 2018, 2020; Castro-Ginard et al., 2018, 2020, 2022; Hao et al., 2022; Feigelson et al., 2011; Kuhn et al., 2014; Smith et al., 2010; Hunt & Reffert, 2023; Bica et al., 2019). We found literature counterparts for 61 (63%) of our DBSCAN clusters and for 31 (8%) of our DBSCAN groups. Almost all of the well-known CNC star clusters (in particular, Tr 14–16, Cr 228 and 232, Bo 11, NGC 3324, and NGC 3293) were also identified as clusters in our DBSCAN

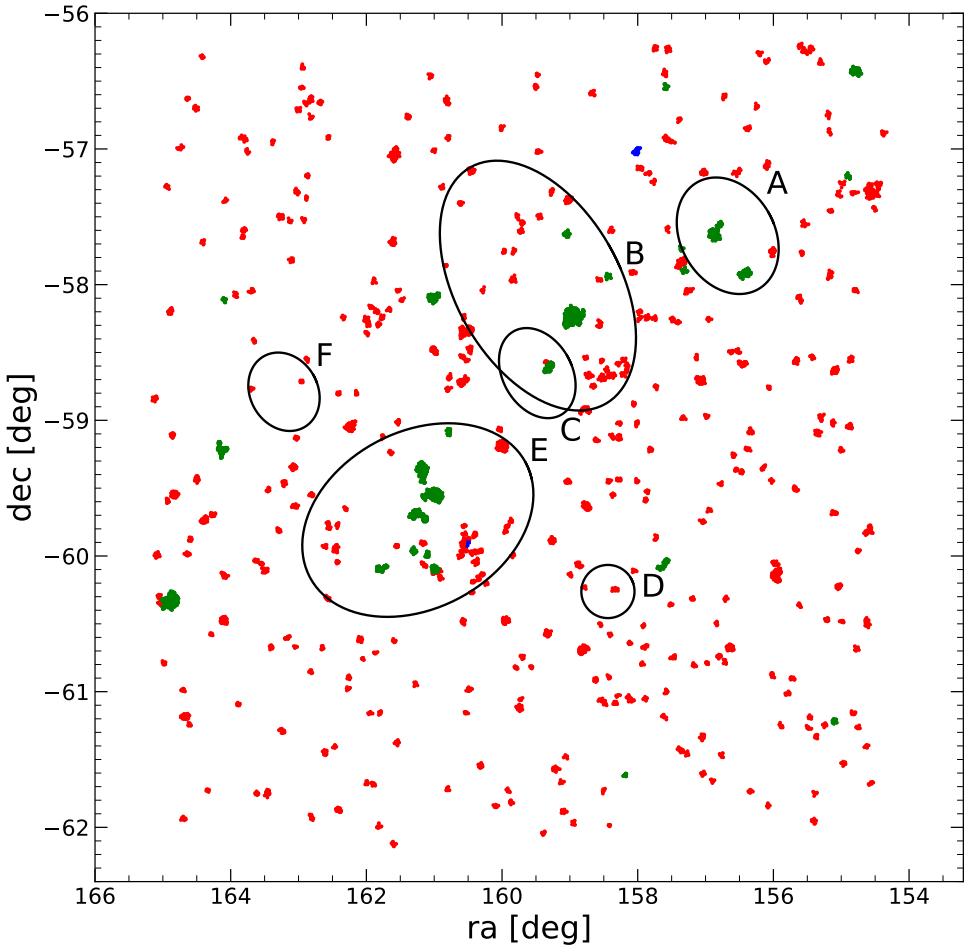

Figure 3.2: Map of all clusters and groups identified with DBSCAN in the investigated region. Clusters with a mean parallax that is consistent with the distance of the CNC (2.35 kpc) are shown in green, clusters in the background in red, and clusters in the foreground in blue. The ellipses show the Car OB1 subgroups as defined by Mel'Nik & Efremov (1995).

search.

Four previously known clusters were not recovered in our DBSCAN cluster search for various reasons:

(1) The Treasure Chest cluster, a very young ($\lesssim 0.1$ Myr (Smith et al., 2005)) cluster still embedded in its natal cloud. With typical visual extinctions ranging from $A_V \gtrsim 5$ mag up to $A_V \approx 50$ mag for individual members (Smith et al., 2005; Preibisch et al., 2011b), most cluster members are too faint at optical wavelengths to be detected by *Gaia*.

(2) Tr16-SE, a strongly obscured cluster of stars south-east of Tr 16, which was discovered in infrared and X-ray observations (Sanchawala et al., 2007; Preibisch et al., 2021). Due to the high extinction, only very few stars in this cluster were detected by *Gaia*.

(3) Bo 10, which constitutes a quite sparse stellar group with a low star density, was not identified with DBSCAN. Patat & Carraro (2001) and Carraro et al. (2004) had already suggested that Bo 10 may not be a real physical cluster.

(4) Cr 234, a group of stars located just $\approx 1.5'$ south-east from the edge of Tr 16; we classify it here as one of the subclusters of Tr 16, as already suggested by Carraro et al. (2004) and Feigelson et al. (2011).

3.3.3 New clusters in Car OB1

Our first criterion for assuming a cluster or a group to be part of Car OB1 is that the 90% confidence interval for its distance (determined with *Kalkayotl*) is compatible with the distance interval of [2.25, 2.45] kpc for Car OB1 as mentioned in Sect. 3.2. Out of the 462 clusters and groups, 47 fulfill this criterion. Group 339, with $D_{\rm ML} = 15.9^{+61.9}_{-7.1}$ kpc, satisfies this requirement only due to its extremely large distance uncertainty; we therefore exclude this cluster from our list of Car OB1 clusters. The positions of all clusters and groups in the investigated area are shown in Fig. 3.2, where also the subgroups of the Car OB1 association (as defined by Mel'Nik & Efremov, 1995) are shown as black ellipses. We exclude groups 23, 32, 130, 132, and 424 from being a part of Car OB1 due to their large spatial separation from any of the Car OB1 subgroups and the cloud complex.

3.3.4 Cluster age estimates

As a second criterion for assuming a cluster to be related to Car OB1, we considered the clusters' ages. Table 3.1 lists the age estimates for previously known clusters in Car OB1 collected from the literature. Since we are interested in the young ($\lesssim 30$ Myr old) populations of the Car OB1 association, we excluded the six previously known clusters/groups with literature ages of $\gtrsim 40$ Myr.

To determine cluster ages, we used the PARSEC v3.7 stellar evolution models (see Bressan et al., 2012) and fit them to a color-magnitude diagram of the DBSCAN-selected members of all potential Car OB1 clusters. For most clusters, we find values that agree well with the literature-based age estimations. We find deviating ages for UBC 501 and Tr 17, which can be seen in Fig. 3.3. No age confirmation was possible for [DBS2003] 53 due to a low number of members. For UBC 501, we find a slightly older age than listed in the literature, but still under the maximum age requirement for Car OB1. For Tr 17, our age estimate of ≈ 80 Myr, together with the cluster's location well outside the cloud complex and the known association subgroups, excludes this cluster from the association. With fewer than 20 members, it was not possible to confirm ages for stellar groups using CMD fitting. We therefore included groups 114, 117, 184, and 291 in our Car OB1 stellar cluster and group sample.

The locations of the clusters/groups we consider to be part of the Car OB1 association are marked in Fig. 3.4; their basic properties are listed in Table 3.2. In total, we find 15 clusters and groups (split into their 27 (sub)clusters and groups in Table 3.2) to be part of Car OB1.

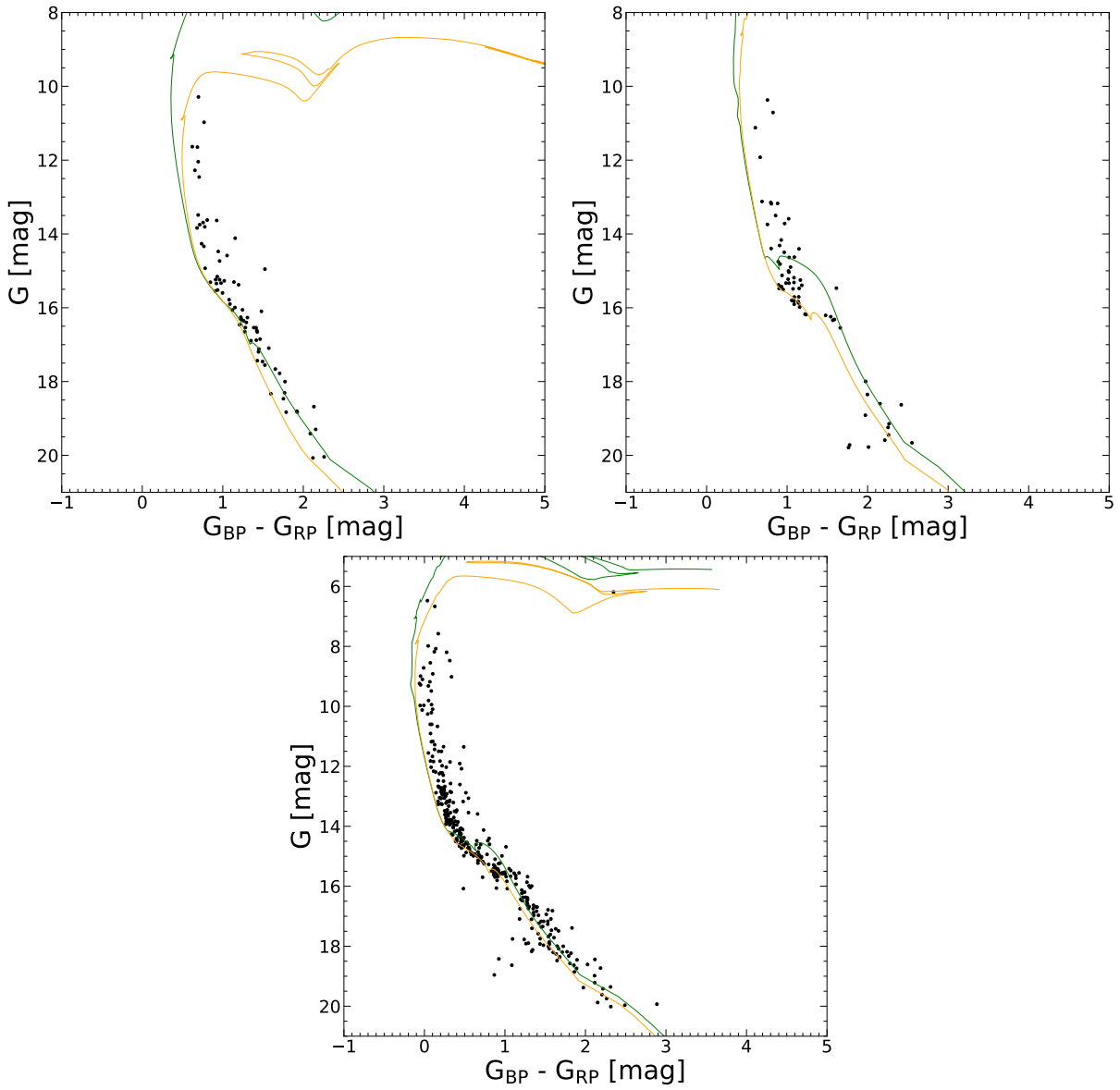

Figure 3.3: Color-magnitude diagrams of the DBSCAN-selected members of clusters with their literature age and their best-fitting PARSEC v3.7 isochrone (Bressan et al., 2012). Left panel: Tr 17 with 20 Myr (Cantat-Gaudin et al., 2020) isochrone in green and 80 Myr isochrone in orange, assuming an extinction of $A_V = 1.6$ mag for both isochrones. Middle panel: UBC 501 with 6 Myr (Liu & Pang, 2019) isochrone in green and 13 Myr isochrone in orange, assuming an extinction of $A_V = 1.8$ mag for both isochrones. Right panel: NGC 3293 with 10 Myr (Cantat-Gaudin et al., 2020) isochrone in green and 15 Myr isochrone in orange, assuming an extinction of $A_V = 0.6$ mag for both isochrones.

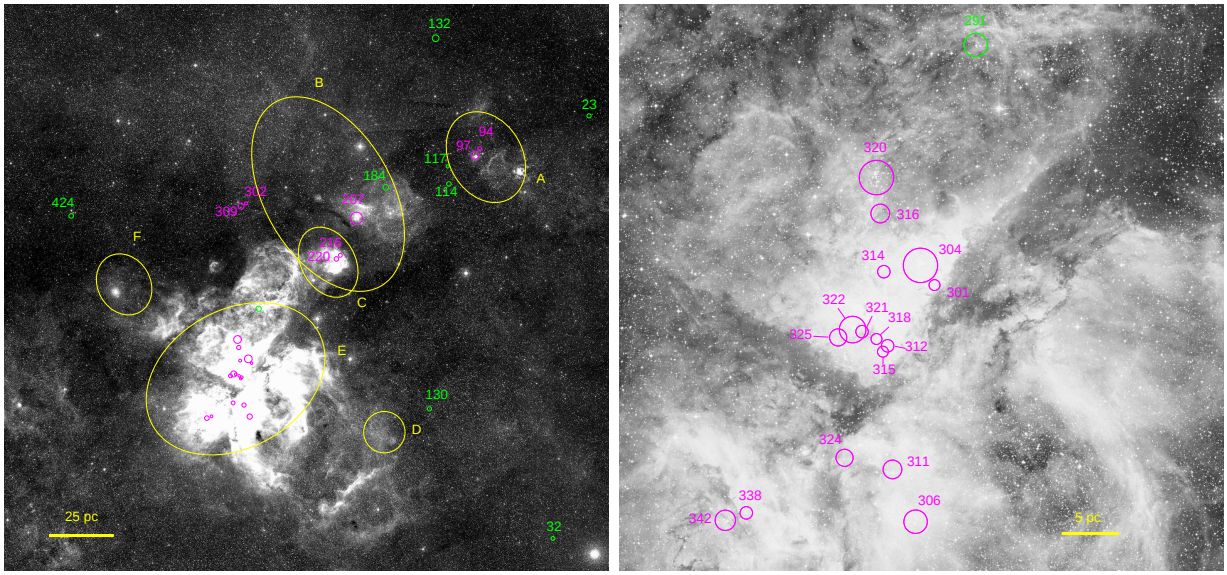

Figure 3.4: Optical image of the CNC. (Left panel: DSS2 red in grayscale; right panel: DSS2 red in grayscale `www.eso.org/public/images/eso0905b/`; image credit: ESO/Digitized Sky Survey 2, Davide De Martin). North is up and east to the left. The circles show the clusters and groups whose distance and age are compatible with being a part of Car OB1. Circles in magenta represent clusters with counterparts in the literature, and circles in green represent clusters without counterparts. The clusters' radii are chosen as the radii in which 75% of their cluster members reside.

In order to find out which of these clusters and groups are related to the clouds of the CNC, we used a mosaic of *Herschel* 160 μm maps that was produced as part of the Herschel High Level Images (HHLI) by Graciá-Carpio et al. (2017); this map is shown in Fig. 3.5. We used the contour corresponding to a surface brightness of 7.4 mJy/(arcsec)^2 to define the boundaries of the cloud emission related to the CNC. 19 of the 27 clusters and groups in Car OB1 are located inside the boundaries of the cloud complex.

3.3.5 Quantification of the clustered versus distributed populations of high-mass stars in Car OB1

For a quantification of the clustered versus distributed populations of high-mass stars in Car OB1, we need an efficient criterion for considering a star as either being a member of one of the clusters or belonging to the distributed (i.e., non-clustered) population. Out of the 517 stars in our Car OB1 high-mass star sample, 180 (35%) were identified as members of one of the clusters found by DBSCAN. Furthermore, several stars from our Car OB1 high-mass sample are located in the area of one of the found clusters, but were not classified as cluster members by DBSCAN (e.g., because they have slightly deviating parallaxes or proper motions, which precluded their classification as cluster members by DBSCAN).

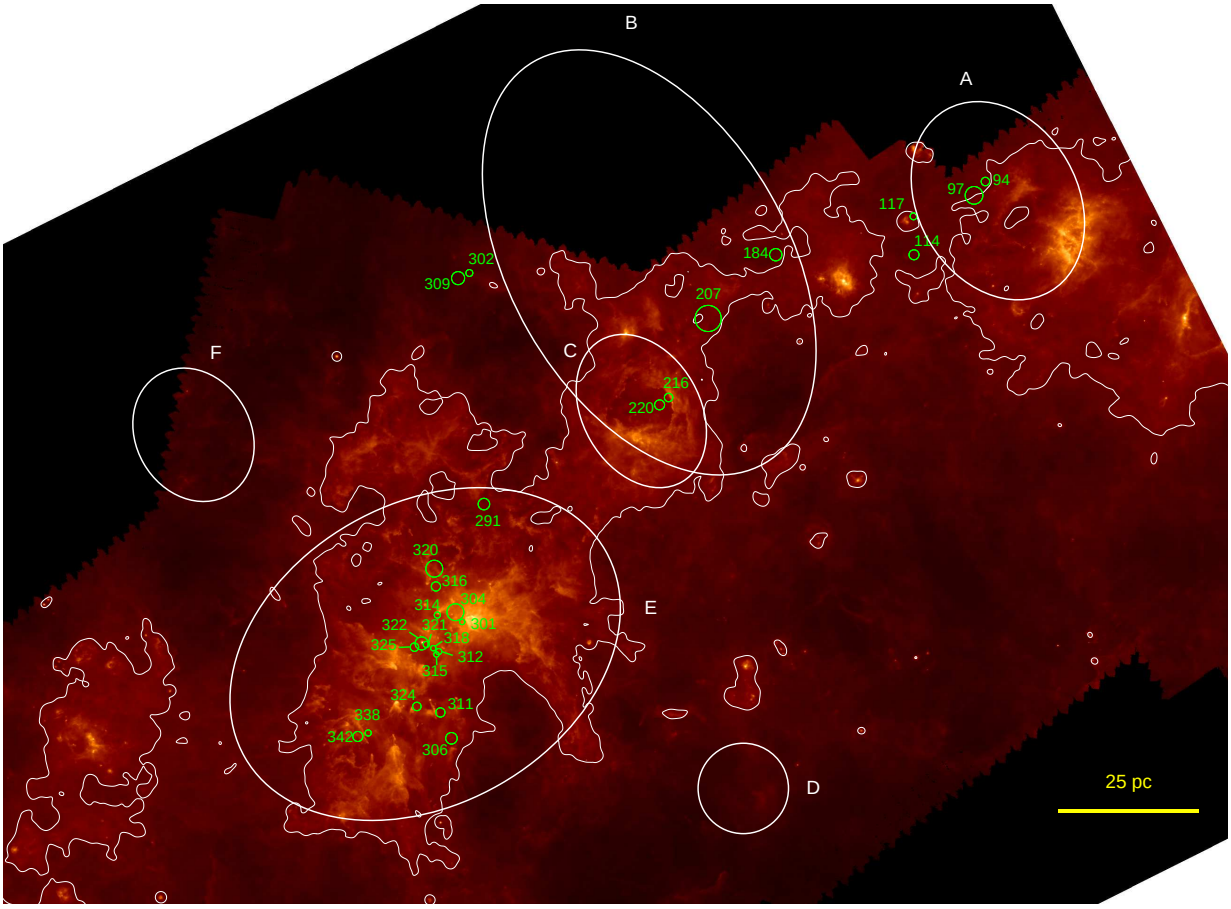

Figure 3.5: *Herschel* 160 μm image (from `https://www.cosmos.esa.int/web/herschel/pacs-jscanam-mosaics-hpdp`; see Graciá-Carpio et al., 2017) of the Car OB1 region. A white contour line is drawn at an intensity of 7.4 mJy/(arcsec)^2. The locations of clusters with distances and ages $\leq$ 20 Myr are shown in green. North is up and east to the left.

We therefore defined circles around the clusters that include all DBSCAN members[2] and assumed that all Car OB1 high-mass stars inside these circles belong to the clustered population. Figures 3.6 – 3.9 show the clusters and their chosen perimeter. With this definition, we find that 301 (58%) of the Car OB1 high-mass stars are in clusters, while the remaining 216 (42%) Car OB1 high-mass stars are part of the non-clustered, distributed population. Considering only O-type, WR, and supergiant stars, the ratio of the clustered versus distributed population changes only very slightly to 55 : 45. The 58% fraction of clustered high-mass stars is slightly higher, but similar to the $\approx$ 51% clustered population fraction among the X-ray selected young stars in the CNC (Feigelson et al., 2011), and the $\approx$ 47% fraction of clustered young stars from the analysis of the spatial distribution of infrared-excess selected young star candidates (Zeidler et al., 2016).

[2]The circle around Tr 16 extends beyond the DBSCAN member selection to include the cluster Tr16-SE, which was not identified by DBSCAN.

Table 3.1: Age estimates of the clusters in and around Car OB1.
References: (1): Itrich et al. (2024), (2): Preibisch et al. (2011b), (3): Preibisch et al. (2017), (4): Cantat-Gaudin et al. (2020), (5): Liu & Pang (2019), (6): Hao et al. (2022), (7): Kharchenko et al. (2016), (8): Morel et al. (2022).

Cluster	Age in Literature (Myr)	Reference	Age estimate this work (Myr)
Tr 14	≈ 1	(1)	
Tr 16	≈ 3–4	(2)	
Bo 11	≈ 3–10	(2)	
Tr 15	≈ 5–8	(2)	
UBC 501	≈ 6	(5)	≈ 13
NGC 3293	≈ 10, 20	(2,3), (8)	≈ 15
NGC 3324	≈ 11	(4)	
IC 2581	≈ 12	(4)	
Tr 17	≈ 20	(4)	≈ 80
UBC 258	≈ 40	(4)	
[DBS2003] 53	≈ 126	(7)	
UBC 259	≈ 126	(4)	
Cl vdBH 92	≈ 275	(4)	
Cr 220	≈ 282	(4)	
NGC 3496	≈ 537	(4)	

This demonstrates that a very substantial fraction of about 40% of the young high-mass stars with known spectral type in the complex are in a non-clustered, distributed population. While this should not be surprising, since the Carina complex is an OB association, it suggests that the census of OB stars may still be seriously incomplete, as spectroscopic searches for OB stars have been primarily focused on the central regions of the Carina Nebula and the well-known and prominent clusters in the CNC, whereas the more widely spread distributed population has received much less attention. In Sect. 3.5 we use the *Gaia* data to identify candidates for further, yet unidentified OB stars in the Car OB1, in order to move toward a more complete census of the stellar population.

Table 3.2: Clusters and groups with a mean distance compatible with Car OB1 and an age ≤ 30 Myr.
References: (1): Cantat-Gaudin et al. (2020), (2): Oliveira et al. (2018), (3): Kuhn et al. (2014), (4): Castro-Ginard et al. (2020), (5): Dias et al. (2014), (6): Smith et al. (2010), (7): Feigelson et al. (2011).

DBSCAN Cluster/Group	N	R.A. (J2000)	Dec. (J2000)	$D_{\mathrm{Kalkayotl}}$ (kpc)	Central 68.3% quant. (kpc)	literature name	age (Myr)
94	10	10:27:08.99	−57:33:41.5	2.432	[2.352, 2.513]	part of IC 2581 (1)	≈ 12
97	109	10:27:28.73	−57:37:31.3	2.438	[2.369, 2.507]	IC 2581 (1)	≈ 12
114	17	10:29:16.01	−57:54:11.4	2.483	[2.381, 2.585]		
117	10	10:29:22.74	−57:44:13.8	2.537	[2.446, 2.629]		
184	11	10:33:46.12	−57:56:40.1	2.343	[2.262, 2.425]		
207	358	10:35:51.67	−58:14:13.4	2.330	[2.268, 2.392]	NGC 3293 (1)	≈ 15
216	24	10:37:02.12	−58:35:16.3	2.505	[2.414, 2.596]	part of NGC 3324 (1)	≈ 11
220	59	10:37:19.36	−58:37:17.6	2.379	[2.308, 2.450]	NGC 3324 (1)	≈ 11
291	19	10:43:04.92	−59:04:46.6	2.551	[2.454, 2.651]		
301	14	10:43:43.11	−59:35:33.9	2.333	[2.256, 2.410]	[OBB2018] 1 (2), Carina A (3), part of Tr 14 (1)	≈ 1
302	11	10:43:45.59	−58:04:48.6	2.413	[2.345, 2.479]	UBC 501 (4)	≈ 13
304	416	10:43:57.52	−59:33:03.9	2.368	[2.302 ,2.434]	Tr 14 (1)	≈ 1
306	40	10:43:59.66	−60:05:52.6	2.353	[2.280, 2.427]	Cr 228 (5)	
309	56	10:44:07.56	−58:06:12.7	2.410	[2.341, 2.478]	UBC 501 (4)	≈ 13
311	19	10:44:23.89	−59:59:12.9	2.383	[2.305, 2.461]	Spitzer B (6), CCCP-Gp 13, 14, 16 (7)	
312	11	10:44:29.97	−59:43:24.1	2.255	[2.194, 2.316]	part of Tr 16 (1)	$\approx 3-4$
314	18	10:44:34.47	−59:33:55.2	2.325	[2.263, 2.387]	Cr 232 (5), part of Tr 14 (1)	≈ 1
315	15	10:44:34.70	−59:44:09.3	2.192	[2.133, 2.251]	part of Tr 16 (1)	$\approx 3-4$
316	16	10:44:38.58	−59:26:28.7	2.463	[2.379, 2.546]	Carina F (3), CCCP-Cl 7 (7), part of Tr 15 (1)	$\approx 5-8$
318	10	10:44:41.35	−59:42:32.6	2.311	[2.240, 2.382]	part of Tr 16 (1)	$\approx 3-4$
320	238	10:44:42.72	−59:21:52.8	2.366	[2.300, 2.433]	Tr 15 (1)	$\approx 5-8$
321	9	10:44:56.05	−59:41:36.9	2.295	[2.220, 2.368]	part of Tr 16 (1)	$\approx 3-4$
322	70	10:45:05.64	−59:41:21.5	2.359	[2.293, 2.424]	part of Tr 16 (1)	$\approx 3-4$
324	24	10:45:13.04	−59:57:46.7	2.373	[2.292, 2.453]	Carina M (3), Spitzer F (6), CCCP-Cl 13 (7)	
325	16	10:45:20.24	−59:42:22.5	2.266	[2.209, 2.323]	part of Tr 16 (1)	$\approx 3-4$
338	15	10:46:53.48	−60:04:51.7	2.417	[2.337, 2.495]	Carina S (3), CCCP-Gp 28, 30 (7), part of Bo 11 (1)	$\approx 3-10$
342	31	10:47:15.05	−60:05:48.6	2.325	[2.257, 2.392]	Bo 11 (1)	$\approx 3-10$

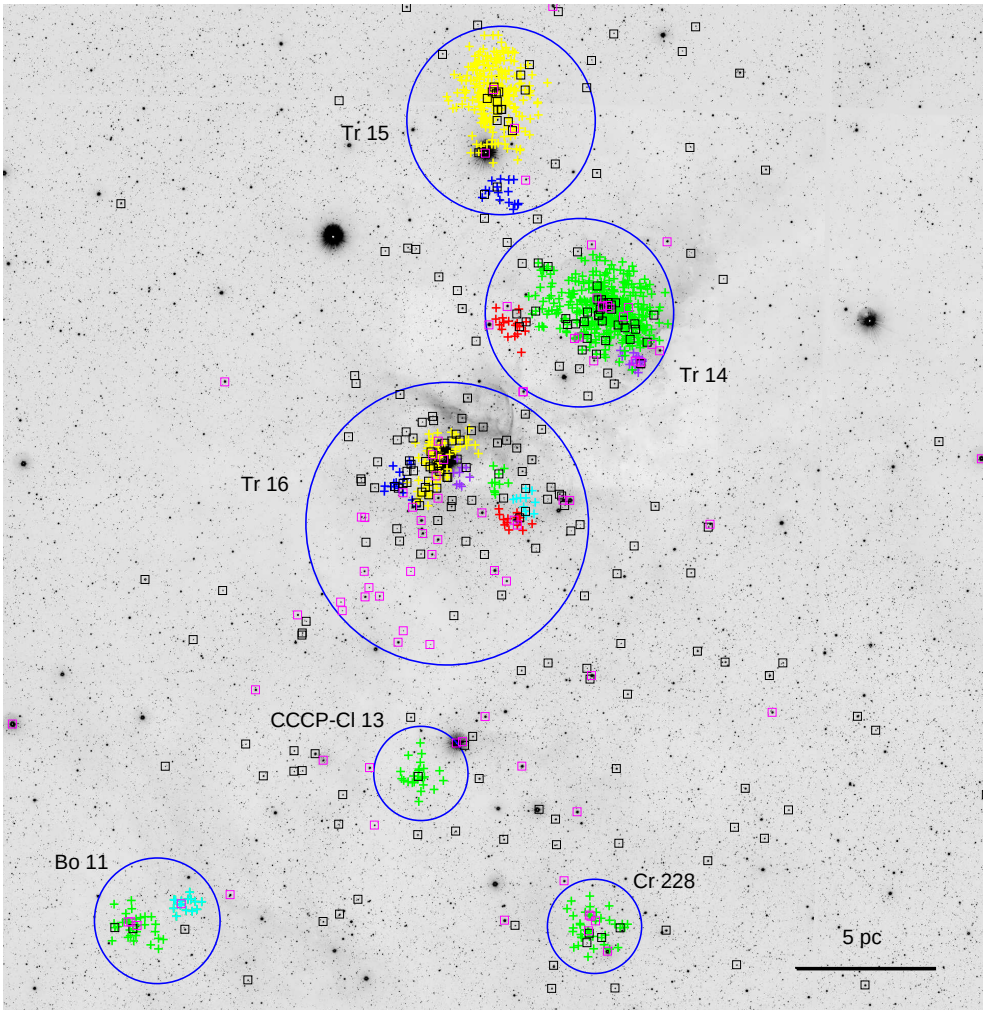

Figure 3.6: VISTA J-band image of the central region of the Carina Nebula. The DBSCAN members of the clusters Tr14, 15, and 16 (split into subclusters) are marked by crosses. O- and WR stars and supergiants from the Car OB1 high-mass star sample are marked by magenta, B-type stars by black open boxes. Stars in clusters have different colors in order to differentiate the subclusters.

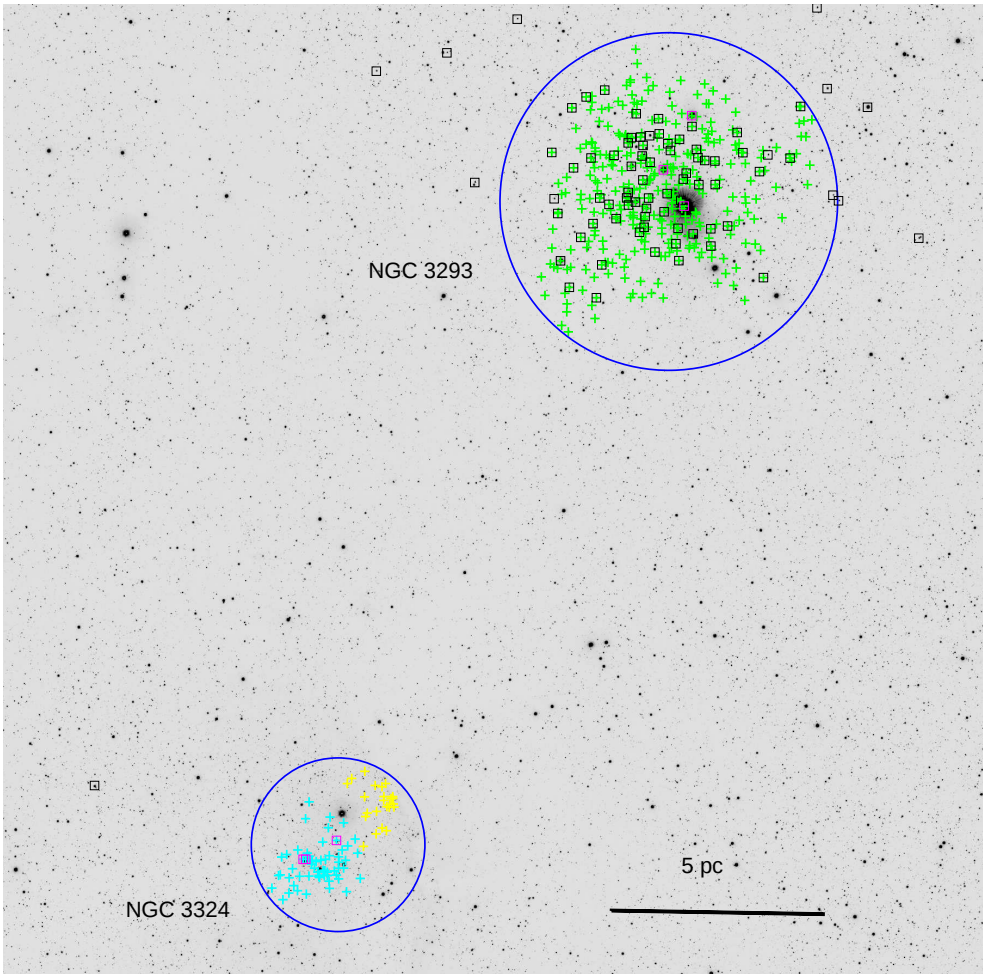

Figure 3.7: VISTA J-band image of the northwestern part of the CNC. The DBSCAN members of the clusters NGC 3293 and NGC 3324 are marked by crosses. O-type stars and supergiants from the Car OB1 high-mass star sample are marked by magenta, B-type stars by black open boxes. Stars in clusters have different colors in order to differentiate the subclusters.

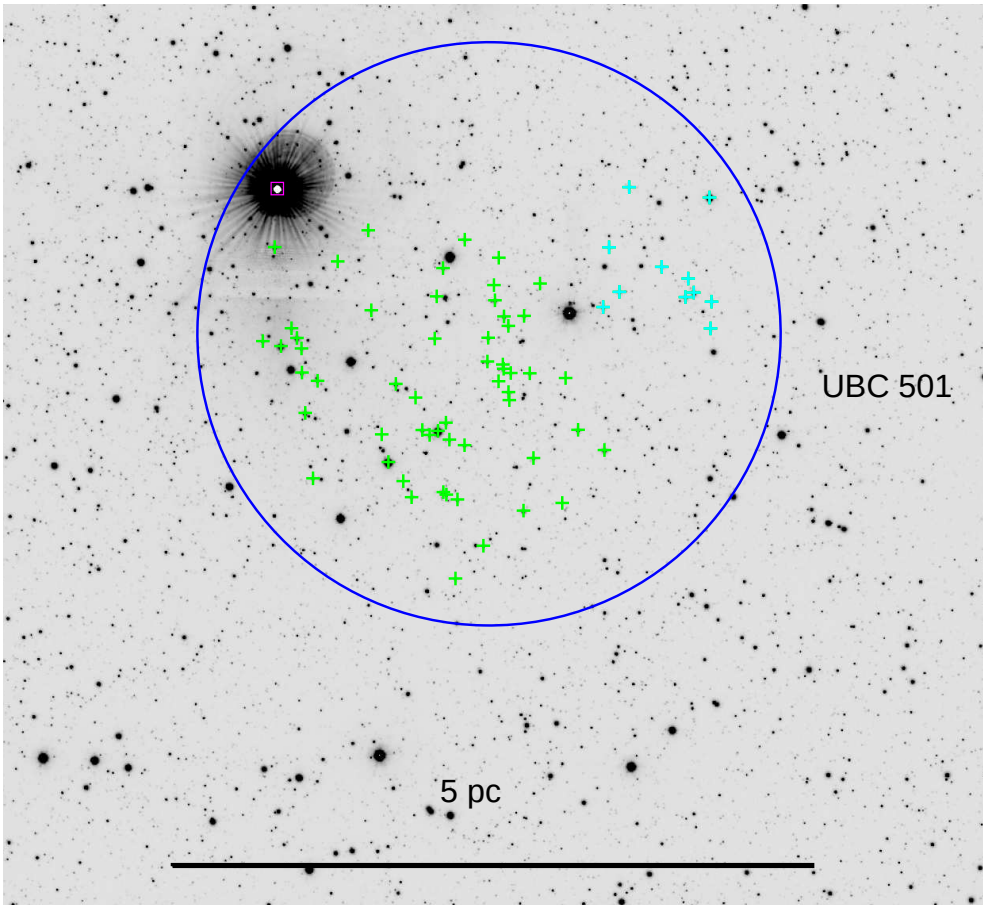

Figure 3.8: VISTA J-band image of the northwestern part of the CNC. The DBSCAN members of the cluster UBC 501 are marked by crosses. The red supergiant HD 303250 (M3Iab) is marked by the magenta box. Stars in clusters have different colors in order to differentiate the subclusters.

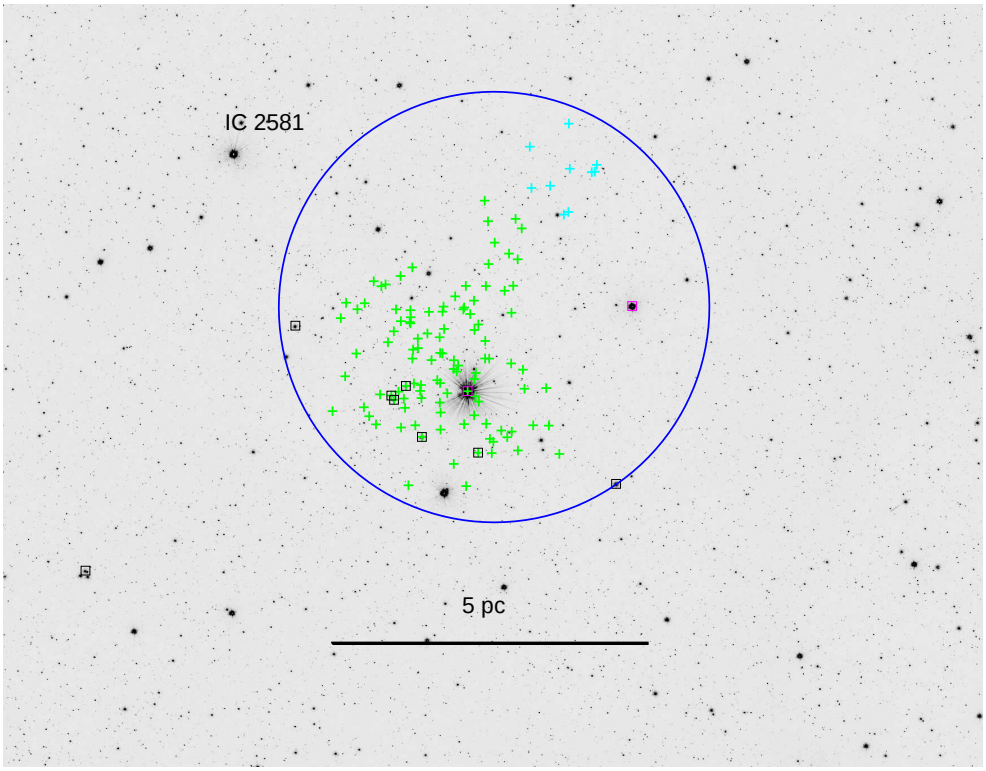

Figure 3.9: VISTA K-band image of the northwestern part of Car OB1. The DBSCAN members of the cluster IC 2581 are marked by crosses. The two supergiants V399 Car (F0Ia) and HD 90706 (B2.5Ia) are marked by magenta, B-type stars by black open boxes. Stars in clusters have different colors in order to differentiate the subclusters.

3.4 Kinematic analysis of the individual clusters

We analyzed the proper motions and radial velocities of the stars in the 10 Car OB1 DBSCAN clusters (Table 3.2) with ≥ 20 members, to gain more information about the internal kinematics of these clusters. We treated subclusters separately from their cluster if their mean weighted proper motions in either right ascension or declination lie one standard deviation outside of the full cluster's proper motion distribution in right ascension or declination. This concerns Tr 14, 15, and 16, where Groups 301, 316, and 312 showed diverging proper motion from the rest of their cluster and were treated separately.

For our kinematic analysis, we use proper motions and radial velocities from *Gaia* DR3. Since only a few stars have radial velocities in *Gaia* available, we complement these with radial velocity measurements from the Gaia-ESO survey (GES) (Gilmore et al., 2012; Hourihane et al., 2023). GES is a public spectroscopic survey whose observations include stars in the Carina Nebula and NGC 3293 and that provides radial velocity measurements for 342 stars in our cluster member list.

First, we calculated correction factors for the proper motions using radial velocities in order to account for the effect of the cluster moving toward or away from us, which can mimic expansion or contraction. For this, we used equation 13 from van Leeuwen (2009):

$$\Delta\mu_{\alpha^*,\mathrm{per}} \approx \Delta\alpha_i \left(\mu_{\delta,c} \sin\delta_c - \frac{v_r \varpi_c}{\kappa} \cos\delta_c\right) \tag{3.1}$$

and

$$\Delta\mu_{\delta,\mathrm{per}} \approx -\Delta\alpha_i \mu_{\alpha^*,c} \sin\delta_c - \Delta\delta_i \frac{v_r \varpi_c}{\kappa}, \tag{3.2}$$

with $\alpha_c, \delta_c, \mu_{\alpha^*,c}, \mu_{\delta,c}, \varpi_c$ as the weighted mean cluster properties, $\Delta\alpha_i = \alpha_i - \alpha_c$ (analogous for $\Delta\delta_i$), and $\kappa = 4.74$ as the conversion factor from milliarcsecond year^{-1} to kilometer second^{-1} at a distance of 1 kpc. For the cluster radial velocity, we used the median value of each cluster. If there were fewer than five radial velocity measurements for a cluster available, we did not calculate the correction factor. This was the case for five of the ten clusters. The correction factors were < 0.02 $\frac{\mathrm{mas}}{\mathrm{yr}}$ for all stars in the remaining five clusters, which is sufficiently small that we can assume that the lack of correction for the other five clusters has negligible influence on their results. To compare this, we have performed the kinematic analysis with and without the correction factor, if possible. The results are shown in Table 3.4 and show only small differences.

Next, we applied the correction factors (if available) as in equations (3) and (4) in Kuhn et al. (2019) and calculated the velocities v_α and v_δ, which are parallel to RA and Dec, respectively:

$$v_\alpha \approx \kappa \left(\frac{\Delta\mu_{\alpha^*,\mathrm{obs}} - \Delta\mu_{\alpha^*,\mathrm{per}}}{\varpi_c}\right) \tag{3.3}$$

and

$$v_\delta \approx \kappa \left(\frac{\Delta\mu_{\delta,\mathrm{obs}} - \Delta\mu_{\delta,\mathrm{per}}}{\varpi_c}\right). \tag{3.4}$$

In order to characterize possible expansion motions in all directions (not only along right ascension and the declination axis), we rotated the coordinate system by a sequence

of angles from $\theta = 0°$ to $\theta = 179°$ in steps of 1°, and translated the position coordinates accordingly in parsec (centered at the cluster center).

$$x(\theta) = \frac{1000}{\varpi_c}(-\Delta\alpha \cos(\theta) + \Delta\delta \sin(\theta)) \tag{3.5}$$

and

$$v_x(\theta) = -v_\alpha \cos(\theta) + v_\delta \sin(\theta). \tag{3.6}$$

For all values of the rotation angle θ, we then plotted x versus the velocity in x (v_x) and checked for correlation. A positive correlation indicates expansion, while a negative correlation indicates contraction of the cluster. In order to quantify the significance of the expansion/contraction, we first computed the Pearson's correlation coefficient r_{xv_x}, then determined the Student's t-value, and used it to quantify the significance of the correlation. Using bootstrap analysis, we carried out this step 20 000 times for each cluster while adding errors with random weights based on the stars' normally distributed uncertainties in velocity, and then took the t-value of the mean correlation coefficient to determine the significance, which can be seen in Table 3.3. The uncertainties in the velocity of each star were estimated using error propagation for equations 3.1–3.4 and a covariance matrix to take the rotation into account.

We did this for $\theta \in [0°, 179°]$ and determined the angle for which the Student's t-value is maximized, which is the direction of the most significant expansion or contraction. Figure 3.18 shows this for all clusters that have correlation at a significance higher than $1\,\sigma$.

In total, we find indications of expansion/contraction with at least 1σ significance for eight investigated clusters. Four clusters show a significance $\geq 2\,\sigma$, with Tr 14 yielding the highest significance ($5.2\,\sigma$). The clusters generally show signs of expansion; the only exception is NGC 3293, which shows indications of contraction and expansion.

Our expansion analysis results for Tr 14 and 16 agree with the conclusions by Kuhn et al. (2019) who found expansion in the two clusters as well, based on *Gaia* DR2 data. They find low-level expansion for at least $\sim 75\%$ of their analyzed clusters, which agrees with our results that 80% of our investigated clusters show signs of expansion.

Wright et al. (2024) analyzed 18 groups and stellar clusters (including Tr 14 and 16) using data from GES and *Gaia* EDR3. They also found indications of expansion for Tr 16, while they did not find significant expansion or contraction in Tr 14. The differences in their analysis results could be due to different membership selection criteria of stars since the GES observations of Tr 14 go beyond our spatial definition of Tr 14.

The kinematic age of clusters can be calculated by inverting the slope of the fit in the velocity-position plot (see Fig. 3.18). The expansion time and its uncertainty were estimated via bootstrapping (as the significance before) and by inverting the mean of the gradients with added/subtracted standard deviation of the gradients. The kinematic ages are generally rather well consistent with age estimates for the stellar populations of these clusters in the literature (see Table 3.3).

The kinematic analysis for NGC 3293 yields interesting results. Figure 3.19 (f) shows the significance of expansion/contraction according to the angle for NGC 3292. While most

Table 3.3: Car OB1 clusters that show indications of expansion or contraction at least $1\,\sigma$ significance and their kinematic age $\tau_{\rm kin}$.

Cluster	Angle [°]	Expansion			Contraction
		Significance	$\tau_{\rm kin}$ (Myr)	$\tau_{\rm stellar}$	Significance
NGC 3293	38			≈ 10	$2.3\,\sigma$
Tr 14	90	$5.2\,\sigma$	$1.07^{+0.22}_{-0.16}$	≈ 1	
Tr 16	168	$2.8\,\sigma$	$5.19^{+3.14}_{-1.42}$	≈ 3.5	
CCCP-Cl 13	5	$1.5\,\sigma$	$1.09^{+1.38}_{-0.39}$		
Bo 11	99	$1.9\,\sigma$	$0.62^{+0.48}_{-0.19}$	≈ 3–10	
IC 2581	170	$2.3\,\sigma$	$4.80^{+3.92}_{-1.49}$	≈ 12	
NGC 3324	135	$1.2\,\sigma$	$1.98^{+10.30}_{-0.90}$	≈ 11	
UBC 501	48	$1.3\,\sigma$	$4.91^{+7.40}_{-1.84}$	≈ 13	

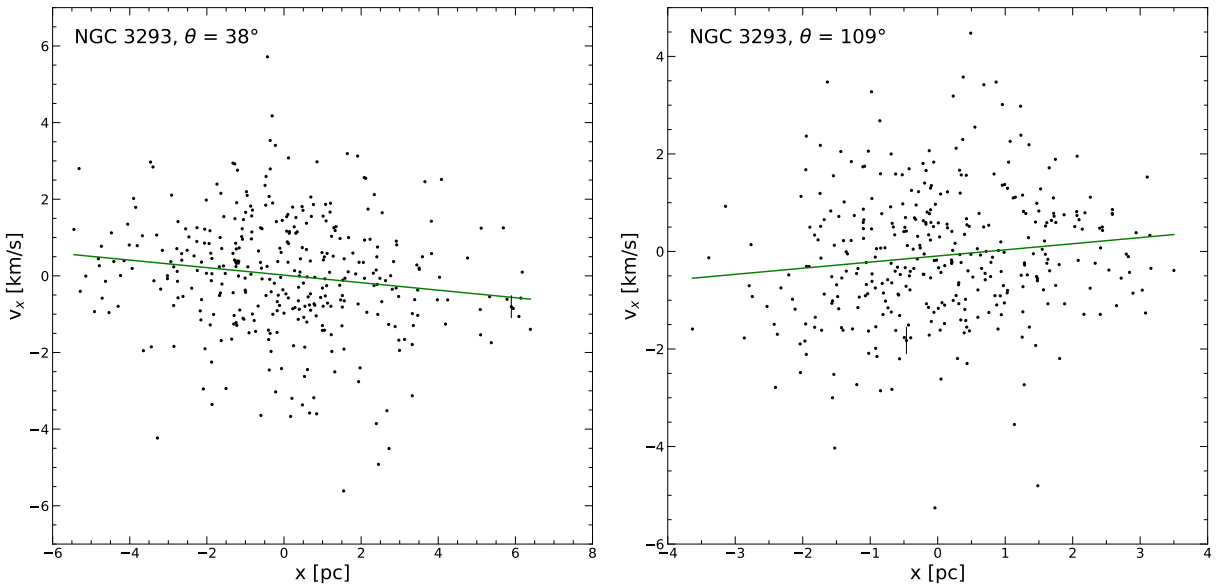

Figure 3.10: Relative position versus relative velocity with its slope for members of NGC 3293 at angles of the primary ($\theta = 38°$, left panel) and secondary significance peak ($\theta = 109°$, right panel).

clusters only show one peak with a significance higher than 1.5σ, only NGC 3293 shows a secondary peak above this threshold at $\theta = 111°$ with a significance of 1.9σ. But while the proper motions show contraction at the primary peak with a significance of 2.3σ (as seen

on the top in Fig. 3.10), the proper motions indicate expansion at an angle of $\theta = 109°$ as shown on the bottom in Fig. 3.10. The directions of contraction and expansion are almost perpendicular to each other and show that NGC 3293 is contracting and expanding at the same time along different axes.

Simulations predict that clusters contract at the beginning of their lifetime and are in their most compact form in their first few Megayears, after which cluster expansion follows (Farias et al., 2024). This is also seen in observational kinematic studies, as Kuhn et al. (2019) conclude that 75% of their investigated clusters show signs of expansion, with only the cluster M17 contracting. As M17 is very young ($\sim$ 1 Myr), they conclude that it is still in the first evolutionary phase of contraction. Della Croce et al. (2024) kinematically analyzed young clusters and found expansion for 80% of their young ($t < 30$ Myr) clusters. This makes the kinematic result for NGC 3293 very interesting as it's at an age of $\sim 10 - 15$ Myr and is therefore expected only to expand.

Ward et al. (2020) analyzed the kinematics of stars in a region of $\sim 0.6° \times \sim 0.45°$ around the stellar cluster NGC 3923 with *Gaia* DR2 and determined a contraction as well at a contraction velocity of 2.67 ± 6.63 km s^{-1}, which is slightly higher than our contraction velocity of 1.32 ± 0.07 km s^{-1} for NGC 3293 at an angle of 38° that was calculated using only stars with proper motions showing contraction.

3.5 New OB star candidates in Car OB1 from *Gaia*

As mentioned in the introduction, the sample of known high-mass members of Car OB1 is not yet complete, especially in the regions between and around the well-studied known clusters and the peripheral regions of the association. We therefore used the *Gaia* main catalog and the additional `astrophysical_parameters` catalog to perform a spatially unbiased search for further high-mass members of Car OB1 over the full area of the association. Our aim was to identify still unidentified OB stars in Car OB1, to find out how large the total population of high-mass stars is, to ascertain how far the OB association extends, and to analyze the distributed OB star population.

The *Gaia* database provides estimates of spectral types and stellar parameters for some stars based on *Gaia* BP/RP spectra with five effective temperature estimates based on different models and data. Here we only use `teff_gspphot` and `teff_esphs` as `teff_gspphot` is the temperature estimation that is available for most stars in Car OB1, while `teff_esphs` is focused on stars with spectral types O, B, and A.

To assess how useful and reliable the *Gaia* temperature estimates are, we compare them to the effective temperatures according to their spectral type for our sample of spectroscopically identified OB stars in Car OB1 (see Sect. 3.3.5). For the effective temperatures from the spectral type, we used the observational scales provided by Martins et al. (2005) for O-type stars and the scale from Pecaut & Mamajek (2013) for B-type stars.

Figure 3.11 shows the comparison for `teff_esphs`. We find the best agreement between the spectral type and derived effective temperatures for the parameter `teff_esphs` (compared to the other *Gaia* derived effective temperatures), which was to be expected

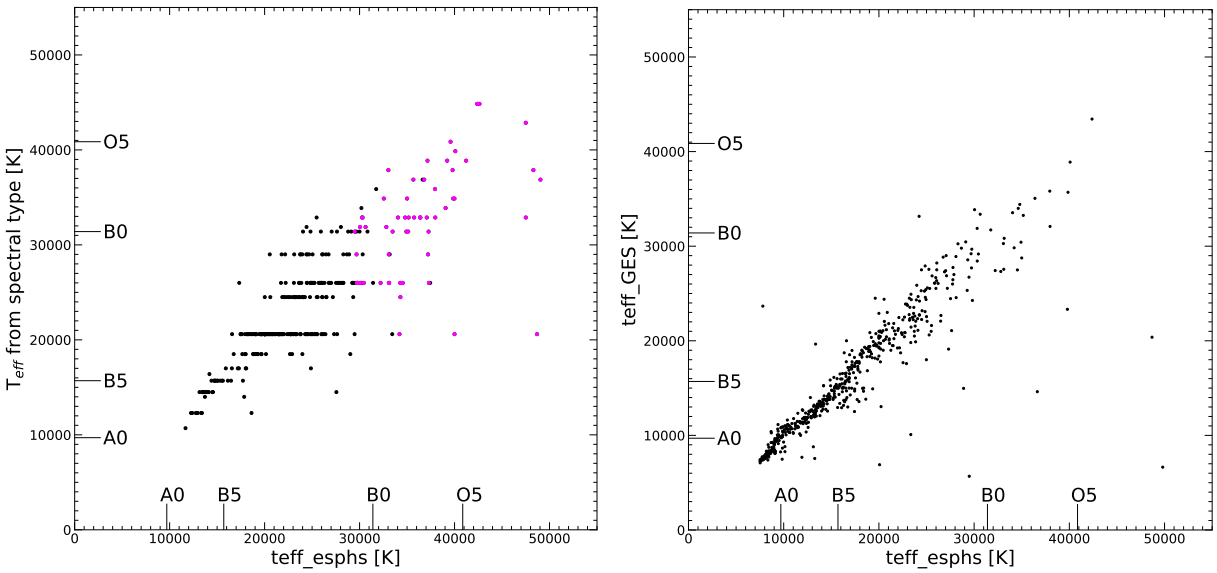

Figure 3.11: Comparison of `teff_esphs` with the effective temperature expected from the spectral type and the effective temperature given in GES. Left panel: Effective temperature from spectral types versus the *Gaia* DR3 effective temperature `teff_esphs` for the Car OB1 high-mass star sample. The stars highlighted in magenta have `spectraltype_esphs` O. Right panel: *Gaia* DR3 effective temperature `teff_esphs` versus effective temperature from GES for stars in the region of Car OB1.

because only stars that were classified as O, B, or A stars by *Gaia* were processed. Ulla et al. (2022) also report that `teff_esphs` performs better than `teff_gspphot` for hot stars since it takes corrections for the $T_{\rm eff}$-extinction degeneracy into account.

We also compare `teff_esphs` with effective temperatures from the *Gaia*-ESO Survey (GES), which is shown in Fig. 3.11 on the right. In the context of the GES, optical high-resolution spectra were obtained for 2875 stars in the region of Car OB1, and effective temperatures for 1817 of these stars were derived. 572 of these stars also have a `teff_esphs` value in the *Gaia* database available. We can see that there is generally good agreement (with a median absolute difference of 668 K) between the effective temperatures derived by *Gaia* and GES, but there are some outliers. In general, we consider effective temperatures derived in the GES to be more reliable than *Gaia* `teff_esphs` values, since their GES parameters are based on spectra with higher resolution. For stars that have both temperature estimations, we therefore favor the effective temperature in GES. Four stars with `teff_esphs` $> 35\,000$ K (i.e., suggesting an O spectral type) have $T_{\rm eff,GES} < 25\,000$ K (suggesting a mid-late B spectral type).

3.5.1 Identifying new OB star candidates in the Car OB1 association

We used two approaches to find new candidate OB stars: In the first approach, we applied DBSCAN on the sample of stars with `spectraltype_esphs` O or B, and `teff_esphs` $\geq$ 17 000 K, in order to see whether we can find further association members by the coherent parallaxes and proper motions as expected for members of an association.

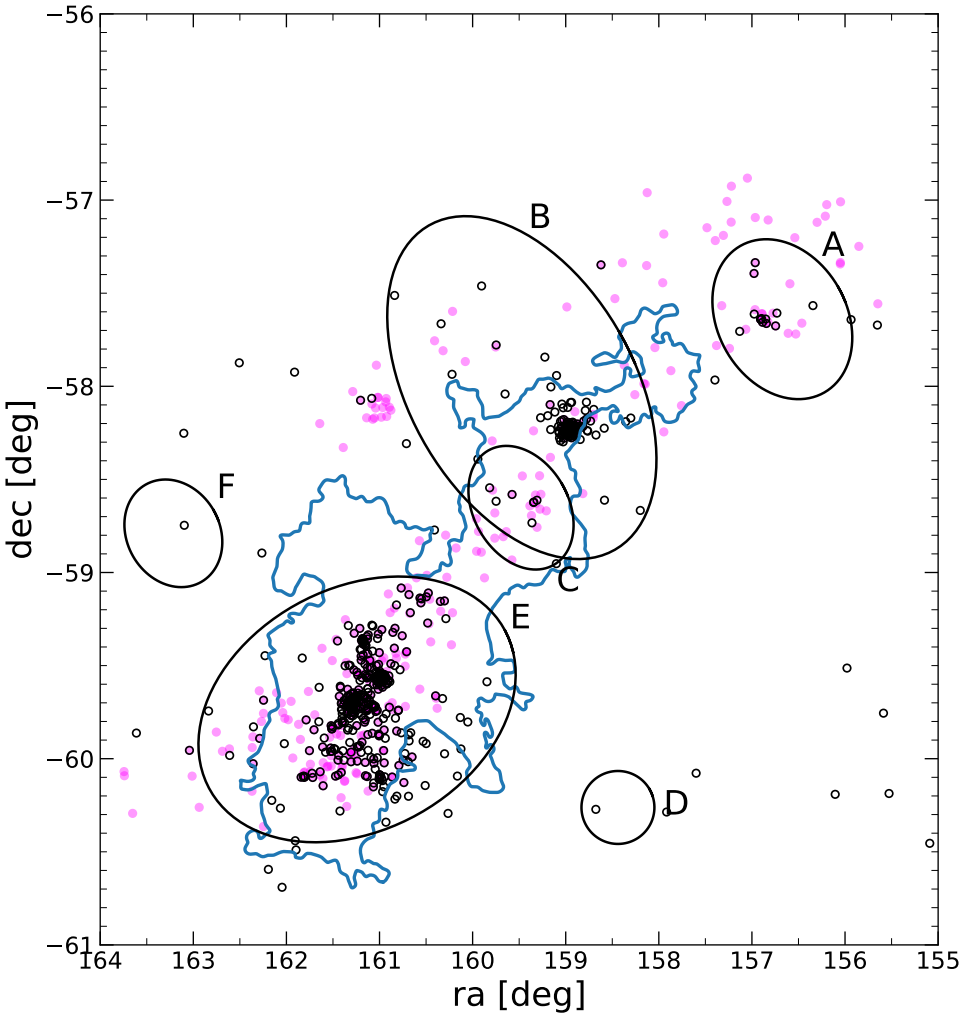

Figure 3.12: Map of the Car OB1 high-mass stars and OB candidates. The Car OB1 high-mass star sample is in black and *Gaia* stars with `teff_esphs` $\geq$ 17 000 K, which were identified by DBSCAN in the region of Car OB1, are in magenta. The Car OB1 subgroups from Mel'Nik & Efremov (1995) are shown as ellipses.

We started by selecting stars inside a box centered around the Carina Nebula with 25° side length, `spectraltype_esphs` O or B, and `teff_esphs` > 17 000 K in *Gaia* DR3. This leads to a sample containing 12 915 stars. We then applied the clustering algorithm

DBSCAN to the stars while using the same method as in Sect. 3.3.1 to determine the density parameter ϵ.

Figure 3.12 shows the stars that were identified by DBSCAN in an overdensity that has a similar distance as Car OB1. DBSCAN recovered Car OB1 as four overdensities, with the Carina Nebula as one large overdensity, the clusters NGC 3293 and IC 2581 as another one, while the clusters UBC 501 and NGC 3324 were identified as separate clusters. The stars of our Car OB1 high-mass sample are plotted in black and show that the association found by DBSCAN extends farther north and north-west than our Car OB1 high-mass sample. DBSCAN also identified Car OB1 members in the region of the cluster UBC 501, which has only one cluster member in our Car OB1 high-mass star sample.

In total, 497 stars were identified by DBSCAN to be part of Car OB1, out of which 472 (95%) have a 2σ distance interval, which is consistent with the distance of Car OB1. Of these stars, 215 (46%) lie inside one of the cluster circles defined in Sect. 3.3.5 and can therefore be regarded as members in one of the clusters. The remaining 257 (54%) stars can be interpreted as the distributed population in Car OB1. This leads to a ratio of 46:54 of clustered versus distributed population.

The 235 stars identified by DBSCAN as association members were already part of our Car OB1 high-mass star sample and thus are spectroscopically confirmed high-mass stars. The other 237 stars have not been assigned to Car OB1 before. We searched for spectral types for the 237 OB candidates and found spectral types for 38 stars (2 O-, 16 B-, 3 A-, and 17 OB-type), while 199 stars have no spectroscopically determined spectral type available in Simbad. Out of these 199 stars, 20 have an effective temperature in GES.

We excluded ten stars as their GES effective temperature is below our cutoff temperature of 17 000 K. We classify stars with no available spectral type as O star candidates if `teff_esphs` $>$ 31 900 K (effective temperature of an O9.5 V star according to Martins et al. (2005)), which leads to 5 new O-type and 184 new B-type candidates.

Figure 3.13 shows on the left a color-magnitude diagram of the Car OB1 high-mass star sample and the DBSCAN identified *Gaia* OB candidate population. The blue arrows show the reddening arrows of a B0 and an A0 star, we can see that all new *Gaia* OB candidates in Car OB1 lie above the A0 arrow and have photometry consistent with being an O- or B-type star.

3.5.2 Revealing the distributed population of OB stars in Car OB1 with *Gaia*

In the second approach, we considered all stars in the area with `spectraltype_esphs` O or B and `teff_esphs` $\geq$ 17 000 K, and selected those stars that have parallaxes consistent with being members of Car OB1. This approach can also identify stars with proper motions deviating from the typical values of the association, as may be the case for "run-away" stars, for example, and it allows us to find more of the distributed Car OB1 population.

Figure 3.14 shows a two dimensional spatial histograms of stars in *Gaia* DR3 whose 2σ distance interval overlaps with the distance interval of Car OB1 ([2.25, 2.45] kpc) and

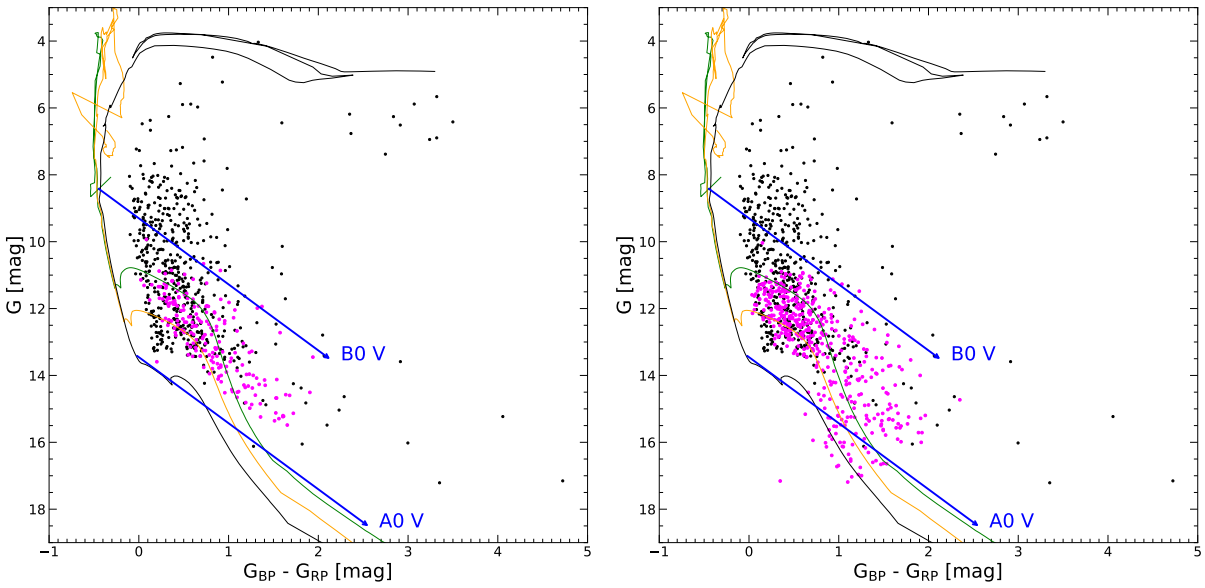

Figure 3.13: *Gaia* CMD of the Car OB1 high-mass stars in black and OB candidates in magenta. PARSEC v3.7 isochrones (Bressan et al., 2012) at ages 1 Myr (green), 3 Myr (red), and 10 Myr (black) are overplotted. The arrows show the reddening vectors of a 1 Myr old B0 and a 10 Myr old A0 star for $A_V = 6$ mag. Left panel: OB starcandidates are selected with DBSCAN and with `teff_esphs` $\geq 17\,000$ K. Right panel: OB star candidates are selected from Fig. 3.14.

which have `teff_esphs` $> 17\,000$ K. The whole Car OB1 can be seen as an overdensity with densities peaking in the central regions of Tr 14 and 16.

A clear density decrease from the central Carina Nebula and the surrounding clusters toward the periphery of the field can be seen. The star density shows a strongly elongated shape, following the large-scale structure of the association (Fig. 3.14). Figure 3.14 reveals numerous new OB star candidates around the already known members of the association, and highlights the distributed population that had remained largely unidentified so far.

The selection of stars in a box of $5^\circ \times 5^\circ$ centered around $(10^\mathrm{h}40^\mathrm{m}48^\mathrm{s}, -59^\circ)$ with a 2σ distance interval overlapping with the distance interval of Car OB1 and `teff_esphs`$>$ $17\,000$ K (as seen in Fig. 3.14) yields in total 1233 stars, with 306 being already a part of the Car OB1 high-mass star sample, and 237 identified as Car OB1 members in Sect. 3.5.1. Out of the 690 new OB candidates, 233 have spectral types available in Simbad, including 2 O-, 186 B-, and 15 A-type stars, and 30 stars with spectral type OB. Figure 3.13 shows on the right a color-magnitude diagram for the 457 stars without available spectral type. Almost all stars (92%) have optical photometry compatible with being an O- or B-type star. The 37 stars that are located below the reddening vector of an A0 V star are excluded from our list of possible OB candidates. The GES catalog contains effective temperature values for 7 stars in this sample, which leads to the exclusion of 5 stars as their GES effective temperature is below $17\,000$ K. This leads to 415 new OB star candidates in the

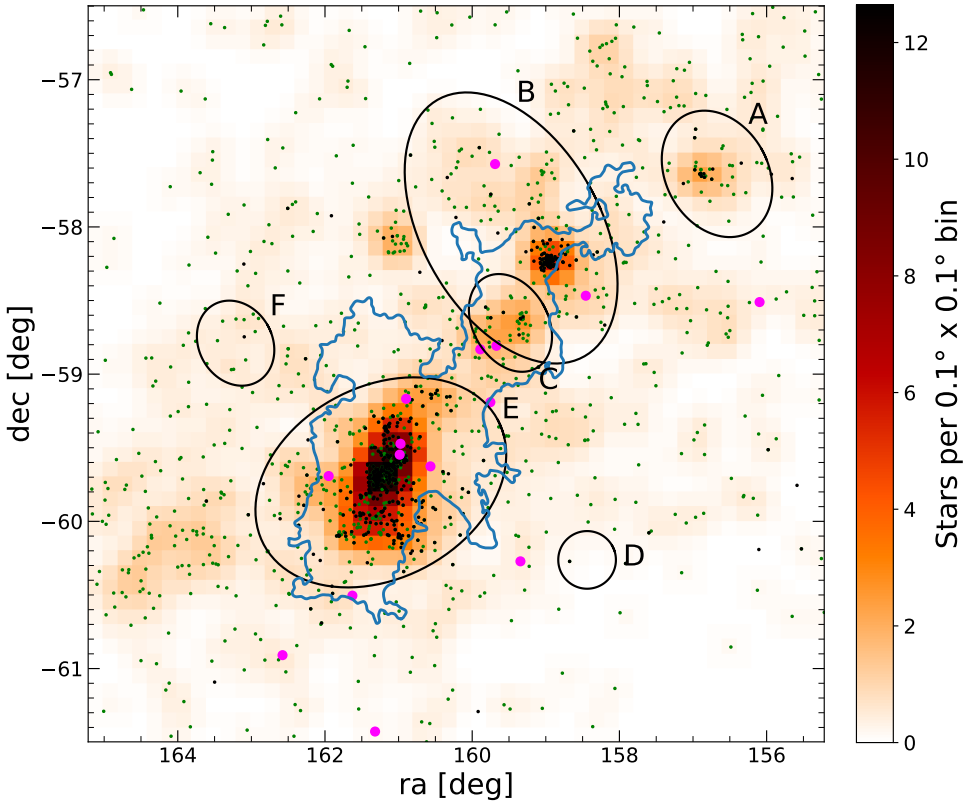

Figure 3.14: Map of smoothed two-dimensional spatial histograms of stars with a compatible distance to Car OB1 and `teff_esphs` $\geq 17\,000$ K. The Car OB1 subgroups from Mel'Nik & Efremov (1995) are shown as ellipses, and the CNC contour is in blue. Stars with compatible distance and `teff_esphs` in green, stars from the Car OB1 high-mass star sample in black, and new O-type candidates in magenta.

region of Car OB1, with 10 being O-type candidates, 405 B-type candidates, and 218 spectroscopically identified stars in the Car OB1 region.

If all of these 604 new OB candidates from Sects. 3.5.1 and 3.5.2 are actually high-mass stars in Car OB1, then the ratio of clustered versus distributed population would be 26:74 (compared to 58:42 for the Car OB1 high-mass star sample, and 46:54 for the DBSCAN-selected Car OB1 population). An $\sim 75\%$ fraction of distributed stars may appear quite high, but we note that similar fractions have been reported for other OB associations (e.g., for Sco OB2, a ratio of 14.5:85.5 was reported by Damiani et al. (2019)). All new OB star candidates are listed in Table 3.6 and are labeled with 'TD' for stars from Sect. 3.5.1 and 'T' for stars from Sect. 3.5.2 in the column 'Selection'.

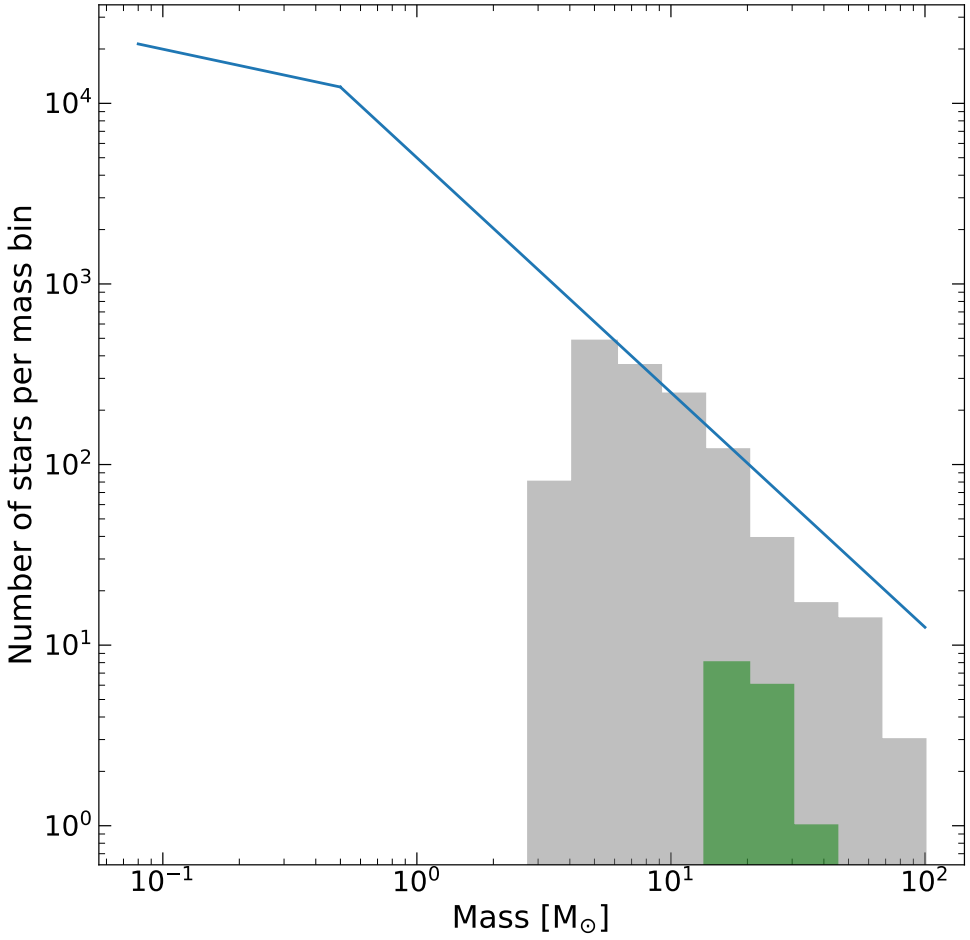

Figure 3.15: Histogram of the masses of the stars for our Car OB1 high-mass star sample combined with the new identified OB star candidates from Sects. 3.5.1 and 3.5.2. A fit of the Kroupa (2001) IMF is shown in blue. The contribution by our new O-type candidates is shown in green.

3.5.3 An estimate of the total stellar mass of Car OB1

In order to investigate the mass function and to obtain an estimate of the total number of stars in Car OB1, we have combined our Car OB1 high-mass star sample with our new OB star candidates in the Car OB1 region from Sects. 3.5.1 and 3.5.2 which yields a total sample of 1374 stars which includes 92 O-type, 3 WR, 36 supergiants, and one luminous blue variable star (η Car). We have converted spectral types to masses with the table from Pecaut & Mamajek (2013). Stars selected by `teff_esphs` were taken into account by translating stellar temperatures to stellar masses with tables provided by Martins et al. (2005) and Pecaut & Mamajek (2013). We have used mass determinations provided in the literature (Hamann et al., 2019; Sander et al., 2019; Gruner et al., 2019; Strawn et al., 2023) for the 3 WR stars in our sample, HD 93129 A, and η Car. We have not included

supergiants in our IMF plot (Fig. 3.15) since the exact masses of supergiants are difficult to determine due to winds and high mass loss rates.

Figure 3.15 shows a histogram of the stars' masses and an approximate fit of a Kroupa IMF. The slope of the IMF agrees well with the histogram for masses between ≈ 4 and $20.5\,M_\odot$ while it predicts more stars at higher masses than are present in our sample. This discrepancy is probably caused by the missing 36 supergiant stars due to their highly uncertain masses. Based on the observed mass function between ≈ 8 and $20.5\,M_\odot$ with 367 stars in our combined Car OB1 sample, an extrapolation based on the Kroupa IMF leads to a total number of $\approx 79\,800$ stars with masses from $0.08\,M_\odot$ to $100\,M_\odot$, and a total stellar mass of $\approx 45\,800\,M_\odot$ in Car OB1. An extrapolation based on the 140 stars (including the 36 supergiants) with masses $> 18\,M_\odot$ leads to a total number of $\approx 69\,100$ stars with masses from $0.08\,M_\odot$–$100\,M_\odot$ and a total stellar mass of $\approx 39\,600\,M_\odot$ in Car OB1. It is important to note that both estimates are only lower limits because the cloud complex contains numerous obscured stars. The sample of stars identified by optical spectroscopy, and also the Gaia-based sample, is certainly incomplete to some degree.

Our estimate of a total population of $N \sim 8 \times 10^4$ stars in Car OB1 is in good agreement with the extrapolation based on the number of X-ray detected young stars by Feigelson et al. (2011). It also confirms Car OB1 as probably being the most massive of the well-studied OB associations in our galaxy. Our results suggest Car OB1 being substantially more massive than Cyg OB2 (with a total stellar mass of $\sim 16\,500\,M_\odot$; Wright et al., 2015), which was considered to be the probably most massive OB association in our galaxy by Wright (2020), and also exceeding the total stellar mass of $\sim 36\,200\,M_\odot$ for the Per OB1 association estimated by Melnik & Dambis (2020). Car OB1 is therefore comparable to the star-forming region 30 Doradus in the Large Magellanic Cloud, which is the most luminous star-forming region in our Local Group (Kennicutt, 1984), with a total stellar mass of $110\,000\,M_\odot$ (Doran et al., 2013).

3.6 Large-scale kinematics and expansion of the Car OB1 association

3.6.1 Expansion of Car OB1

Previous studies of Car OB1 (see Melnik & Dambis, 2020) found an expansion of the association. In order to confirm and quantify this expansion with our stellar samples, we analyze the kinematics of the stars in the Car OB1 association. For this, we combine the stars from our high-mass Car OB1 sample with the kinematically coherent OB star candidates, which were identified by DBSCAN in Sect. 3.5.1, yielding a total sample of 741 stars. We plot the high-mass stars' proper motions relative to the center as arrows to visualize the kinematics of the association as shown in Fig. 3.16. The stars are divided into three categories according to the angle between the vector of their relative proper motion and the vector of the star's position to the association's center. Stars whose proper motions are directed outward (angles between 120° and 240°) are shown in blue, inward (angles

between 300° and 60°) in red, and moving tangentially around the cluster (angles between 240° and 300° or between 60° and 120°) in yellow. Most arrows in Fig. 3.16 are in blue and pointing outward (572, 77%) while there are fewer stars whose proper motions are pointing inward or rotating (101 and 63, respectively), which indicates that the whole Car OB1 association is expanding. The relative proper motions show an expansion of the whole association and also confirm that members of the cluster UBC 501 have consistent proper motions with an expansion of the association, which validates UBC 501's membership in the Car OB1 association.

In order to determine the outward velocity of the association, we have calculated the projected outward velocity of each star with respect to the association's center and taken the mean, which results in a velocity of $v_{\rm out} = 5.25 \pm 0.02$ km s^{-1} for Car OB1. A large part of the stars with positive outward velocity (291 out of 612) move out at an angle between $12 \pm 15°$ with respect to the galactic plane, which we assume to be the expansion angle of the whole association. Taking only stars which are contributing to the expansion, this results in an expansion velocity of 7.05 ± 0.03 km s^{-1} at an angle of 12° in galactic coordinates. This expansion follows along the elongation of the CNC cloud complex as shown in Fig. 3.16. Interestingly, this expansion angle of Car OB1 at 42° (in ecliptic coordinates) is close to the angle of 38° at which NGC 3293 contracts.

Melnik & Dambis (2020) investigated 28 OB associations using *Gaia* DR2 and found clear evidence of expansion (significance $> 3\sigma$) for 9 associations (32%) including Car OB1, Ori OB1, and Sco OB1. They determined an expansion velocity of 5.0 ± 1.7 km s^{-1} for Per OB1, which is similar to the expansion velocity we estimated for Car OB1.

3.6.2 Traceback analysis of Car OB1

In order to investigate the temporal evolution of the spatial extent of Car OB1, we performed a traceback analysis for the stars in our combined Car OB1 star sample. We used the epicyclic equations from Fuchs et al. (2006) to approximate the motion of the stars. They are given in galactocentric coordinates XYZ with galactic space velocities UVW:

$$\begin{aligned} X(t) &= X(0) - \frac{V(0)}{-2B}\,(1 - \cos(\kappa\,t)) + \frac{U(0)}{\kappa}\sin(\kappa\,t) \\ Y(t) &= Y(0) + 2\,A\,\left(X(0) - \frac{V(0)}{-2B}\right)\,t \\ &\quad + \frac{\Omega_0}{-B\,\kappa}\,V(0)\sin(\kappa\,t) + \frac{2\Omega_0}{\kappa^2}\,U(0)\,(1 - \cos(\kappa\,t)) \\ Z(t) &= \frac{W(0)}{\nu}\sin(\nu\,t) + Z(0)\cos(\nu\,t). \end{aligned} \tag{3.7}$$

Here A and B are the Oort constants, and Ω_0 the angular velocity of the sun's circular orbit. κ is the epicyclic frequency and is defined as $\kappa = \sqrt{-4\,\Omega_0\,B}$, while ν is the vertical oscillation frequency and is defined as $\nu = \sqrt{4\,\pi\,G\,\rho_0}$ with G as the gravitational constant and ρ_0 as the local density. We have used values of $A = 15.1 \pm 0.1$ km s^{-1} kpc^{-1},

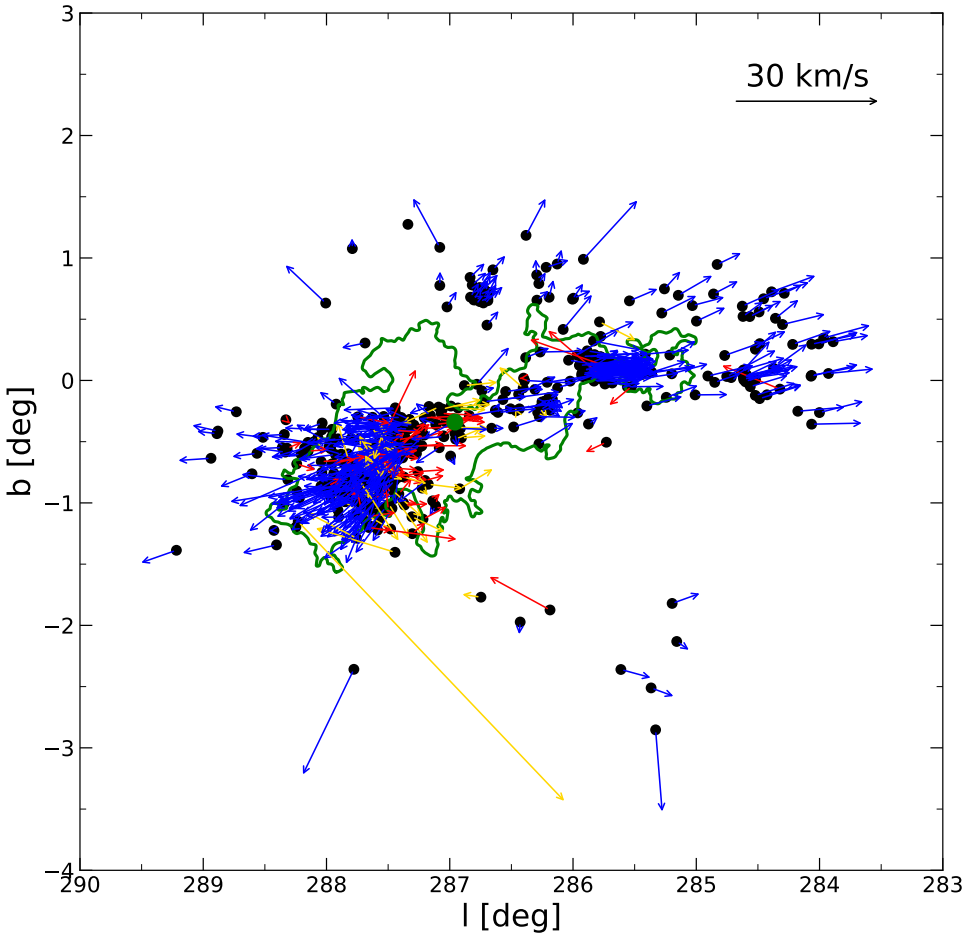

Figure 3.16: Relative proper motions of the stars in our combined Car OB1 high-mass star sample. Motions pointing outward are shown with blue, inward motions with red, and rotating motions with yellow arrows. The green dot represents the association's center, and the green contour the outline of the CNC.

$B = -13.4 \pm 0.1$ km s^{-1} kpc^{-1}, and $\Omega_0 = 28.5 \pm 0.1$ km s^{-1} kpc^{-1} (Li et al., 2019), and $\rho_0 = 0.102$ M$_\odot$ pc^{-3} (Holmberg & Flynn, 2004). We used the median radial velocity of -7.1 ± 5.4 km s^{-1} and a distance of 2.35 ± 0.1 kpc for all stars for the conversion to galactocentric coordinates in order to minimize the effect of the greater uncertainty in measurements in the line-of-sight direction.

Following the method described in Quintana et al. (2023), we explored at which time the association had its smallest extent. For this, we traced back the stars' position using equations 3.7 in steps of 0.1 Myr. At each time step, we calculate and save the median absolute deviation to the association's center in XYZ coordinates. The smaller the median absolute deviation, the compacter is the association. In order to derive uncertainties, we add errors with randomly normally distributed weights to each variable and carry out the calculation 1000 times at each time step. We then save the median and standard deviation

of the median absolute deviation at each time step and plot it over time as seen in the upper plot in Fig. 3.17.

We also quantified the spread of the association over time with two more measures of dispersion: the standard deviation of the association (middle plot in Fig. 3.17) and the mean distance between all stars in the sample (lower plot in Fig. 3.17). All dispersion measures give similar results, with a minimum around 3–4 Myr.

Although there is clear evidence for large-scale expansion of Car OB1 during the last 3–4 Myr, we note that the absolute change of the spatial extension during this time period is relatively moderate: the current extent of the stellar populations is ≈ 220 pc, and during the time of the minimum, the extent was ≈ 190 pc. This result is in agreement with the conclusions from Ward et al. (2020), who found that the expansion seen in most OB associations cannot be interpreted as the expansion of one initial monolithic dense cluster. OB associations are thus not the product of an expanding cluster, but instead originate from a large-scale, globally unbound, and highly substructured initial configuration. A more detailed analysis of the temporal evolution of the full Car OB1 association and its individual components will be the topic of a separate study.

3.7 Conclusions and summary

The main results of our astrometric analysis of the high-mass stars over the full extent of the Car OB1 association can be summarized as follows:

1. Applying a cluster-finding method to the *Gaia* DR3 data of the area, we have found 15 clusters and groups that have a spatial position, distance, and age compatible with Car OB1. Four identified groups in Car OB1 were not mentioned in the literature before. Seven of our recovered clusters, including the well-known clusters Tr 14, 15, and 16, NGC 3324, IC 2581, and Bo 11, are split into subclusters. We also find that the cluster UBC 501 is part of Car OB1. We find that subgroups A, B, C, and E of Car OB1, which were identified by Mel'Nik & Efremov (1995), agree well with our distribution of clusters, while we did not detect any clusters or groups with a compatible distance that are located in or near subgroups D and F.

2. We have assembled a new census and collected the largest sample of high-mass stars with a known spectral type in Car OB1 so far, with 517 stars (including 88 O-type stars, three WR stars, and 36 supergiant stars) that have compatible distances. Our census of Car OB1 provides a very substantial extension in the area covered and the star numbers compared to previously published censuses by Smith (2006a) (70 O-type and WR stars) and by Berlanas et al. (2023) (80 O-type, WR, and supergiant stars), both of which were restricted to the central Carina Nebula.

3. We analyzed the kinematic properties of the clusters and found signs of expansion or contraction for 80% of the clusters in Car OB1 at a level of at least 1σ significance. The clusters Tr 14 and 16 show clear evidence of expansion at 5.2σ and 2.8σ,

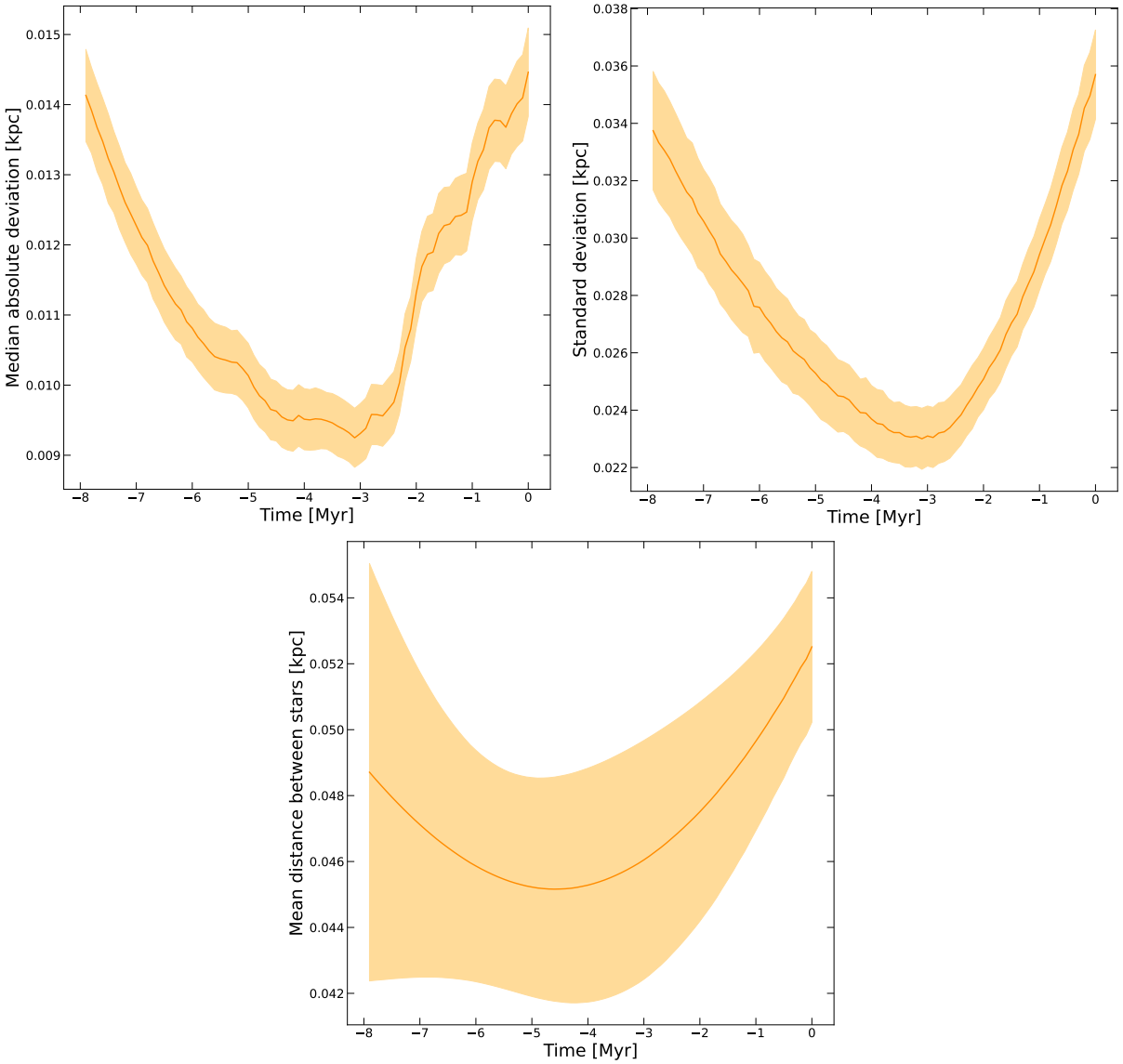

Figure 3.17: Three methods to trace the size of Car OB1 over time. The methods are median absolute deviation of the stars' position to the association's center (left panel), standard deviation of the association (middle), and mean distance between all stars (right).

respectively, while NGC 3293 contracts at a level of 2.3σ. The derived kinematic ages for the clusters agree well with (previously estimated) ages in the literature and isochrone fittings to color-magnitude diagrams.

4. We combined the full *Gaia* astrometry with *Gaia* spectral types (`spectraltype_esphs`) and effective temperatures (`teff_esphs`) in order to search for new OB star candidates and constrain the distributed OB population over the full spatial extent of the Car OB1 association, including poorly studied regions outside of the prominent star clusters. This led to 604 new OB candidates, resulting in a total sample of 857 OB candidates and association members in Car OB1. In a literature search of these candidates, we found a spectroscopic identification as an O- or B-type star for 253 (35 from Sect. 3.5.1 and 218 from Sect. 3.5.2) of the candidates, including four O-type stars. For the remaining 604 candidates, we classified 15 as O-type candidates and 589 as B-type candidates according to their effective temperatures (`teff_esphs`) listed in the *Gaia* data.

   The fraction of OB stars in a spatially non-clustered distributed population increases to 54% (Sect. 3.5.1) and 74% (Sect. 3.5.2), respectively, when the new OB star candidates are taken into account. Extrapolating the Kroupa IMF, based on the Car OB1 high-mass star sample and OB candidates, down to $0.08\,M_{\odot}$, we estimate that Car OB1 contains a total population of at least $\sim 8 \times 10^4$ stars.

5. We also ascertained that the whole Car OB1 association is expanding at a velocity of $v_{\rm out} = 5.25 \pm 0.02$ km s^{-1} by examining the kinematics of the Car OB1 high-mass stars. Using the positions and proper motion of the high-mass Car OB1 stars allowed us to kinematically trace back the association, and it shows that the spatial extent had a minimum about 3–4 Myr ago.

In this chapter, we present a comprehensive OB star and cluster catalog of the full association and show that the association reaches beyond the Carina Nebula. To study the evolution of the association, it is therefore necessary to take the full extent of Car OB1 into account.

3.A Kinematical analysis without correction factor

Table 3.4 shows a comparison of the kinematical analysis from Sect. 3.4 with and without the correction factor. It can be seen that the correction factor has only a small influence on the end result.

3.B Supplemental plots and previews of tables

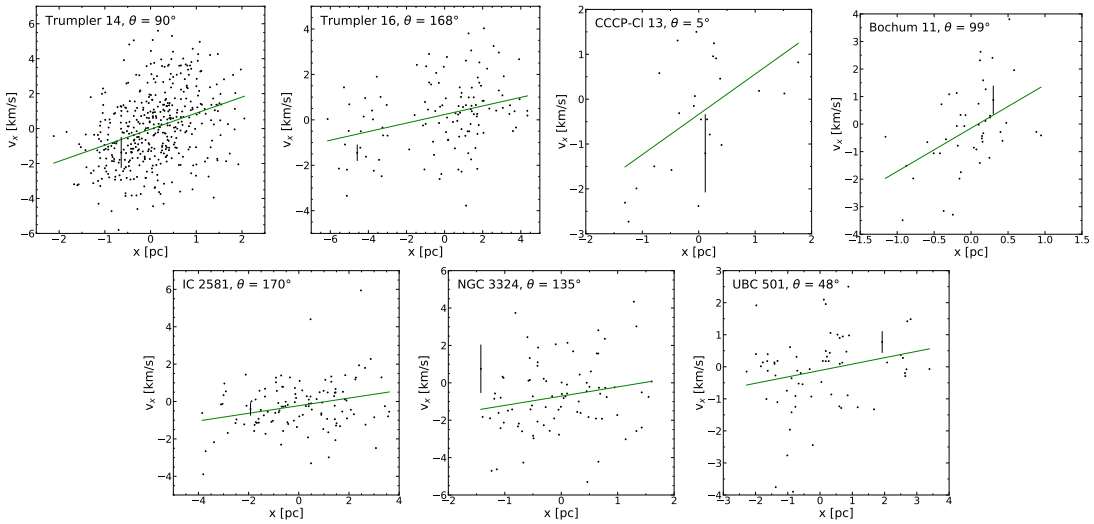

Figure 3.18: Cluster members' relative position versus relative velocity with its slope at the angle of highest significance. The vertical black line shows the cluster's median uncertainty in velocity. Panel (a): Tr 14, (b): Tr 16, (c): CCCP-Cl 13, (d): Bo 11, (e): IC 2581, (f): NGC 3324, (g): UBC 501

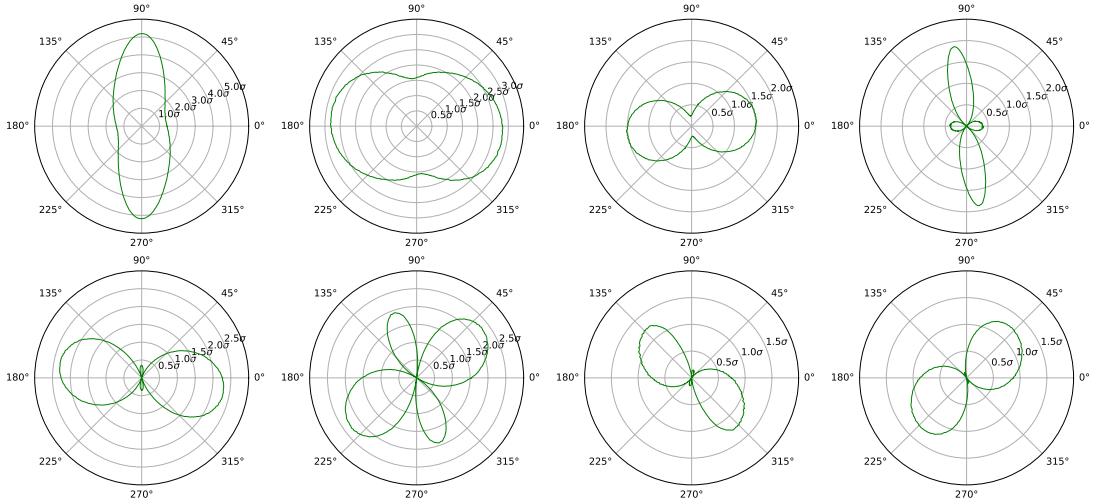

Figure 3.19: Significance of the correlation between position and velocity for angles between 0° and 359°. Panel (a): Tr 14, (b): Tr 16, (c): CCCP-Cl 13, (d): Bo 11, (e): IC 2581, (f): NGC 3293, (g): NGC 3324, (h): UBC 501.

Table 3.4: Comparison of kinematical results for clusters with and without correction factor.

Cluster	With correction			Without correction		
	Angle [°]	Expansion Significance	Contraction Significance	Angle [°]	Expansion Significance	Contraction Significance
NGC 3293	38		$2.3\,\sigma$	38		$2.3\,\sigma$
Tr 14	90	$5.2\,\sigma$		90	$5.2\,\sigma$	
Tr 16	168	$2.8\,\sigma$		176	$2.8\,\sigma$	
Tr 15	148	$0.9\,\sigma$		149	$0.9\,\sigma$	
Cr 228	54	$0.8\,\sigma$		58	$0.8\,\sigma$	

Table 3.5: Clusters found with DBSCAN in the region of the Car OB1. The clusters are listed with their member size, weighted position, weighted proper motion, weighted mean parallax with its uncertainty, mean *Kalkyotl* distance with its central 68.3% quantile, their counterpart in literature with reference, if the cluster is part of the Car OB1, and if the cluster is a substructure, if available. This table is available in its entirety in electronic form at the CDS.

Cluster	NMem	RA	Dec	μ_α^* [mas yr^{-1}]	μ_δ [mas yr^{-1}]	$\varpi \pm \sigma_\varpi$ [mas]	$D_{Kalkayotl}$ [kpc]	Counterparts	Reference Counterpart	Part of Car OB1?	Clusters associated
1	11	10:17:34.52	−56:52:40.9	−5.800	3.267	0.279 ± 0.032	3.706 [3.275,4.135]			N	
2	15	10:17:52.57	−57:15:53.0	−5.435	3.600	0.238 ± 0.010	4.253 [3.971,4.539]			N	3,8,10
3	17	10:17:53.14	−57:20:20.6	−5.595	3.020	0.252 ± 0.011	4.022 [3.773,4.271]			N	2,8,10
4	10	10:18:03.98	−57:25:52.3	−5.556	3.431	0.209 ± 0.015	4.884 [4.455,5.312]			N	
5	10	10:18:13.79	−61:40:20.0	−3.740	2.443	0.058 ± 0.031				N	
6	11	10:18:14.06	−57:21:02.8	−6.901	3.842	0.350 ± 0.014	2.874 [2.739,3.009]			N	
7	10	10:18:18.93	−59:46:56.7	−4.838	2.866	0.115 ± 0.033				N	2,3,10
8	10	10:18:20.41	−57:16:01.8	−5.551	3.287	0.273 ± 0.020	3.730 [3.423,4.031]			N	
9	36	10:18:21.48	−59:49:18.1	−5.029	2.757	0.252 ± 0.007	3.994 [3.778,4.211]	CWNU 2300	2023A&A...673A.114H	N	
10	28	10:18:25.80	−57:19:03.5	−5.529	3.178	0.225 ± 0.014	4.530 [4.166,4.895]	HSC 2325	2023A&A...673A.114H	N	2,3,8

Table 3.6: The table contains the stars' astrometric parameters, `teff_esphs`, spectral type, to which population (clustered or distributed) a star belongs, and how the star was selected. The table is available in its entirety in electronic form at the CDS.

Gaia DR3 Designation	Name	RA	Dec	$\varpi \pm \sigma_\varpi$ [mas]	`teff_esphs` [K]	Spectraltype	SpT Reference	Population	Selection
5350357519345171200	HD 93162	10:44:10.37	−59:43:11.1	0.456 ± 0.020		O2.5 If*/WN6	2014ApJS..211...10S	C	L
5254268071479968512	HD 93131	10:43:52.24	−60:07:04.0	0.380 ± 0.023		WN6ha-w	2006A&A...457.1015H	C	L
5350370026290390912	HD 92740	10:41:17.50	−59:40:36.8	0.402 ± 0.022		WN7h + O9III-V	2006A&A...457.1015H	D	L
5350357313186767104	HD 93205	10:44:33.72	−59:44:15.4	0.443 ± 0.025	42623.5	O3.5 V((f)) + O8 V	2014ApJS..211...10S	C	L
5350383460949215232	HD 93250	10:44:45.01	−59:33:54.6	0.424 ± 0.020		O4 III((fc))	2014ApJS..211...10S	C	L
5350358683250920704	HDE 303308	10:45:05.90	−59:40:05.9	0.455 ± 0.021	47500.0	O4.5 V((fc))	2014ApJS..211...10S	C	L
5350357205782177664	HD 93204	10:44:32.32	−59:44:31.0	0.436 ± 0.023	40080.8	O5.5 V((f))	2014ApJS..211...10S	C	L
5350357519345176192	ALS 15210	10:44:13.18	−59:43:10.2	0.416 ± 0.014		O3.5 If*Nwk	2014ApJS..211...10S	C	L
5350356419839915904	CPD −59 2600	10:44:41.78	−59:46:56.4	0.403 ± 0.023		O6 V((f))	2014ApJS..211...10S	C	L
5350358069101053184	CPD −559 2603	10:44:47.29	−59:43:53.2	0.381 ± 0.021	31747.8	O7.5 V(n)z + B0 V(n)	2014ApJS..211...10S	C	L

CHAPTER 4

OBSERVATIONAL CHARACTERIZATION OF CLUSTER EXPANSION

C. Göppl, T. Preibisch, and A. Burkert

4.1 Introduction

As clusters lose their gas reservoir through protostellar outflows, winds from high-mass stars, and supernovae, they reduce their cluster potential. Open clusters are therefore expected to expand and dissipate over time due to tidal forces from the galactic potential (Krumholz et al., 2019).

Recent analyses of *Gaia* proper motions of the stars in young stellar clusters have shown correlations between the stellar position (relative to the cluster center) and the proper motion along the position axis (Kuhn et al., 2019; Della Croce et al., 2024; Göppl & Preibisch, 2025). If a significant correlation is found, this is usually interpreted as evidence for cluster expansion or contraction along this direction.

However, for clusters at distances > 1 kpc, the uncertainties of the Gaia proper motions are often rather large, and might perhaps in some cases just produce a random correlation. In order to check how reliably an expansion (or contraction) can be inferred from observational data, we use here kinematic data from simulated clusters and perform cluster expansion analysis with realistic observational uncertainties. The aim is to find out how often an apparently significant expansion is found for the virialized cluster, which would then be interpreted as (false-positive) evidence for expansion or contraction, and whether and at what significance we can recover the real underlying expansion of an expanding cluster.

We introduce our stellar cluster model in Sect. 4.2. In Sect. 4.3, we analyze a cluster in equilibrium, e.g., neither expanding nor contracting, to determine if we can find significant expansion or contraction by randomly selecting a subset of cluster members. In the second

part of our analysis, Sect. 4.4, we simulate a cluster based on the cluster properties of Tr 14, let it expand for 1.2 Myr, and determine if we can recover the expansion.

4.2 Stellar cluster model

We simulate stellar clusters using an N-body code that assigns position and velocity values to the particles based on the Plummer density profile and Plummer potential (Plummer, 1911), which are defined as

$$\rho(r) = \frac{3M}{4\pi a^3}\left(1 + \frac{r^2}{a^2}\right)^{-5/2} \tag{4.1}$$

and

$$\Phi(r) = -\frac{GM}{\sqrt{r^2 + a^2}} \tag{4.2}$$

with M as the total cluster mass and a as the Plummer radius, which defines the size of the cluster core. We generate 40 000 particles, which are in virial equilibrium, and denote this dataset "numerical cluster" in the following text.

As our main area of research is the Carina OB1 association, we translated the stellar positions and velocity components into observed projected sky coordinates and proper motions to simulate observational data. We assume a cluster distance of 2.35 kpc, which was determined to be Car OB1's distance in Göppl & Preibisch (2022).

4.3 Virialized clusters

Figure 4.1 shows the stellar positions and proper motion diagrams of the virialized numerical cluster. As the simulated cluster is spherically symmetric, we only show the projection along the x- and y-axes.

In cluster detections, it is only possible to recover a subset of cluster members due to effects such as crowding, extinction, and uncertain astrometry. To mimic this effect for our analysis, we randomly selected between 20 and 400 members from the numerical cluster. These cluster sizes are comparable to those we found for clusters in Car OB1 using *Gaia* DR3 data.

For each simulated cluster, we determined whether it shows signs of contraction or expansion by plotting the position versus its velocity, calculating Pearson's correlation coefficient r_{xv_x}, and then the Student's t-value to determine the significance of the correlation. We rotated the position and velocity coordinates from 0° to 180° to find the angle with the highest significance of expansion or contraction. This is the same method we applied to the Car OB1 clusters in Sect. 3.4.

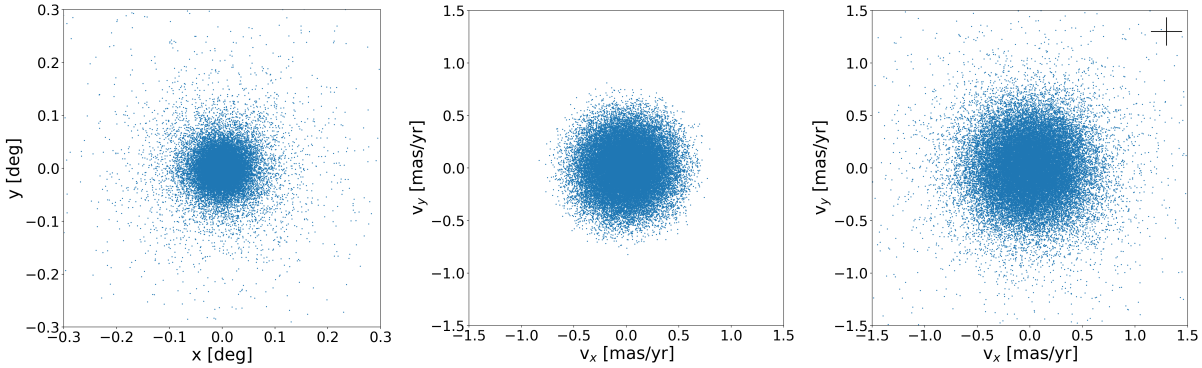

Figure 4.1: Positions (left panel) and proper motions (middle panel) of the particles in the full simulated cluster scaled to an assumed distance of 2.35 kpc. Velocities are rescaled with a velocity unit of 7.7 $\mathrm{km\,s^{-1}}$, to match its velocity dispersion to that of Tr 14. In the right panel, proper motions are shown with added uncertainties. The uncertainties are drawn from the distribution in Fig. 4.2, rescaled, and then added to the proper motions while randomly weighted by their normal distribution. The right plot shows one possible realization. The black cross shows the median uncertainty in proper motion from Gaia DR3 data (as shown in blue in Fig. 4.2).

As a first step, we directly used the proper motions calculated from the velocities of the particles in the numerical cluster, without adding errors. Following this, we added realistic uncertainties to the proper motions of each star and repeated the whole analysis.

Figure 4.2 shows a histogram of the uncertainties of *Gaia* DR3 objects in the Car OB1 region with distances compatible with Car OB1, $\varpi/\sigma_{\varpi} > 2$, and ruwe < 1.4, and a histogram of an alpha distribution with the same sample size that provides a good fit to the distribution of the uncertainties. The shown alpha distribution has a shape parameter of $\alpha = 3.2$, a scale parameter of $\beta = 1$, and is shifted by -0.172. The mode of the distribution is 0.095 $\mathrm{mas\,yr^{-1}}$, which corresponds to 1.06 $\mathrm{km\,s^{-1}}$ at the distance of 2.35 kpc.

We fit the velocity uncertainty distribution with an alpha distribution (Figure 4.2), as it has an extended tail toward larger uncertainty values. For our cluster analysis, we assigned each object a random uncertainty from this distribution. Tr 14, the cluster with the most members recovered in our Car OB1 sample, has a velocity dispersion of 2.31 $\mathrm{km\,s^{-1}}$. We rescaled the numerical cluster's velocity dispersion of 0.3 to Tr 14's dispersion, using a velocity unit of 7.7 $\mathrm{km\,s^{-1}}$, to achieve a realistic velocity dispersion.

We used the Monte Carlo method to account for the velocity uncertainties in the expansion significance analysis for each cluster. For this, we first sampled uncertainties for each star from the approximated alpha distribution, as shown in Fig. 4.2, and translated these values to $\mathrm{km\,s^{-1}}$ at a distance of 2.35 kpc. Assuming that the velocity uncertainty for a star corresponds to the standard deviation in a normal distribution, we randomly weighted the uncertainty for each star, added it to the velocity of the star, and then calculated the correlation coefficient for the cluster. Because each weighting leads to a different realization, we carried this out 1000 times, storing the correlation coefficient

for each realization, and then determined the mean correlation coefficient. From that, we calculated the Student's t-value and the expansion significance of the cluster. We repeated this for angles between 0° and 179° to find the angle with the highest expansion or contraction significance.

An example of the method is shown in Fig. 4.3 for a cluster with 400 members. The plot on the left displays the mean significances of each angle in green. As the Monte Carlo uncertainty determination leads to fluctuations in the significance distribution, seen in green, we apply smoothing to recover the underlying distribution, shown in magenta, and the angle of the highest significance. We then took the maximum of the smoothed significance as the cluster's maximum significance for expansion or contraction. The plot on the right shows the position plotted versus the velocity at the angle of highest significance, here 117°, with the slope of the linear fit in green.

We calculated the highest significance for contraction or expansion 500 times for clusters with sizes of 20, 30, 50, 80, 100, 200, 300, and 400 members and stored the maximum significance for each cluster. Figure 4.5 shows them as a histogram, while Table 4.1 lists the mean maximum significances for each cluster size and the number of clusters whose maximum significance exceeds the threshold of 1, 2, or 3σ.

Cluster size	No uncertainties				With uncertainties			
	$< \sigma >$	$> 1\sigma$	$> 2\sigma$	$> 3\sigma$	$< \sigma >$	$> 1\sigma$	$> 2\sigma$	$> 3\sigma$
20	1.07 ± 0.52	252	23	4	0.74 ± 0.36	105	3	0
30	1.03 ± 0.53	236	24	2	0.69 ± 0.34	71	2	0
50	0.98 ± 0.44	227	10	1	0.64 ± 0.31	67	0	0
80	0.92 ± 0.44	183	10	1	0.61 ± 0.30	55	0	0
100	0.91 ± 0.42	182	9	0	0.61 ± 0.29	50	0	0
200	0.86 ± 0.43	154	7	0	0.57 ± 0.26	30	0	0
300	0.83 ± 0.38	143	2	0	0.54 ± 0.25	24	0	0
400	0.84 ± 0.39	158	2	0	0.52 ± 0.24	20	0	0

Table 4.1: Mean maximum significance of expansion or contraction for 500 clusters per cluster size, and number of simulation runs that yielded maximum significances of $> 1\sigma$, $> 2\sigma$, and $> 3\sigma$.

4.4 Expanding cluster

To analyze an expanding cluster, we model it after the cluster properties of Tr 14, as we find the strongest indication of expansion for that cluster in Car OB1 at a significance of 5.2σ, which can be seen in the first panels of Fig. 3.18 and Fig. 3.19. For our numerical set-up, we assume a total cluster size of 7827 members with a cluster mass of 4492 $M_{\odot}$, based on extrapolation of Tr 14's O-type star population, and a Plummer radius of 1.63 pc. Clusters experience rapid gas expulsion a few Myrs after their formation, resulting in cluster

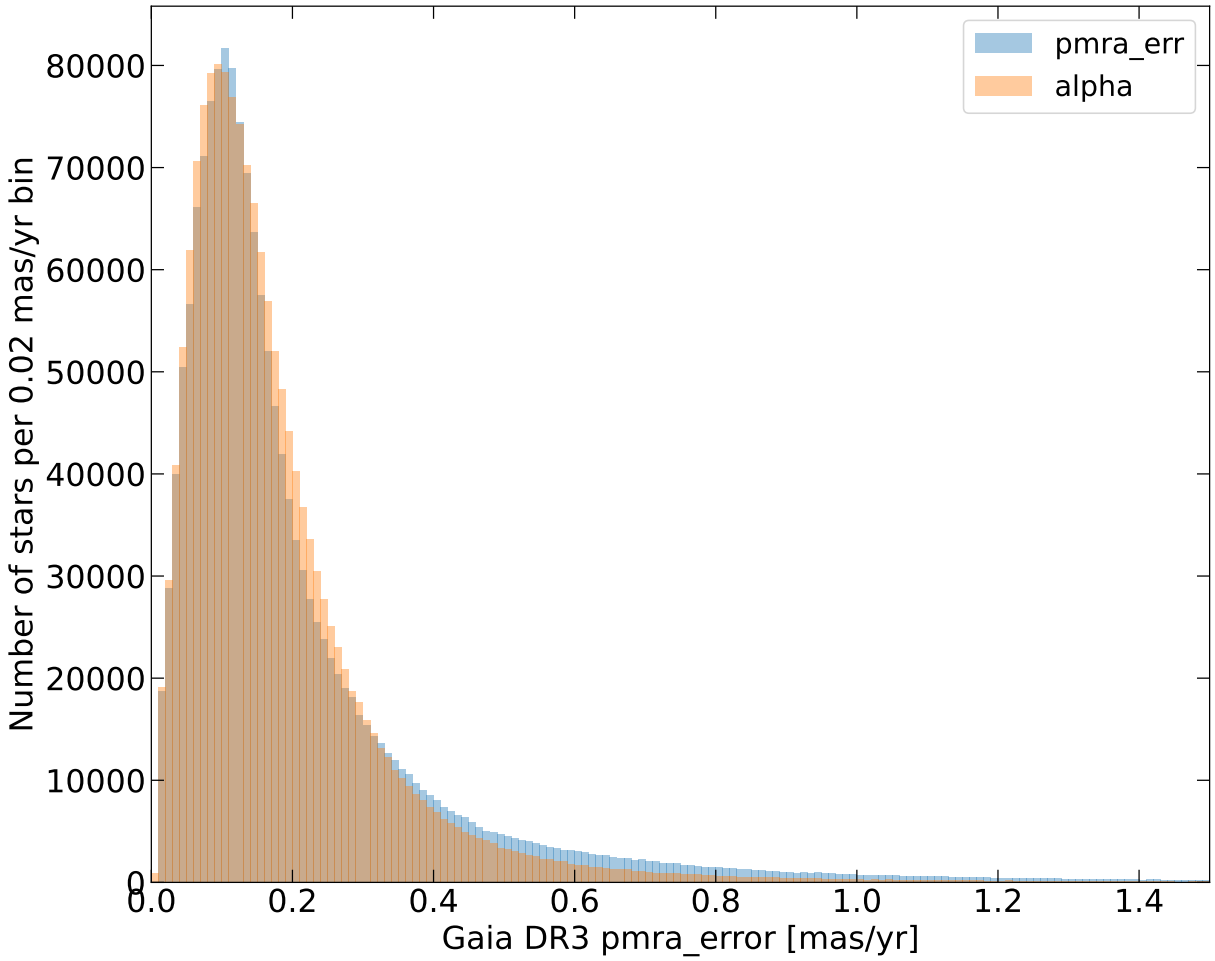

Figure 4.2: Histogram of uncertainties in μ_α^* in the Car OB1 region with distances compatible with Car OB1, $\varpi/\sigma_\varpi > 2$, and ruwe < 1.4 in blue. Approximation with an alpha distribution with a shape parameter of $\alpha = 3.2$, a scale parameter of $\beta = 1$, and shifted by -0.172, shown in orange.

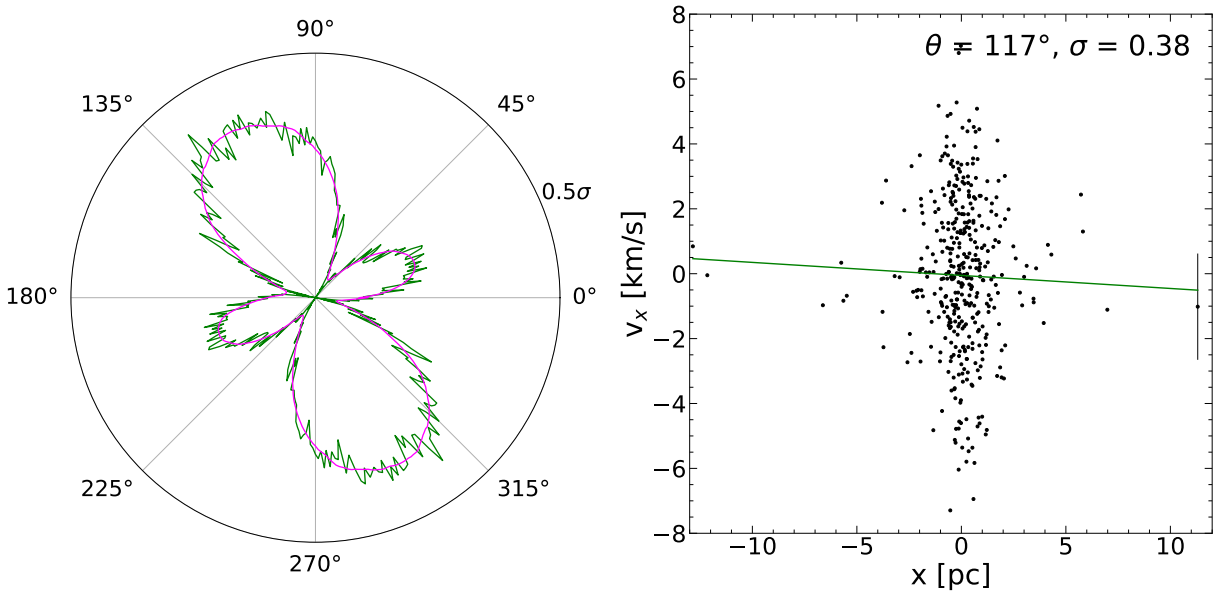

Figure 4.3: Example plots of the analysis for a random cluster with 400 members. The left panel illustrates the significance expansion or contraction depending on the angle, while the right panel displays the position versus velocity plot at the angle with the highest significance.

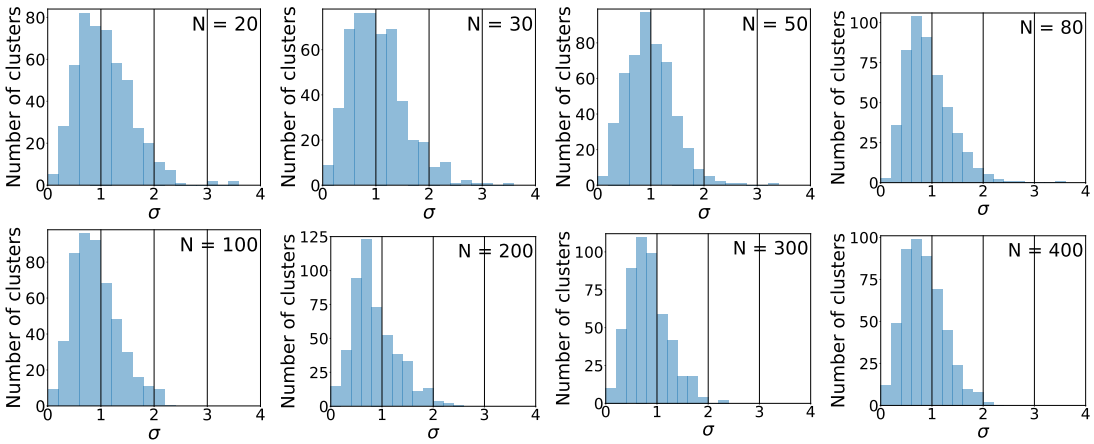

Figure 4.4: Histogram of maximum significances for 500 clusters without taking uncertainties into account per cluster size. The vertical lines highlight the significances of 1, 2, and 3σ.

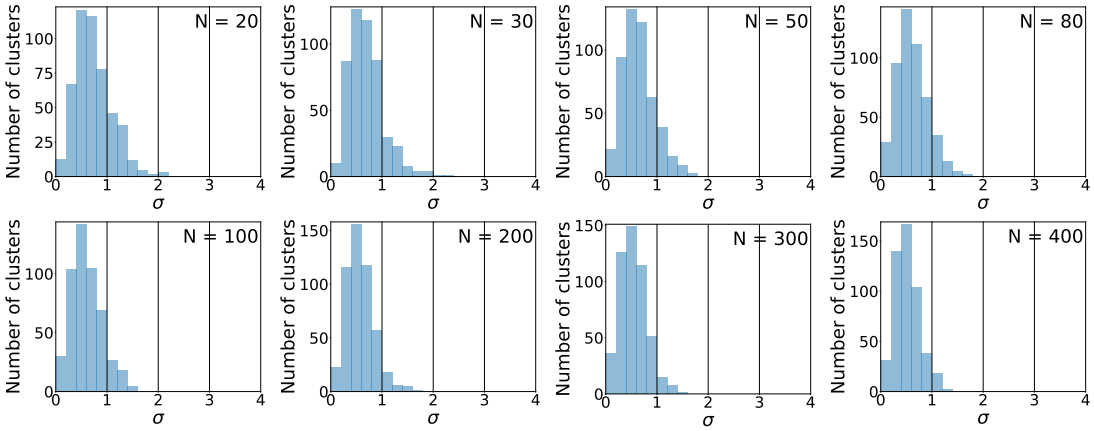

Figure 4.5: Histogram of maximum significances for 500 clusters with uncertainties accounted for per cluster size. The vertical lines highlight the significances of 1, 2, and 3σ.

expansion (Krause et al., 2020). To simulate this, we first set up the positions and proper motions of the stars using a higher cluster mass, which we then reduce to mimic the effect of the mass loss through a reduced potential, i.e., gas expulsion, and let the cluster evolve for 1.2 Myr in accordance with the kinematic age of Tr 14. Figure 4.6 shows the positions and proper motions of stars in the simulated cluster Tr 14 at simulation times of 0 Myr and 1.2 Myr. As the simulation begins with a fully formed cluster, the elapsed time is not equal to the cluster age, but the time since the cluster has been expanding.

The numerical cluster has a velocity dispersion of 0.3 in our set-up, which we multiply by a velocity unit of 7.7 $\mathrm{km\,s^{-1}}$ to obtain the observed velocity dispersion of 2.31 $\mathrm{km\,s^{-1}}$ in Tr 14. As the cluster is set to expand, we repeat our expansion analysis to determine if we can recover the expansion and at what significance. We repeat our kinematic analysis taking velocity uncertainties into account, as described in Sect. 4.3.

Figure 4.7 shows the maximum significances we find if we randomly draw 434 members, i.e., the number of Tr 14 members used for kinematic analysis in Göppl & Preibisch (2025), from the complete sample and test for expansion. We carry out the analysis 500 times at expansion times of 0 and 1.2 Myr. We find only expansion at low significances at 0 Myr, which is to be expected as the cluster is just starting to expand. However, we determine indications of expansion at much higher significances ($> 4\sigma$) already at 1.2 Myr for all realizations. Beyond that age, most of the realizations ($\approx 90\%$) have very small p-values of $< 5 \times 10^{-17} \cong 8\sigma$ even when taking uncertainties into account.

4.5 Conclusions

We have simulated two clusters, one virialized and one expanding, to explore how kinematical analyses of observed clusters are done on a subset of members and how this affects the results. For the cluster in virial equilibrium, we find overall only small chances of false positives with a significance of $> 2\sigma$, with the highest chance at 5.4% at cluster sizes of

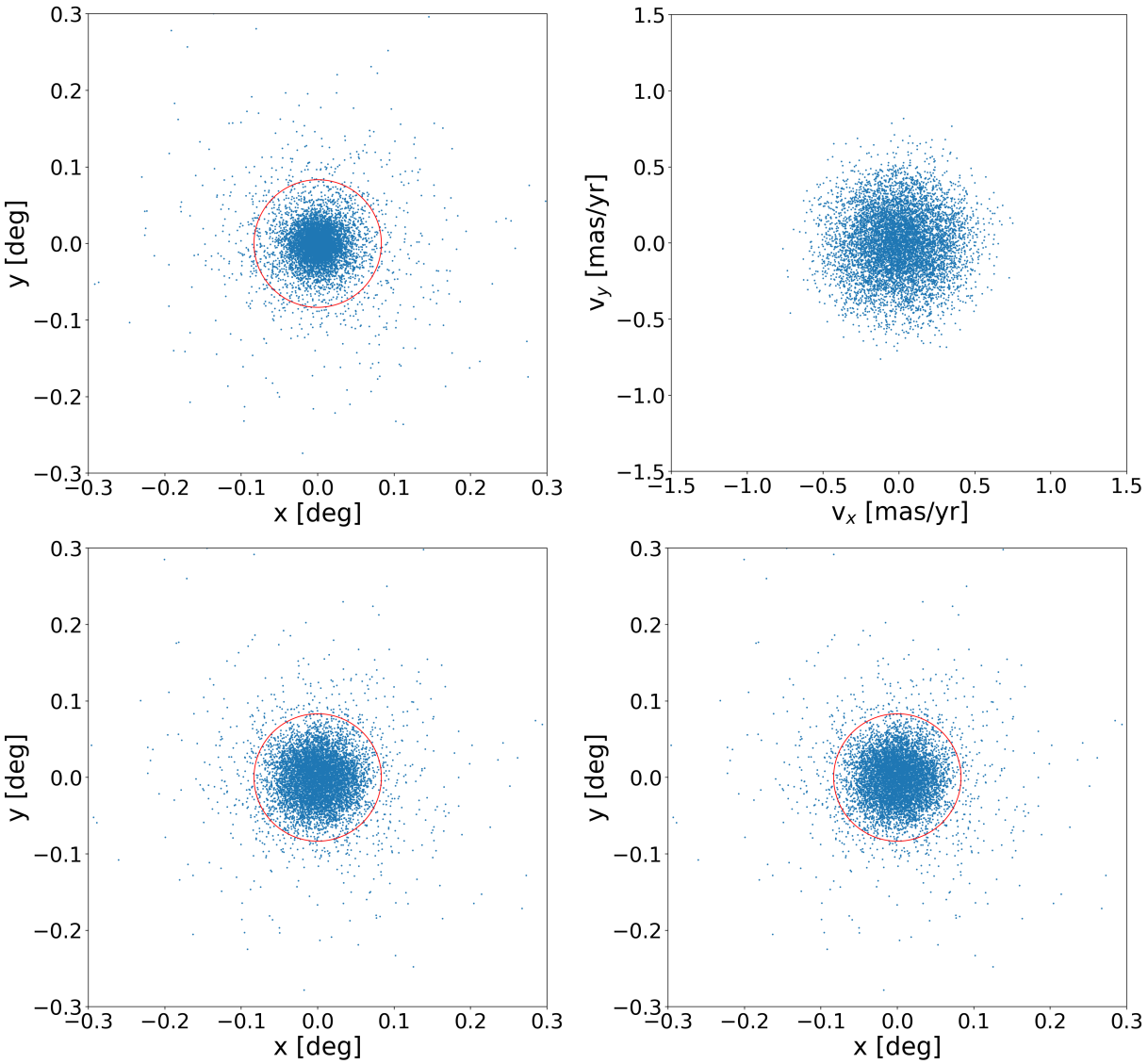

Figure 4.6: Positions and velocities for the simulated Tr 14 cluster, scaled to a distance of 2.35 kpc and a velocity dispersion of 2.31 $\mathrm{km\,s^{-1}}$. The cluster is shown at an elapsed simulation time of 0 Myr (upper panels) and 1.2 Myr (lower panels). The red circle shows the full extent of the currently observed cluster Tr 14.

20 members without taking uncertainties into account. We find that the amount of false positive expansion or contraction results decreases with increasing cluster member size, regardless of whether velocity uncertainties were taken into account or not. While the number of false positives decreases with increased cluster member size from 20 to 200, it plateaus for cluster member sizes of 200 or more, showing only small differences. When we include velocity uncertainties in our analysis, the rate of false positive expansion or contraction results is lower at all cluster sizes.

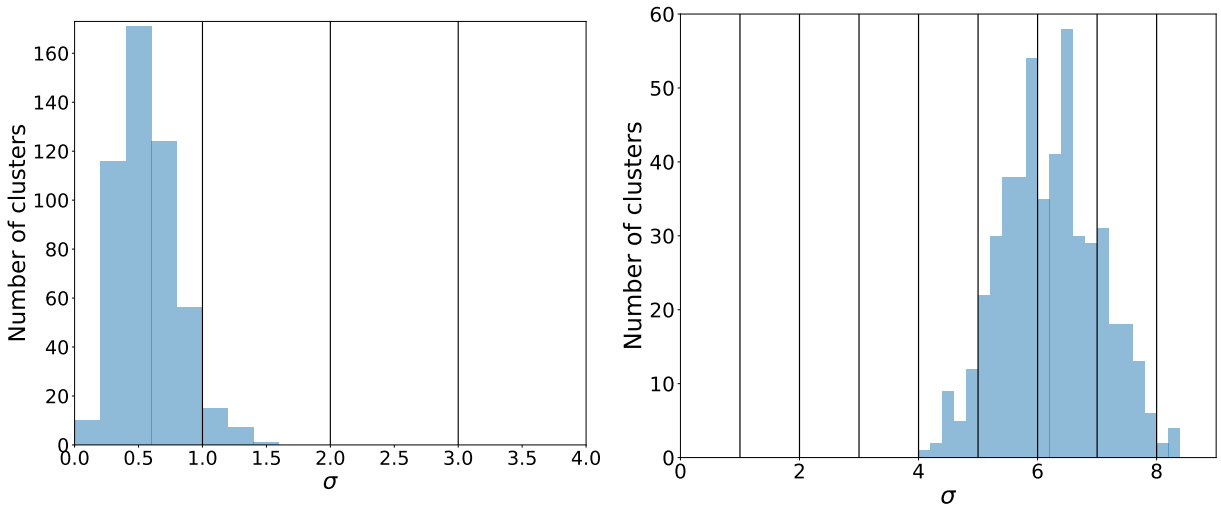

Figure 4.7: Histogram of maximum significances for 500 clusters with sizes of 434 members with uncertainties at simulation times of 0 and 1.2 Myr. The lines show the significances of 1–8σ.

When simulating an expanding cluster, we find that we can recover the underlying expansion with high significance, which increases the longer the expansion has been going on. These results strengthen the result that the expansion observed for Tr 14 is likely due to a real underlying expansion, considering the cluster size and the high determined significance of 5.2σ.

In future simulations, we plan to take a closer look at the influence of the expansion velocity and time on the results of the kinematic analysis. While the speed of the velocity should have no influence on the results, if velocity uncertainties are neglected, the ratio between velocity uncertainties and velocity dispersion of the cluster is likely a deciding factor in whether expansion or contraction can be recovered when uncertainties are taken into account.

CHAPTER 5

SPATIO-TEMPORAL EVOLUTION OF STAR FORMATION IN THE CAR OB1 ASSOCIATION

C. Göppl and T. Preibisch, submitted to *Astronomy & Astrophysics* on 20.11.25 and currently in the review process

5.1 Introduction

OB associations are the stellar nurseries where most of the high-mass stars in our Galaxy are born (see, e.g., Wright et al., 2023, for a recent review). Due to their large spatial extent (several tens of parsecs) and low stellar density, associations are expected to expand and disperse over a timescale of a few tens of megayears. Most OB associations show substructure in the form of stellar groups and clusters of various ages; many OB associations also still contain molecular clouds with ongoing star formation. This is seen, e.g., in the Scorpius-Centaurus (Sco-Cen) association (Damiani et al., 2019; Ratzenböck et al., 2023a,b; Žerjal et al., 2023) and in Orion OB1 (Zari et al., 2019; Chen et al., 2020; Hunt & Reffert, 2023). Indications for sequential, presumably triggered formation of subgroups or clusters in OB associations have been found already decades ago in several nearby OB associations (see, e.g., Elmegreen & Lada, 1977; de Geus, 1992; Preibisch & Zinnecker, 1999; Briceño et al., 2007).

In the era before *Gaia*, model scenarios for triggered sequential star formation in OB associations were necessarily rather simple, usually employing only a few steps of triggering in a linear sequence of large star clusters/groups. In the last few years, the availability of precise astrometric data from *Gaia* allowed a much more reliable definition of clusters and associations as co-moving groups of stars. For nearby OB associations, the precise *Gaia* proper motions and parallaxes made it possible to draw a detailed picture of their

spatio-temporal evolution. In some cases, these studies revealed a clear systematic spatial progression of star formation events, creating chains of clusters with decreasing ages (e.g., Ratzenböck et al., 2023b; Posch et al., 2023, 2025; Miret-Roig et al., 2025; Großschedl et al., 2025; Hutschenreuter et al., 2025, for the case of the Sco-Cen OB association), that connect the oldest cluster with the very young clusters, which are sometimes still sites of ongoing star formation. Similar, although often less clear indications of sequential star formation, have also been found in several other OB associations, such as Cepheus-Hercules (Kerr et al., 2024), the Circinus Complex (Kerr et al., 2025), and the Vela OB2 Complex (Cantat-Gaudin et al., 2019; Pang et al., 2021). Sequential star formation is suggested to be triggered by feedback from massive stars, initiating the formation of the next generation of clusters, for example, via their (ionizing) radiation, winds, or supernova shocks.

A scenario for the recent formation history of the clusters Tr 14, 15, and 16 and the South Pillars clouds in the central Carina Nebula has been presented by Povich et al. (2019). In the chapter presented here, we extend the star formation scenario in two ways: firstly, we consider the full spatial extent of the Car OB1 association, including also the northern parts with the clusters NGC 3324, NGC 3293, and IC 2581. Secondly, our scenario covers the full history of the association, which started ≈ 13 Myr ago with the formation of the oldest cluster, NGC 3293.

As the first step of the analysis in this chapter, we build on our previous results from Göppl & Preibisch (2025, GP25, hereafter) to characterize the stellar populations of the clusters in Car OB1 and estimate the number of supernova explosions that have happened until today (Sect. 5.2). In Sect. 5.3, we determine the 3D structure and kinematics of the association, and perform a traceback analysis of the cluster positions over the formation history of Car OB1. In Sect. 5.4, we construct a model for the global formation history of the association, and we summarize our conclusions in Sect. 5.5.

5.2 Properties of the individual clusters in Car OB1

The data for this study are based on the results from GP25: we consider the eight most massive clusters in Car OB1, selected by the condition that each cluster has at least two high-mass ($M_* \geq 18\,M_\odot$) stars today. Our census of the high-mass stellar population of each cluster is based on the catalog of high-mass stars in Car OB1 from GP25. For the estimates of the full stellar population of the clusters, we also use the catalog of X-ray emitting young stars from the *Chandra Carina Complex Project* (CCCP, Townsley et al., 2011b), as well as the source catalogs resulting from the *Chandra* X-ray observations of NGC 3324 (Preibisch et al., 2014a) and NGC 3293 (Preibisch et al., 2017).

As a first step of our analysis, we derive best estimates of the cluster ages, the present and the initial population of high-mass stars in each cluster, and the total initial stellar population size for each cluster; these data are listed in Table 5.1. Comments on individual clusters are given in Sect. 5.2.5.

For the conversion of (main-sequence) spectral type to stellar mass, we used the most

recent version[1] of the calibration table from Pecaut & Mamajek (2013), according to which all O-type main-sequence stars have a mass of $M_* \geq 18\,M_\odot$. In the rest of the paper, the term "high-mass star" means a star with an initial main-sequence stellar mass of $\geq 18\,M_\odot$.

5.2.1 Cluster Ages

Cluster ages are taken from our analysis in GP25 and the literature. For some of the clusters, a range of different ages is reported in the literature. In addition to the notorious difficulties in the determination of stellar cluster ages (see, e.g., Preibisch, 2012; Herczeg & Hillenbrand, 2015), the complex spatial configuration of the stellar populations in the Carina Nebula Complex (CNC) adds another uncertainty factor. As described in GP25, a substantial fraction of the young stars in the Carina complex constitutes a non-clustered, widely distributed population that had already been seen in the previous X-ray and infrared surveys (Feigelson et al., 2011; Zeidler et al., 2016). The ages of the stars in this distributed population show a broad distribution between ≈ 3 Myr and ≈ 10 Myr (Povich et al., 2019; Preibisch et al., 2011b). Stars from this distributed population will therefore contaminate the samples of cluster stars, and (for the younger clusters) produce a systematic bias in the cluster age estimates towards older values, if a significant number of stars from the distributed population is included in the chosen cluster area. This effect is well demonstrated in the study of Tr 14 by Itrich et al. (2024) (see their Fig. 12 and I.1): for the stars in the cluster core, the age distribution is narrowly confined around 1 Myr, but when stars in the outskirts of the cluster area are included in the sample, a much broader age distribution and an older mean age are found, due to the increased contamination by stars of the distributed population. We therefore prefer age estimates that are based on the cores of the cluster, in order to minimize the contamination by stars from the distributed population.

5.2.2 High-mass stellar populations and expected number of supernovae

Information about the number of high-mass stars in a cluster is essential for quantifying the level of feedback the cluster exerts on its surroundings. For the young ($\lesssim 4$ Myr old) clusters, where even the most massive stars are still present, one can simply count the number of observed O-type, WR-stars, and supergiants in the respective cluster area.

For the older clusters ($\gtrsim 5$ Myr), one also has to take into account that the most massive stars may have already exploded as supernovae. While there is no direct observational evidence for recent supernova explosions in Car OB1 (e.g., in the form of a prominent supernova remnant), the substantial numbers of early B-type stars in the older (≥ 5 Myr) clusters NGC 3293, IC 2581, and Tr 15 strongly suggest that some O-type stars must have been initially present in these clusters. The X-ray detection of at least one neutron star candidate in the Carina Nebula (Hamaguchi et al., 2009) provides direct support

[1] `https://www.pas.rochester.edu/~emamajek/EEM_dwarf_UBVIJHK_colors_Teff.txt`

for this scenario. Further indirect evidence comes from X-ray observations of the strong diffuse high-energy emission in the area around the Carina Nebula, which clearly show that the CNC superbubble is filled with large amounts of very hot, X-ray emitting plasma (Townsley et al., 2011a; Sasaki et al., 2024). Although a large fraction of this plasma is expected to be generated by the winds of the numerous massive stars, it is considered quite likely that supernova explosions have contributed to the observed emission. The fact that no prominent supernova remnant is seen in Car OB1 does not contradict the expectation of several supernova explosions over the last ≈ 10 Myr, because the lifetime of a supernova remnant is rather short, $\leq 10^5 - 10^6$ years (see, e.g., Braun et al., 1989; Bamba & Williams, 2022). The lack of prominent supernova signs in Car OB1 thus implies that the last supernova explosions must have happened more than a few 10^5 years ago.

For the three clusters older than 5 Myr, we estimated the number of supernovae that are expected to have already happened by using an IMF extrapolation based on the number of present OB stars, as described in more detail in Sect. 5.2.5.

5.2.3 Timing of supernova explosions in Car OB1

In order to construct a formation scenario for Car OB1 that takes the effects of supernovae into account, we also need information about the times at which the first supernova explosion in each cluster occurred, since this dominates the dynamical evolution of the expanding bubble. As the most massive star in a cluster explodes first, we can estimate the time of the first supernova if we know the mass of the initially most massive star in the cluster. We estimate this maximum stellar mass in two ways: (i) by using the observed relation between the total mass of a cluster and the mass of the most massive star as given in Weidner et al. (2013), and (ii) by extrapolating the IMF (Kroupa, 2001) of the cluster based on the cluster mass as listed in Table 5.1 and calculating the mass bin $[M_{*,\max}, 100]\ M_\odot$ in which we would only expect one star. From this estimate of the highest star mass, we can then determine its main-sequence lifetime using the relation from Parravano et al. (2003). The results of this analysis are given in Table 5.3. For NGC 3293, the first supernova should have occurred ≈ 9 Myr ago. The first supernova in Tr 15 happened ≈ 2 Myr ago. In total, there were ≈ 15 supernovae in Car OB1 during the last ≈ 9 Myr. Since there is no evidence for a recent supernova in this area (see Townsley et al., 2011a), the last of these supernovae must have happened $\gtrsim 1$ Myr ago.

5.2.4 Estimates of the total cluster populations

We use two different approaches to estimate the total stellar population of each cluster. The first approach is an IMF extrapolation based on the observed population of O-type (or B-type) stars in each cluster, assuming a Kroupa IMF (Kroupa, 2001) and extrapolating down to $0.08\,\mathrm{M}_\odot$. The upper mass limit was chosen for each cluster individually based on the most massive star.

For the young ($\lesssim 4$ Myr old) clusters, where all (i.e., even the most massive) stars are still present, one can simply extrapolate from the number of observed O- and/or B-type

stars in the cluster. For the older clusters ($\gtrsim 5$ Myr), one also has to take into account that the most massive stars have already evolved into supergiants or exploded as supernovae; an IMF extrapolation based on the currently present OB stars would thus underestimate the stellar population. In these cases, one also has to extrapolate the observed population of B-type stars upwards in order to estimate how many high-mass stars were initially present. To achieve this, we first calculate the current cluster population and then extrapolate upwards from the most massive still-existing star in the cluster. We quantify the uncertainty by assuming a Poisson distribution.

In the second approach, we estimate from the observed number of X-ray detected stars in each cluster, employing the number ratio of X-ray sources to total stellar population and the stellar population sizes derived in Feigelson et al. (2011) as they extrapolate a stellar population of 104 000 stars from a X-ray population of 10 728. For clusters that do not have a counterpart in Feigelson et al. (2011), e.g., Collinder 228, we choose all X-ray detected stars inside the cluster radius and extrapolate from that value. We also use this method for Tr 16, as our cluster boundary and the one used in Feigelson et al. (2011) deviate strongly from each other.

For most clusters, the two different estimates of the total stellar population agree within a factor of about two. The larger differences seen in some cases are related to the uncertainties of both methods, in particular to stochastic effects in the numbers of O-type stars, and illustrate the uncertainties of these extrapolations. Therefore, the star numbers should be considered estimates rather than precise values.

5.2.5 Notes on the individual clusters

Tr 16 is the largest cluster in Car OB1 and consists of several sub-clusters (see Feigelson et al., 2011; Göppl & Preibisch, 2025). Including the O-type stars in the strongly obscured subgroup Tr16-SE (Preibisch et al., 2021), it contains 33 O-type/WR stars, the Luminous Blue Variable η Car, and one blue supergiant. We adopt a mass of $100\,M_\odot$ for η Car (Strawn et al., 2023) and set this as our upper mass limit for the IMF extrapolation. This results in a total cluster population of 17 272 stars. The age of Tr 16 is $\approx 3-4$ Myr (Preibisch et al., 2011b; Povich et al., 2019).

Tr 14 hosts 15 O-type stars and three B supergiants. At the cluster age of ≈ 1 Myr (Itrich et al., 2024; Kang et al., 2025), all high-mass stars should still be present. The most massive star is the spectroscopic binary HD 93129 A with spectral type O2 If*/WN5 + O3.5 III and an initial mass of $100\,M_\odot$ (Gruner et al., 2019) for the primary star. The IMF extrapolation results in an estimate of a total population of 8 883 stars.

Tr 15 contains three O-type stars (HD 93249: O9 III + B1.5 III, TYC 8626-02506-1: O9 V(n), and Tr15-20: O9 V:) and 20 stars with spectral types between B0 and B2.5. The IMF extrapolation leads to an expected initial number of 6.2 ± 2.5 high-mass stars. Subtracting the three O9 stars still present today, and the supergiant HDE 303310 (M3 Iab,

Table 5.1: Stellar population properties of the eight largest clusters in Car OB1. We list the currently observed number of high-mass ($M \geq 18\ M_\odot$) stars, our estimates for the expected number $\mathcal{E}[N_{\rm SN}]$ of supernovae that happened in each cluster, the time ($t_{\rm first\ SN}$) at which the first supernova has presumably happened, and the estimated total stellar populations $\mathcal{E}[N_{\rm tot}]$ based on the number of X-ray detected stars and known O/B stars, as well as an estimate of the total stellar mass of each cluster.

Cluster	Radius (pc)	Age (Myr)	$N_{\geq 18\ M_\odot}$ today	$\mathcal{E}[N_{\rm SN}]$	$t_{\rm first\ SN}$ (Myr)	$\mathcal{E}[N_{\geq 18\ M_\odot}]$ initial	$\mathcal{E}[N_{\rm tot}]$ X-ray	$\mathcal{E}[N_{\rm tot}]$ O/B	$\mathcal{E}[M_{\rm tot}]$ $M_\odot$
Tr 16	5.1	$\approx 3-4$	35	0	–	35	11 846	17 272	≈ 8350
Tr 14	3.4	≈ 1	18	0	–	18	14 037	8883	≈ 6580
Tr 15	3.4	≈ 6	4	2.2 ± 2.5	≈ -2	6	4663	3056	≈ 2210
Cr 228	1.7	≈ 3.5	5	0	–	5	611	2678	≈ 940
Bo 11	2.3	≈ 4	4	0	–	4	1328	2381	≈ 1060
NGC 3324	2.1	≈ 2	3	0	–	3	1648	2283	≈ 1130
NGC 3293	3.9	≈ 13	3	10.9 ± 3.7	≈ -9	10	5420	5168	≈ 3040
IC 2581	3.5	≈ 12	2	2.3 ± 2.1	≈ -7	3	–	1587	≈ 910
Full Car OB1 (including the stars of the distributed population)			≥ 135	15 ± 5		$\gtrsim 145$		$\gtrsim 75\,000$	

%endtable

Berlanas et al. (2023)), this leads to an expected number of 2.2 ± 2.5 supernovae that have already happened. The IMF extrapolation also leads to a total cluster population of 3 056 stars. Recent age estimates for Tr 15 are in the range $\approx 5-8$ Myr (Preibisch et al., 2011b; Povich et al., 2019; Ansín et al., 2023; Berlanas et al., 2025), and thus we assume an age of ≈ 6 Myr.

Cr 228 is located in the Southern Pillars region, and contains four O-type stars with spectral types from O7 V((f))z to O9.7 IV and one WR star (HD 93131) with spectral type WN6ha-w, for which we adopt a mass of 68 $M_\odot$ (Hamann et al., 2019), which we use as an upper mass limit. This results in an extrapolated cluster population of 2 678 members. Kharchenko et al. (2013) and Delgado et al. (2011) estimated ages of 4.8–5 Myr for the cluster, but these values are probably too high because of sample contamination by older stars from the distributed population. As the main-sequence lifetime of a 68 $M_\odot$ star is 3.3 Myr (Parravano et al., 2003), we assume Cr 228 to have an age of ≈ 3.5 Myr.

Bo 11 is also located in the Southern Pillars region and hosts four O-type stars whose spectral types range from O5 Ifvar to O9.7 IV. According to Martins et al. (2005), an O5 I star has a mass of 50.7 $M_\odot$. We adopt this value as the upper mass limit for the cluster and extrapolate a cluster population of 2 381 members. Photometric age estimates for the cluster yielded values of ≈ 6 Myr (Dias et al., 2002) and ≈ 5 Myr (Preibisch et al., 2011b). We can approximate the maximum age of Bo 11 with the lifetime of its earliest star, HD 93632, with spectral type O5 Ifvar. As supergiants have high mass-loss rates, we can assume the star's current mass of 50.7 $M_\odot$ as the star's minimum initial mass on the Main Sequence for a maximum lifetime. This leads to a main-sequence lifetime of ≈ 4 Myr based on the calibration from Parravano et al. (2003), and we use this value as the age of Bo 11.

NGC 3324 is located north of the Carina Nebula and harbors three O-type stars, HD 92 206 A and B (both of spectral type O6 V) and CD −57 3376 (spectral type O9/B0), which create the H II region Gum 31. Assuming 35 $M_\odot$ for an O6 V star as an upper mass limit, we estimate a total cluster population of 2 283 members. The estimations of NGC 3324's age in literature range from $\approx 1-2$ Myr (Preibisch et al., 2014a; Kharchenko et al., 2013) over 6.4 Myr (Dias et al., 2021) and up to 11–12 Myr (Cantat-Gaudin et al., 2020; Tarricq et al., 2021). We note that these latter high values are inconsistent with the presence of O6 main-sequence stars, which have a main-sequence lifetime of ≈ 5 Myr based on the calibration of Parravano et al. (2003). These inconsistent age estimates are probably caused by a bias due to the choice of a (too) large radius for selecting cluster members: the studies with the older age estimates used selection areas of $300-400$ square arcminutes, which then include a considerable number of stars from the older distributed stellar population, and are at least ten times as large as our selection area for NGC 3324 (28.3 square arcminutes). Based on these considerations, we assume the age of NGC 3324 to be ≈ 2 Myr.

NGC 3293 is located at the north-western edge of the cloud complex and contains 41 stars with spectral types between B0.5 and B3, leading to an expected initial population of 13.9 ± 3.7 with earlier spectral types than B0.5, out of which 10.5 ± 3.2 have masses higher than $18\,M_\odot$. As there are three supergiants (HD 91969: B0 Iab, HD 91943: B0.7 Ib, and CP −57 3502: M1.5 Iab-Ib), the number of expected supernovae is 10.9 ± 3.7. The IMF extrapolation yields a total cluster population of 5 168 members. In GP25, we estimated the age of NGC 3293 to be $\approx 10 - 15$ Myr based on *Gaia* photometry. As the earliest main-sequence spectral type in NGC 3293 is B0.5-1.5 V, with a mass of $14.8\,M_\odot$ (Pecaut & Mamajek, 2013), this leads to a main-sequence lifetime of ≈ 13.4 Myr (Parravano et al., 2003). We therefore assume an age of ≈ 13 Myr for NGC 3293. This implies that NGC 3293 is the oldest of the massive clusters in Car OB1, and that its formation marks the origin of the association.

IC 2581 is a young cluster located at the extreme north-western periphery of Car OB1. It appears rather separated from the other parts of Car OB1, but was defined as a subgroup of Car OB1 by Mel'Nik & Efremov (1995). Its distance is somewhat larger than that of the other clusters, but still consistent with membership in Car OB1. It contains eight stars between spectral types B0.5 and B2, which leads to an expected number of 4.3 ± 2.1 stars with masses higher than a B0.5 star, and 3.2 ± 1.8 stars with masses higher than $18\,M_\odot$. As the cluster hosts two supergiants (V399 Car: A9/F0 Ia/ab and HD 90706: B2.5Ia; Turner, 1978), the expected number of supernovae is thus 2.3 ± 2.1 and the IMF extrapolated cluster population is 1 587. In GP25, we determined the age of the cluster to be ≈ 12 Myr.

5.3 Spatio-temporal structure of Car OB1

The basis for our investigation of the 3D-structure and kinematics of the clusters are the mean values for the positions, distances, proper motions, and radial velocities as summarized in Table 5.2. We calculate these values using the stars from the Car OB1 high-mass star catalog and the Car OB1 cluster member catalog (GP25) inside each cluster radius.

5.3.1 Large-scale cloud structure and cluster ages

Figure 5.1 shows the positions and extent of the clusters as circles, color-coded according to their ages, overlaid on the *Herschel* 160 μm map, which traces the distribution of cool gas in the association. The dense clouds are largely concentrated in the central and southern part of the Carina Nebula, and around NGC 3324, whereas no dense clouds are found around or to the west of NGC 3293. There is a large-scale trend of decreasing ages from NGC 3293 in the north-west, towards the younger clusters in the central Carina Nebula, and further on to the still ongoing star formation in the Southern Pillars.

This spatial anti-correlation between the ages of the star clusters and the presence of dense cloud material in their surroundings supports the idea that the feedback from the

Table 5.2: Maximum Likelihood estimates for the mean positions, distance, proper-motion velocities in RA and Dec direction, and median values for the radial velocity of each cluster. The listed uncertainties are the uncertainty of the mean value. The last two columns list the number of stars for which proper motions and radial velocities are available. ¶: The radial velocity of NGC 3324 is not well defined, since measurements are available for only one of the O stars (HD 92206 A), and two much fainter stars (which have very different radial velocities). We therefore list here the radial velocity for HD 92206 A and do not attempt to calculate an uncertainty.

Cluster	RA (h:mm:ss)	DEC (d:mm:ss)	Distance (pc)	$\langle v_{\rm RA} \rangle$	$\langle v_{\rm DEC} \rangle$ (km s^{-1})	$\langle v_{\rm rad} \rangle$	$N_{\rm pm}$	$N_{\rm rad}$
Tr 16	10:45:01.87	−59:44:28.5	2320 ± 8	-76.20 ± 0.02	28.89 ± 0.02	-7.18 ± 1.04	209	120
Tr 14	10:44:07.14	−59:33:13.1	2354 ± 7	-73.13 ± 0.02	23.69 ± 0.02	-7.47 ± 1.09	476	111
Tr 15	10:44:40.69	−59:23:03.7	2369 ± 7	-69.37 ± 0.02	23.35 ± 0.02	-2.72 ± 1.14	266	35
Cr 228	10:43:57.87	−60:05:45.6	2333 ± 20	-73.62 ± 0.05	20.96 ± 0.05	-2.07 ± 3.22	42	9
Bo 11	10:47:04.03	−60:05:36.1	2343 ± 19	-71.69 ± 0.05	23.14 ± 0.05	-4.25 ± 4.31	51	5
NGC 3324	10:37:13.69	−58:36:52.2	2388 ± 16	-80.43 ± 0.04	32.15 ± 0.04	-12.79 ¶	90	3
NGC 3293	10:35:47.78	−58:14:32.9	2325 ± 7	-84.12 ± 0.02	37.36 ± 0.02	-15.05 ± 0.60	363	159
IC 2581	10:27:19.59	−57:36:23.1	2438 ± 11	-83.92 ± 0.03	42.05 ± 0.03	2.85 ± 3.22	125	5

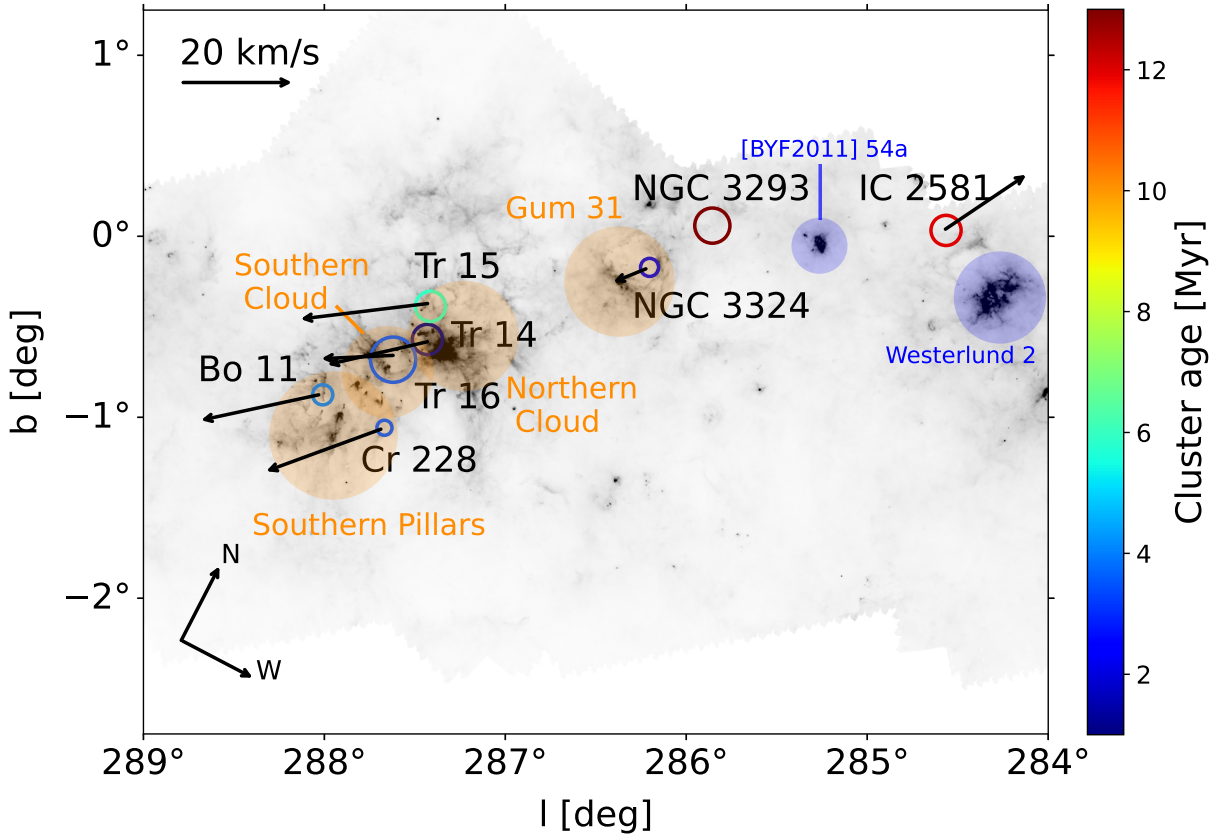

Figure 5.1: Clusters in Car OB1 represented as circles shown with their age on the *Herschel* 160 μm map (from `https://www.cosmos.esa.int/web/herschel/pacs-jscanam-mosaics-hpdp`; see Graciá-Carpio et al., 2017) displayed in inverted grayscale. The cloud complexes of the "Southern Pillars" and the "Northern Cloud", as well as the clouds at the edges of the Gum 31 bubble around NGC 3324, are marked. We also marked the unrelated background cloud complexes BYF2011 54a ($D \approx 5.3$ kpc) and Westerlund 2 ($D \approx 4 - 6$ kpc) in blue. The arrows show the relative 3D velocity of the clusters with respect to NGC 3293.

numerous massive stars in NGC 3293, including presumably 11 supernova explosions, has completely dispersed the original clouds in the north-western part of the association over the last 13 Myr.

5.3.2 3D configuration of the Car OB1 clusters

The 3D configuration of the eight clusters is illustrated in Fig. 5.2. The total spatial extent of the association as seen in projection on the sky, from Bo 11 to IC 2581, is $\simeq 160$ pc (from Bo 11 to NGC 3293 $\simeq 120$ pc). A similarly large range is seen in the distances of the individual clusters, which differ by up to $\simeq 120$ pc.

The distances of the three prominent clusters Tr 14, 15, and 16 in the central Carina

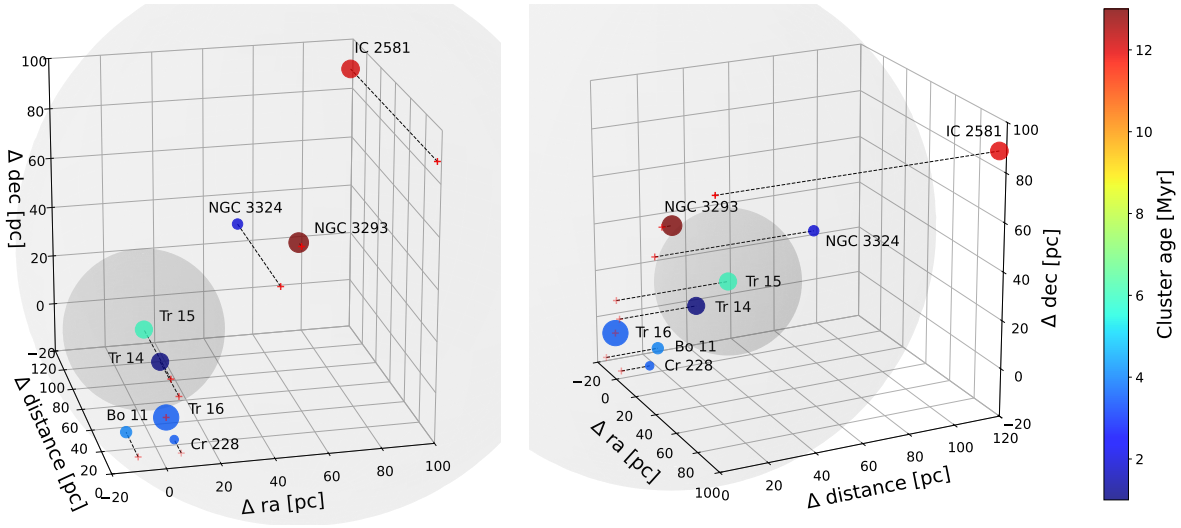

Figure 5.2: Two representations of the cluster position (spheres) in 3-dimensional space, seen approximately from the front (left) and a side-view (right). The red crosses show the projected cluster position on the celestial plane. The radius of the spheres is the cluster radius as listed in Table 5.1, and the clusters are color-coded according to their ages. The gray spheres around NGC 3293 and Tr 15 represent the approximate volumes that supernova-driven bubbles originating in these clusters may have influenced over their lifetime (radii of 100 pc and 30 pc, respectively).

Nebula (which appear to be in close proximity on the sky) vary[2] by up to ≈ 50 pc. Tr 14 and 15 are further away than Tr 16. NGC 3293 is found to be at basically the same distance as Tr 16, while NGC 3324 and IC 2581 are 68 pc and 118 pc more distant (i.e., on the "rear-side" of the association).

5.3.3 Kinematics of the Clusters

Gaia DR3 provides accurate proper motions for the stars in our samples. Since *Gaia* DR3 radial velocities are only available for 23% of the stars in our sample, we complement them with radial velocities from the Gaia-ESO survey (GES) (Gilmore et al., 2012; Hourihane et al., 2023), as well as further studies (Kiminki & Smith, 2018; Hanes et al., 2018; Lloyd Evans, 1969; de Bruijne & Eilers, 2012; Reed, 2005). We exclude radial velocities that are higher than $100\,\mathrm{km\,s^{-1}}$ or lower than $-100\,\mathrm{km\,s^{-1}}$, since such values may suggest motions in binary systems, or run-away stars, i.e., are probably not representative of the cluster motion. Figure 5.7 shows the proper motion and radial velocity values of the individual stars in the different clusters. The mean values of the velocity components for each cluster are summarized in Table 5.2.

[2]Similar differences in the distances were determined by Maíz Apellániz et al. (2025), who derived values of at 2363^{+61}_{-58} pc and 2354^{+61}_{-58} pc for Tr 14 and 15, and for Tr 16 split into east and west at 2311^{+58}_{-56} pc and 2305^{+64}_{-51} pc.

Figure 5.1 shows the direction the clusters are moving with respect to NGC 3293. It can be seen that all clusters appear to move away from NGC 3293 and that the relative velocity increases with distance from NGC 3293 up to values of $\approx 25\,\mathrm{km\,s^{-1}}$.

5.3.4 Relation between the clusters and the surrounding clouds

In order to investigate the physical relation between the star clusters and the surrounding clouds, we compare the median values of the radial velocities of the stars in each cluster to the radial velocities of the molecular and atomic gas at and near the positions of the clusters, as described in detail in Section 5.A in the Appendix. The results of this comparison can be summarized as follows: The (median) radial velocities of the clusters Tr 14, 15, and 16, and Bo 11 are very similar to the radial velocities of the clouds around each of these clusters. This suggests that these star clusters are still kinematically related to the surrounding clouds. For Tr 14, 15, and 16, evidence for expanding bubbles around these clusters is found in the form of gas velocity components with advancing and receding velocities with respect to the cluster velocity; the expansion velocities are around $\approx 10\,\mathrm{km\,s^{-1}}$, and provide a direct illustration of the action of massive star feedback on the surrounding gas.

Considering the large-scale kinematics of the molecular gas complex, variations of the mean radial velocity of $\approx \pm 10\,\mathrm{km\,s^{-1}}$ are present, but no strong systematic velocity gradient is seen over the extent of the cloud complex (on scales of ~ 100 pc; see Rebolledo et al., 2016). However, the Northern Cloud does show a systematic radial velocity gradient on a scale of ~ 20 pc, with a difference of $\approx 15\,\mathrm{km\,s^{-1}}$ between the northern and southern parts of the cloud. Similar velocity differences are also seen in the clouds surrounding Gum 31.

The velocity dispersion of the molecular gas, inferred from the typical observed CO line-widths, and the radial velocity ranges seen in the position-velocity diagram, is typically $\delta v_{\mathrm{rad}} \approx 10 \ldots 20\,\mathrm{km\,s^{-1}}$ in the Southern Cloud/Pillars and the Northern Cloud, and probably reflects the general turbulent motions within the cloud complex. The radial velocities of the individual clumps (Yonekura et al., 2005) and pillars (Klaassen et al., 2020) in the Southern Cloud & Pillars differ by up to $\approx 15\,\mathrm{km\,s^{-1}}$. This implies that individual clouds (clumps) can move by up to $\approx 15\,\mathrm{pc\,Myr^{-1}}$, and shows that the shape and morphology of the cloud complex has probably changed considerably during the last 10 Myr.

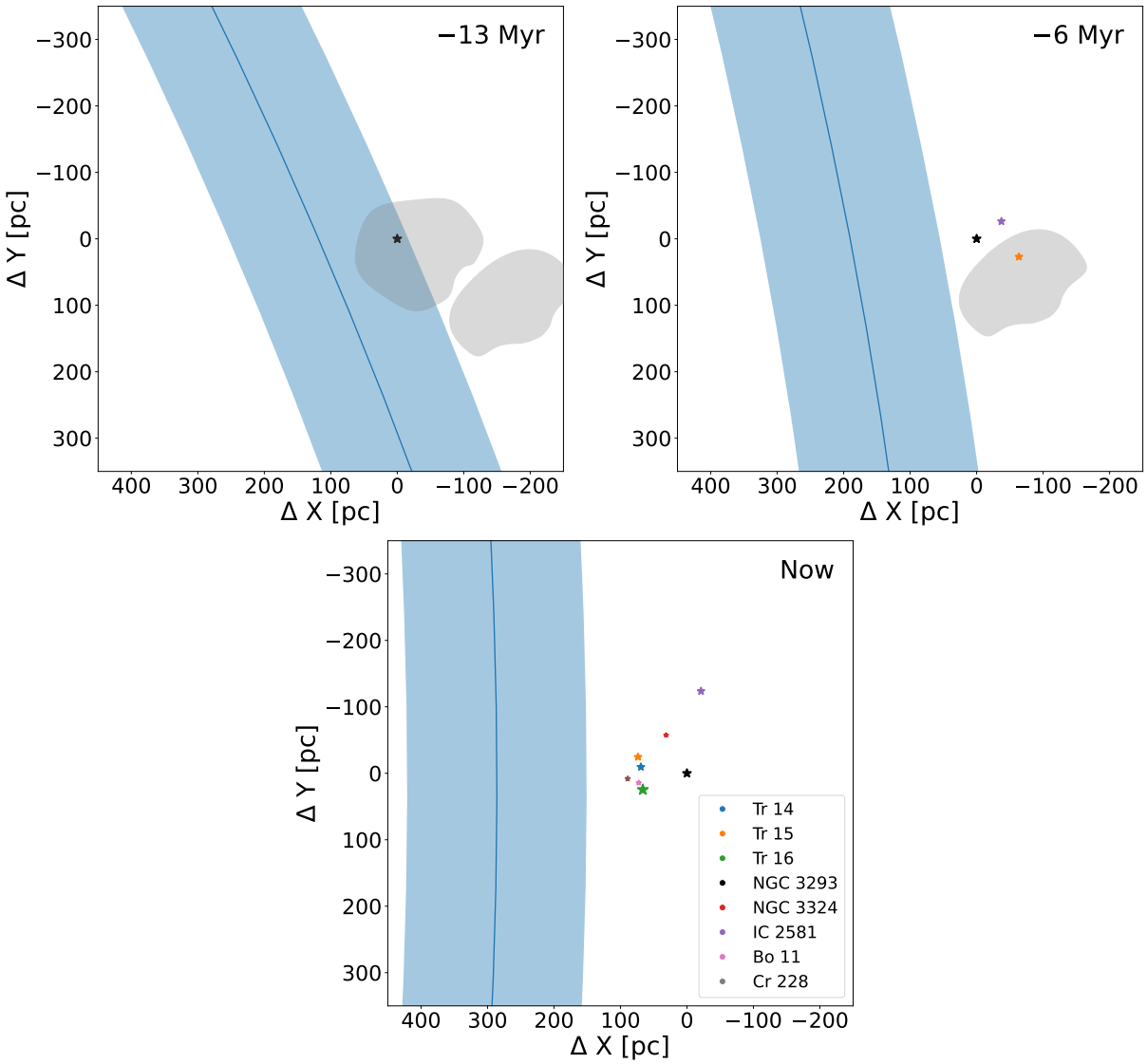

Figure 5.3: Galactic "bird's eye" (X, Y) view of the traceback and current positions of the Car OB1 clusters (asterisks) relative to NGC 3293, for times 13 Myr and 6 Myr ago and today. The blue line and shaded area show the location of the Carina spiral arm. The grey cloud-shaped areas illustrate the hypothetical positions of the two initial main cloud components out of which Car OB1 formed (see discussion in Sect. 5.4).

5.3.5 Kinematic Traceback of the Car OB1 Clusters

In order to explore how the galactic location and the spatial configuration of the clusters have changed with time, we utilize the galactic dynamics package `galpy` (Bovy, 2015) with the Milky Way's gravitational potential model[3] `MWPotential2014` (Bovy, 2015) to trace back the position of clusters in Car OB1 over the last 13 Myrs. For our analysis, we use a solar distance of $R_\odot = 8.23 \pm 0.12$ kpc (Leung et al., 2023) to the galactic center, a solar position of $z_\odot = 17 \pm 5$ pc (Karim & Mamajek, 2017) above the galactic mid-plane, and solar motion of $(U_\odot, V_\odot, W_\odot) = \left(11.1^{+0.69}_{-0.75}, 12.24^{+0.47}_{-0.47}, 7.25^{+0.37}_{-0.36}\right)$ km s^{-1} (Schönrich et al., 2010). We perform the traceback 1000 times, adding errors randomly weighted by a normal distribution to each cluster variable, and determine the mean position and standard deviation of each cluster at time steps of 0.1 Myr.

Large-scale motion of Car OB1 and the Carina spiral arm

In Figure 5.3, we show the positions of the Car OB1 clusters in the galactic plane at three different times: 13 Myr ago (when NGC 3293 formed), 6 Myr ago (when Tr 15 formed), and today. We also show the expected location of the Carina spiral arm according to Reid et al. (2019) at each time, assuming a galactic spiral pattern speed of $\Omega_p = 28.2\,\mathrm{km\,s^{-1}\,kpc^{-1}}$ (Dias et al., 2019). The traceback analysis suggests that NGC 3293 was born in the spiral arm, and has since then moved out of the arm to its current position of about 300 pc ahead of the arm center. The formation of NGC 3293 (which marks the start of the formation of the Car OB1 clusters) can therefore be understood as a consequence of the spiral arm passage of the original cloud. The other, younger, Car OB1 clusters formed later and apparently outside of the spiral arm.

Internal motions of the clusters in Car OB1

Figure 5.4 shows the motions of the clusters in Car OB1 relative to NGC 3293 over the last 13 Myr in the galactic (X, Y)-plane, and Fig. 5.5 for the last 6 Myr in the plane of the sky. Today, all clusters appear to move away from NGC 3293, with velocities of about $7 - 20$ km s^{-1}. Going back in time, the mean distance between the clusters gets smaller, until the most compact configuration is found $\approx$ 3–4 Myr ago. However, it is important to note that the pattern of expansion is *not* an "explosion"-like expansion from a central point. Rather, the traceback suggests that the clusters which today constitute the southern part of the association (or their respective progenitor clouds) moved tangentially past the cluster NGC 3293, and the minimum mean lateral distance between these clusters and NGC 3293 was reached about 3.5 Myr ago.

Continuing the traceback to earlier times leads again to more extended configurations. However, it has to be emphasized that the reliability of the traceback of the internal

[3] `MWPotential2014` models the three main gravitational components of the Milky Way with a Miyamoto-Nagai potential for the disk (Miyamoto & Nagai, 1975), a power-law density spherical profile with an exponential cut-off for the bulge, and a Navarro-Frenk-White profile for the dark-matter halo (Navarro et al., 1997).

motions of the clusters within Car OB1 gets increasingly limited if one goes back in time, since `galpy` only uses the galaxy's gravitational potential for the calculation; neither the influence the clusters exert on each other, nor the gravitational interaction between the clusters and the surrounding (very massive, several 100 000 $M_\odot$) cloud complexes is taken into account. Therefore, while the traceback positions up to 4 Myr in the past should be reliable, the calculated positions at earlier times are increasingly uncertain.

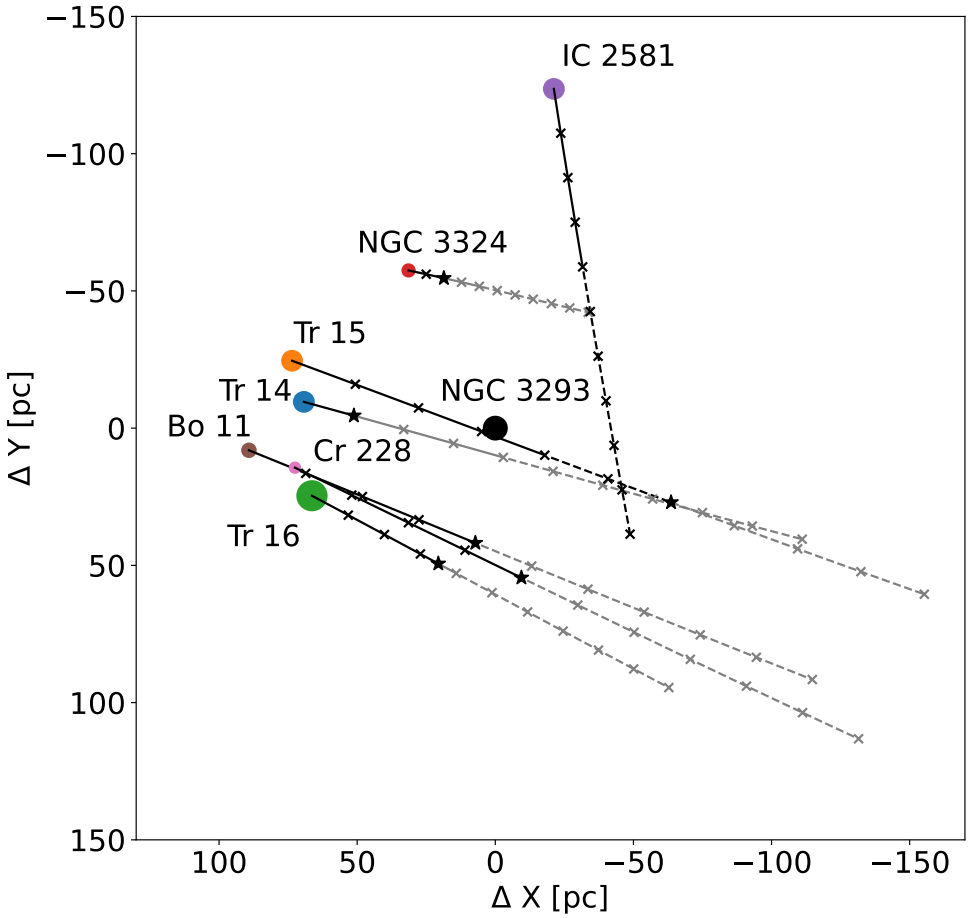

Figure 5.4: Paths of the clusters relative to NGC 3293 in the galactic (X, Y) plane. The paths before 4 Myr ago are plotted with dotted lines, and the crosses show the cluster position for each Myr. The asterisk visualizes the time at which the cluster is formed. Corresponding plots for the paths in the (X, Z) and (Y, Z) planes are shown in Fig. 5.8

Nature of the apparent large-scale expansion

The limited reliability of the traceback for ages of more than about 4 Myr in the past may raise the question, whether the currently observed apparently expanding motion of the clusters in the southern part of Car OB1 away from NGC 3293 with velocities of

$\approx 20\,\mathrm{km\,s^{-1}}$ could alternatively be explained by the effect of stellar feedback on the cloud complex, i.e. whether the series of ≈ 11 supernova explosions in NGC 3293 might have accelerated the cloud complex radially away from NGC 3293.

Although the 3D motions of the clouds cannot be measured, the good and general agreement between the cloud and cluster radial velocities described above suggests that the clusters are still kinematically connected to their surrounding clouds. With a total current cloud mass of $\sim 10^6\,M_\odot$, the momentum of this global expansion in Car OB1 is estimated as $\approx 2 \times 10^7\,M_\odot\,\mathrm{km\,s^{-1}}$. Following the discussion in Quintana & Wright (2022), this number can be compared to the simulation results from Kim & Ostriker (2015), who found that ten supernovae inject a total momentum of about $2 \times 10^6\,M_\odot$ km s^{-1} into the surrounding clouds. This comparison shows that the expected total momentum from the 11 supernovae in NGC 3293 is (at least) a factor of ten too low to explain the kinematics of the large-scale expansion in Car OB1. Therefore, the global motion of the southern clusters away from NGC 3293 cannot be explained as a global expansion due to supernova feedback (and even less by radiative and stellar wind feedback). It appears much more likely that it is related to the initial kinematics of the various parts of the original cloud complex in which Car OB1 formed. This supports the idea that OB associations are born in unbound cloud complexes, and their expansion is a consequence of the strong original intrinsic turbulent velocity dispersion of the individual components of the cloud complex.

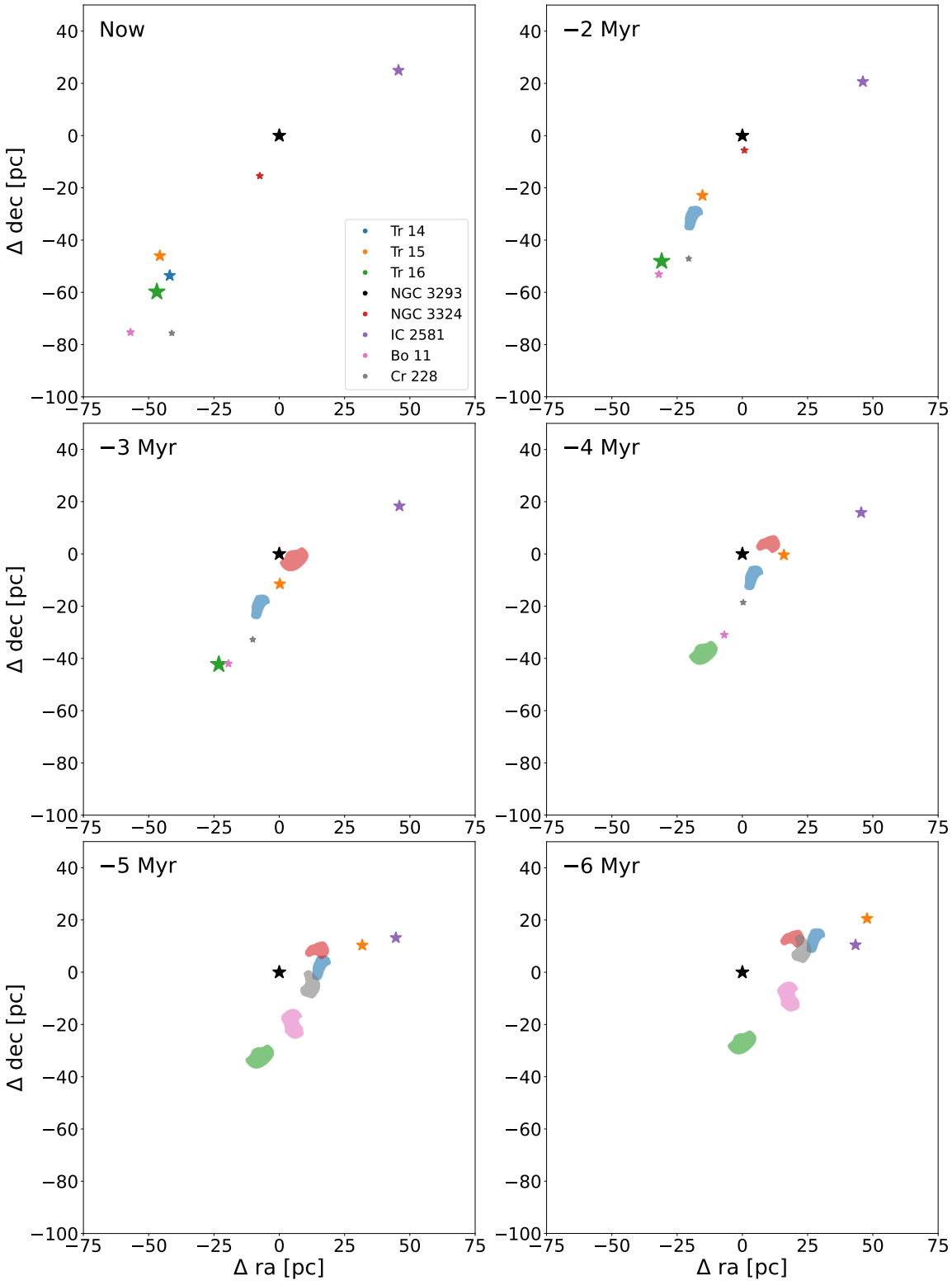

Figure 5.5: Traceback positions of the clusters in Car OB1 relative to the position of NGC 3293 (fixed at (0,0)), in the plane of the sky, from today until 6 Myr in the past. The cluster positions are shown by asterisks, which are replaced by cloud-like shapes according to the age of the individual clusters.

5.4 A Formation & Evolution Scenario for Car OB1

5.4.1 Triggered Star Formation in Car OB1

Today, we see two different kinds of triggered star formation currently at work in the CNC: The first mechanism is radiative triggering, where the strong irradiation from the massive stars in Tr 16 and 14 compresses the clouds in the Southern Pillars (Smith et al., 2010), which leads to cloud collapse and star formation. In a highly inhomogeneous cloud complex like the Southern Pillars, this mechanism is expected to create individual stars or small stellar groups/clusters.

The second way of current triggering is by the expansion of an H II region. The expansion collects cloud material at the edge of an H II bubble and compresses it, until cloud collapse and star formation set in ("collect & collapse model", see Elmegreen & Lada, 1977). This is seen at the rim of the H II region Gum 31 around NGC 3324, where a dense shell has been swept up. In some parts of this rim, a very recent episode of star formation has created embedded clusters of very young stellar objects; prominent examples are the embedded cluster G286.38 − 0.26 (see Ohlendorf et al., 2013) at the southern rim of the H II region, or the numerous embedded protostars revealed by the famous JWST image[4] of the "Cosmic Cliffs" at the western edge of the rim (see Crompvoets et al., 2024, for an analysis of the very young stellar population embedded in this rim).

These two mechanisms, radiative triggering and expanding H II regions, are thought to produce small stellar groups or moderate-sized clusters, and are probably the main source for the widely distributed population of young stars seen throughout the whole Car OB1 association (and in other associations).

A third way of triggering star formation is the interaction of expanding large-scale (super)-bubbles, driven by stellar winds and supernova explosions in a massive cluster, with another molecular cloud at a suitable distance (e.g. Krause et al., 2013, 2014, 2018). While the effect of a supernova shock wave is very destructive for the cloud in which the supernova explodes (e.g. Lucas et al., 2020), there are numerous observations suggesting that supernova bubbles trigger star formation in other clouds at distances of at least $\gtrsim 10$ pc and up to $\lesssim 100$ pc. Examples have been found in nearby regions (Zucker et al., 2022), in other galactic OB associations (e.g., Oey et al., 2005; Lee & Chen, 2009; Krause et al., 2018), and on galaxy scales (e.g., Egorov et al., 2018).

Supernova-driven bubbles reach typical radii of a few tens of parsecs within a few Myr (e.g. Krause et al., 2013). The further expansion of the bubble generally slows down with time, but each subsequent supernova increases the pressure in the bubble again. If the bubble interacts with another cloud, each pressure increase by a subsequent supernova will increase the compression of the cloud again, and may drive further parts of the cloud into collapse. This is illustrated by Krause et al. (2018) with their "Surround and Squash" model, which shows how expanding super-bubbles can strongly change the large-scale morphology of the clouds during the interaction. This large-scale interaction can efficiently

[4] https://webbtelescope.org/contents/news-releases/2022/news-2022-031

redistribute and concentrate large amounts of gas at specific locations. If such a massive, dense cloud clump subsequently experiences a further episode of compression (since a further supernova explosion increases the pressure in the bubble), this may lead to the formation of a massive star cluster. Supernova feedback is therefore a suitable way to form rather massive star clusters (e.g., Rathjen et al., 2021), and a good explanation for the formation of the massive clusters in Car OB1.

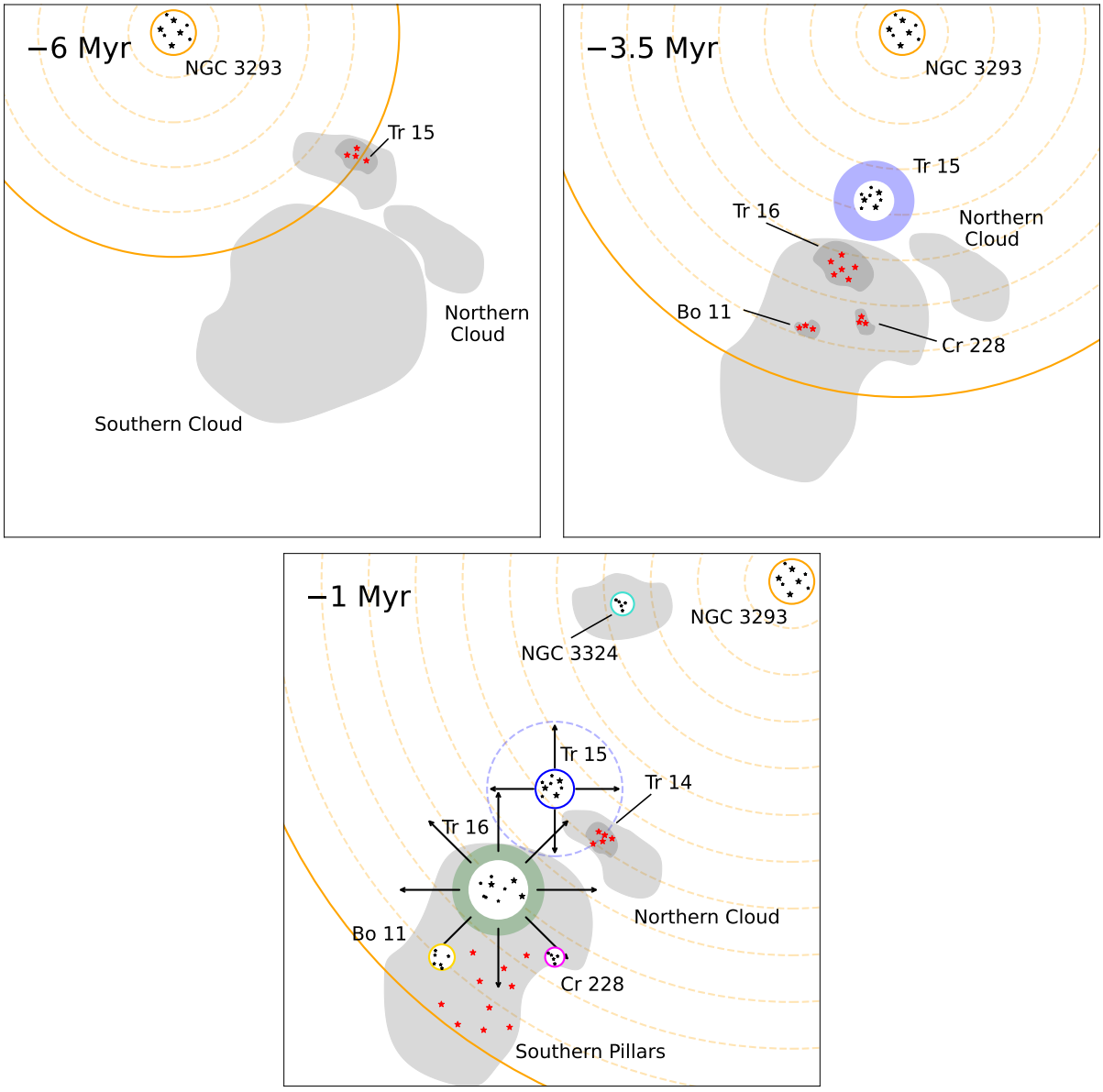

Figure 5.6: Illustrative sketch (not to scale) of the formation scenario for the clusters in the central part of Car OB1, visualizing the compression and triggering effects of the expanding bubble shocks on clouds.

5.4.2 A Formation Scenario for Car OB1

Today, the total mass of the clouds observed in Car OB1 is $\sim 10^6\ M_\odot$ (Smith & Brooks, 2007; Preibisch et al., 2012; Rebolledo et al., 2016); about 10% of this cloud mass is in the form of dense ($A_V > 3$ mag) clouds today, while 90% of the gas mass is in a more diffuse, low-density phase. The total stellar population comprises about $\approx 10^5$ stars, which implies a total stellar mass of $\approx 50\,000\ M_\odot$.

The large majority of dense cloud mass present today is located in the southern parts of Car OB1 (i.e., the CNC), whereas only very little dense cloud material is seen in the northern part of Car OB1. However, the morphology of the original cloud complex, before the start of star formation, must have been very different from what we see today, because the oldest clusters are located at the northern edge of the association. Based on our results for the cluster trajectories from the traceback, cluster ages, and the estimated numbers and times of supernovae, we propose the following cluster formation scenario for Car OB1, which is illustrated in Figure 5.6.

Initial conditions: The original cloud complex consisted of two main components: one complex out of which NGC 3293 (and perhaps IC 2581) formed, and another one, out of which Tr 14, 15, and 16, Bo 11, and Cr 228 formed. These two cloud complexes were moving past each other with relative velocities of about 10–20 km s^{-1}. The cloud complex forming NGC 3293 and IC 2581 is no longer present, since the 13 supernova explosions that happened during the last 10 Myr in this area have completely dispersed the original clouds. The (remnants of the) cloud complex in which Tr 14, 15, and 16, Bo 11, and Cr 228 formed, does now constitute the Southern Cloud, Southern Pillars, and Northern Cloud.

START: Formation of NGC 3293 Star formation in Car OB1 started $\approx$ 13 Myr ago in the northern part of the original Car OB1 cloud complex with the formation of NGC 3293. Our traceback analysis suggests (see Fig. 5.3) that NGC 3293 formed inside the Sagittarius-Carina spiral arm, presumably due to cloud compression in the spiral shock, and then moved out of the arm within a few Myr.

NGC 3293's initial population of 14 O-type stars created an expanding H II region and irradiated the surrounding clouds; this stellar feedback started to create the distributed population of young stars in the northern part of Car OB1. After about 4 Myr (i.e., $\approx$ 9 Myr ago), the most massive O-type star in NGC 3293 exploded as a supernova. This first explosion was probably soon (within $\lesssim$ 1 Myr) followed by the next supernova (11 supernovae within 8 Myr), and within a few Myr, an expanding superbubble was formed around NGC 3293. The feedback from this series of supernovae has now completely dispersed the original cloud in which NGC 3293 had formed. The massive clouds in the southern part of Car OB1, which were $\gtrsim 20 - 50$ pc away from NGC 3293 at that time, were not destroyed by the supernovae in NGC 3293, but instead experienced a sequence of shock waves that (i) presumably strongly changed the global structure of the original cloud complex, and (ii) provided a series of compressions on these clouds that triggered star formation in subsequent steps.

STEP 2: Formation of Tr 15 About 3 Myr after the first supernova in NGC 3293 (i.e., about 6 Myr ago), about 3–4 further supernovae should have exploded in NGC 3293; the compression of this expanding superbubble on a cloud (the remnants of which are now seen as the north-eastern part of the Northern Cloud) triggered the formation of Tr 15. While we do not have exact inter-cluster distances for this timeframe, the distance between the progenitor cloud of Tr 15 and NGC 3293 was very likely smaller than today, probably between 20 pc and 40 pc. The superbubble had thus already interacted for several Myr with the cloud in which Tr 15 formed, and had time to compress and accelerate this cloud. Tr 15 is now moving almost exactly radially away from NGC 3293 with a space velocity of 23.8 $\mathrm{km\,s^{-1}}$; while a large part of this motion is probably related to the general kinematics and the large-scale velocity gradient in the association, this particularly high relative velocity is consistent with the idea that the formation of Tr 15 was induced by shock wave compression from the direction of NGC 3293.

STEP 3: Formation of Tr 16 (and Bo 11, Cr 228) Tr 16 formed 3.5 Myr ago, i.e $\approx$ 5.5 Myr after the first supernova in NGC 3293, and at a distance of $\approx$ 60 pc from NGC 3293. At that time, we can expect that about 5–7 supernovae had already happened in NGC 3293, which sustained the superbubble and increased the pressure in the bubble. Tr 16 is located (as seen from NGC 3293) at the "head", i.e. the northern edge of the Southern Cloud & Pillars cloud complex, which has a total cloud mass of $\approx 200\,000\ M_\odot$ today. The counter-pressure by this massive cloud complex allowed the formation of the particularly large cluster Tr 16. The somewhat smaller clusters Bo 11 and Cr 228, farther south, formed approximately simultaneously to Tr 16, presumably also by the advancing shock wave from the expanding NGC 3293 superbubble.

STEP 4: Formation of Tr 14 The birth of the particularly dense and massive cluster Tr 14 about one Myr ago seems to be related to the combined influence of three factors:

(i) the superbubble from NGC 3293 (at a distance of 56 pc), compressing the cloud in which Tr 14 formed from the north-west direction. At the time when Tr 14 formed, 11 supernovae had already exploded in NGC 3293, and the bubble had already interacted with the cloud for several Myr. This interaction has presumably swept up a particularly dense and massive clump.

(ii) the first supernova that had happened in Tr 15 (at a distance of 13 pc) about 1 Myr before the formation of Tr 14.

(iii) the irradiation from the 35 high-mass stars in Tr 16 at a distance of 37 pc.

Assuming a typical star formation efficiency of $\lesssim 5\%$, the mass of the progenitor cloud of Tr 14 must have been $\gtrsim 100\,000\ M_\odot$. This dense cloud received pressure from the north-western direction (from the NGC 3293 superbubble), a supernova-shock wave coming from the north-east (from Tr 15), and strong irradiation from the east (Tr 16). The very massive progenitor cloud, the remnants of which now constitute the Northern Cloud, would have

provided counter-pressure for the advancing superbubble and supernova shockwaves, which increased the compressing effect of the bubble shock waves and enabled a particularly large and dense cluster to be created. We note that the dense cloud seen today just west of Tr 14 (which is the densest and most massive ($\sim 45\,000\ M_\odot$) cloud structure present in the entire cloud complex today) is in the opposite direction from Tr 15, as seen from Tr 14. This may suggest that a shock wave from the direction of Tr 15 was a decisive ingredient for the formation of Tr 14 at this position.

STEP 5: Recent and current triggered star formation in the Southern Pillars and the Gum 31 rim: The distributed stellar population in the Southern Pillars has a range of ages between $\lesssim 1$ Myr and ≈ 4 Myr (Getman et al., 2014). This can be understood by assuming that these distributed stars have been formed by the radiative triggering from Tr 16 (and Bo 11 and Cr 228) over the last 4 Myr. Since this feedback is still ongoing, it currently forms the youngest embedded populations in this area (see Smith et al., 2010). The rim of the Gum 31 bubble constitutes the second "hotspot" of current star-forming activity in the association (see Ohlendorf et al., 2013; Crompvoets et al., 2024).

NGC 3324: This ≈ 2 Myr old cluster is spatially separated from the clusters in the southern part of Car OB1, but it shares a similar kinematics: it moves in a similar direction as the southern clusters, although with a lower velocity. The cluster appears to be related to the rather massive cloud complex surrounding the Gum 31 H II region in the southern and western direction. While NGC 3324 and NGC 3293 appear to be rather close together on the sky, their actual 3D-distance is about 66 pc. Our traceback suggests that, at the time of its formation, NGC 3324 had a 3D separation of 58 pc from NGC 3293; thus, its formation may have been influenced by the expanding superbubble around NGC 3293.

IC 2581: This cluster appears to be an "outlier". It is located at the extreme north-western periphery of Car OB1, about 100 pc more distant than NGC 3293, and shows a distinct kinematics, moving in a completely different direction than the other clusters. At the cluster age of ≈ 12 Myr, it is not surprising that no clouds are seen anymore related to the cluster.

The traceback puts it at a distance of 90 pc from NGC 3293 at the time of cluster formation. This rather large separation, combined with the small (1 Myr) difference in ages, suggests that its formation can probably not have been affected by NGC 3293.

5.4.3 Comparison to formation scenarios for other OB associations

The scenario we propose here for Car OB1 is different from, and more complex than, the sequential cluster formation model for the "cluster chains" in Sco-Cen (Posch et al., 2025), where the formation of each cluster is triggered by the feedback of the most recently formed cluster in an approximately linear sequence (in space and time). But we note that similar

formation scenarios, in which one cluster has a dominant impact on the formation of several other clusters in an association through feedback, were proposed, e.g., in Großschedl et al. (2021) for the Orion cloud complex and in Kerr et al. (2025) for the Circinus Complex.

Another notable difference of our scenario for Car OB1 from the triggered star formation model for Sco-Cen is that we do *not* find a systematic decrease of cluster size in the subsequent generations, as observed in Sco-Cen: in Car OB1, the relatively young clusters Tr 14 and 16 are the most massive clusters in the whole association, and substantially more massive than the intermediate-age cluster Tr 15 as well as the oldest cluster NGC 3293. However, we note that the current star formation activity in the Southern Pillars does not seem to form large clusters: all (embedded) clusters in the Southern Pillars region (e.g., Smith et al., 2005; Povich et al., 2011; Preibisch et al., 2011b; Oliveira et al., 2018) are (much) smaller than Tr 14 and 16. The most massive sub-mm clumps in the cloud complex have masses of $\approx 2000\ M_\odot$ (Preibisch et al., 2011c; Pekruhl et al., 2013), and with an assumed star formation efficiency of $\approx 5\%$, these may form clusters with at most ≈ 100 stars. This implies that the process of (radiatively) triggered star formation going on today in the Southern Pillars is a fundamentally different mode of star formation than the processes that led to the formation of the massive clusters Tr 14 and 16.

The difference in the observation of decreasing cluster masses in the subsequent populations seen in Sco-Cen can presumably be explained by the total cloud mass in the associations. The cluster chains in ScoCen have residual gas masses ranging from 300 to $11\,000\ M_\odot$ available (Posch et al., 2025) with a total gas mass of $368\,000\ M_\odot$ today in the full association (Pöppel et al., 2010), while the Carina Nebula harbors $\approx 10^6\ M_\odot$ in gas. The difference in gas mass is also apparent in the most massive stars that are formed in the associations: there are no O-type stars formed in the young clusters of Upper Sco, e.g, ρ Oph, while Tr 16 by itself already hosts 35 high-mass stars with stellar masses up to $100\ M_\odot$. Furthermore, this also offers an explanation as to why the clusters in Car OB1 do not follow a clear age chain, as gas is more ubiquitous in the Car OB1 association and star formation can be induced in several directions. In comparison, the Sco-Cen association has less gas available, which is pushed by the high-mass stars along chains (Ratzenböck et al., 2023a).

The lower initial total cloud mass in Sco-Cen also explains why the original cloud material there is almost completely dispersed today (after about 15 Myr of stellar feedback). The initially about three times higher total cloud mass in the CNC requires considerably more feedback energy to be dispersed, and thus we still see about $175\,000\ M_\odot$ of dense cloud material, in which star formation is still ongoing at a high rate.

5.5 Summary

In this study, we took a detailed look at the massive star clusters in Car OB1 and proposed a star formation scenario for the association. We have estimated the cluster member sizes based on their high-mass star population and estimated that in total 15 ± 5 supernovae have occurred in the Car OB1 association during the last ~ 9 Myr so far. Using a traceback of the

cluster's positions, we proposed a star formation scenario in which the spiral arm passage of the original cloud complex initiated star formation by creating the cluster NGC 3293 13 Myr ago. We suggest that the feedback of the 11 supernovae from NGC 3293, in combination with the later supernovae in Tr 15 and the irradiation from high-mass stars in cluster Tr 16, has led to the formation of the massive clusters in Car OB1.

Our conclusion that the observed global expansion of Car OB1 is probably *not* the result of stellar feedback, but rather due to the initial intrinsic kinematics of the original clouds, adds further support to the notion that OB associations form in unbound cloud complexes, and their large-scale expansion is due to the initial dynamics of the clouds (see, e.g., Ward et al., 2020).

5.A Relation between the clusters and the surrounding clouds

In order to investigate the physical relation between the star clusters and the surrounding clouds, we compare the radial velocities. For this, one has to translate the radial velocities reported in the literature for molecular emission lines from clouds, which are usually given relative to the "local standard of rest" (LSR), to the barycentric velocity system, in which the stellar radial velocities are given. In the direction of the Car OB1 clusters, the typical[5] difference between the LSR and barycentric radial velocity (see Reid et al., 2009, for details of the computation) is $\simeq 11.6\,\mathrm{km\,s^{-1}}$.

In the following, we use barycentric radial velocities and consider the large-scale maps of molecular (CO) gas from Rebolledo et al. (2016, R16), atomic (H I) gas from Rebolledo et al. (2017, 2021, R17, R21), the velocities for the molecular clumps and pillars reported in Yonekura et al. (2005, Y05) and Klaassen et al. (2020, K20), and build on the results already reported by Kiminki & Smith (2018) for the central Carina Nebula.

Tr 14: The median radial velocity of the stars in Tr 14 of $\langle v_{\mathrm{rad}} \rangle = -7.1\,\mathrm{km\,s^{-1}}$ agrees well with the main peak radial velocity of the molecular gas in the Northern Cloud $v_{\mathrm{rad}} \simeq -8.2\,\mathrm{km\,s^{-1}}$ (R16), and also with the range of radial velocities of the CO clumps in the Northern Cloud of $[-8.3\ \ldots\ -6.0]\,\mathrm{km\,s^{-1}}$ (Y05).

The HI gas around Tr 14 shows radial velocity components at $-14.4\,\mathrm{km\,s^{-1}}$ and $+8.6\,\mathrm{km\,s^{-1}}$ (R17), tracing an expanding bubble around Tr 14, probably driven by the feedback from the massive stars. This gas is flowing away from the cluster with relative velocities of $\approx 7 - 15\,\mathrm{km\,s^{-1}}$. The expanding bubble is also seen in the radial velocities of ionized gas ($\approx -22\,\mathrm{km\,s^{-1}}$ and $\approx +10\,\mathrm{km\,s^{-1}}$) (see Fig. 11 and 12 in Kiminki & Smith, 2018).

[5]Individual values at the positions of the discussed clusters range from $11.48\,\mathrm{km\,s^{-1}}$ for Bo 11, over $11.56\,\mathrm{km\,s^{-1}}$ for Tr 16, to $11.89\,\mathrm{km\,s^{-1}}$ for NGC 3293.

Tr 16: The mean velocities of the molecular gas in the Southern Cloud (-13 km s^{-1}) and in the Southern Pillars (-10 km s^{-1}) (R16) are slightly more negative than the median star cluster velocity of $v_{\rm rad} = -7.18$ km s^{-1}.

The individual CO clumps (Y05) and pillars (K20) in the cloud complex show ranges of radial velocities of $[-14.2 \ldots -0.5]$ km s^{-1} and $[-14 \ldots +6.6]$ km s^{-1},

The atomic (HI) gas around Tr 16 shows components at -18.4 km s^{-1} and $+6.6$ km s^{-1} (R21), indicating an expanding shell around Tr 16 with an outward velocity of ≈ 10 km s^{-1}, which is probably driven by the feedback from the massive stars. This expanding shell is also seen in ionized gas at velocities of ≈ -20 km s^{-1} and $\approx +10$ km s^{-1} (see Kiminki & Smith, 2018).

Bo 11: The (poorly constrained) cluster radial velocity of -4.25 km s^{-1} agrees approximately with the mean velocity of the surrounding molecular gas of $\approx -10 \ldots -5$ km s^{-1} (R16).

Cr 228: The CO map of R16 does not show a significant detection of CO emission at the position of the cluster. The (poorly constrained) cluster radial velocity of -2 km s^{-1} is higher than the typcial mean velocity of the surrounding molecular gas of ≈ -14 km s^{-1} (R16).

Tr 15: The molecular gas near Tr 15 shows peaks at radial velocities of $-8.4, -3.4$, and $+3.6$ km s^{-1} (R16, Fig. 4). Given the median cluster radial velocity of $\langle v_{\rm rad} \rangle = -2.72$ km s^{-1}, this suggest an expanding shell around the cluster, (as discussed by Kiminki & Smith, 2018), where gas is blown away from Tr 15 with an outward velocity of $\approx 5 - 6$ km s^{-1}.

NGC 3324: The (poorly constrained) cluster radial velocity of $\langle v_{\rm rad} \rangle \approx -12.8$ km s^{-1} is similar to the general molecular gas velocity in the Gum 31 cloud of ≈ -10.4 km s^{-1} (R16), as well as the velocity range of $[-12.4 \ldots -8.4]$ km s^{-1} for the CO clumps in this area (Y05). The atomic (HI) gas shows components at -8.4 km s^{-1} and -2.4 km s^{-1} (R21), suggesting that the gas moves away from us relative to the cluster.

However, given the large uncertainty of the cluster radial velocity and the fact that the radial velocities in the Gum 31 region show a very complex pattern with strong variations (R16), this result should be treated with caution.

NGC 3293: The CO maps show a very complicated velocity distribution at the position of NGC 3293. The CO emission at that position is, however, probably strongly dominated by gas from the extended Gum 31 cloud as well as clouds in the galactic background. Considering that about 11 supernova explosions have happened in NGC 3293 over the last ten Myr, their impact should have dispersed the natal cloud of NGC 3293.

5.B Supplemental Tables and Plots

Table 5.3: Estimates for the mass and lifetime of the (initially) most massive star in each cluster, and the time of the first supernova explosion.

Cluster	$\mathcal{E}[N_{\mathrm{SN}}]$	age (Myr)	$M_{cl} - M_{*,\max}$-relation $M_{*,\max}$ ($M_\odot$)	τ_{MS} (Myr)	IMF $M_{*,\max}$ ($M_\odot$)	τ_{MS} (Myr)	time of first SN (Myr from today)
NGC 3293	11	13	43	≈ 4.3	64	≈ 3.4	≈ -9
IC 2581	2	12	28	≈ 6.5	38	≈ 4.9	≈ -7
Tr 15	2	6	39	≈ 4.7	57	≈ 3.6	≈ -2

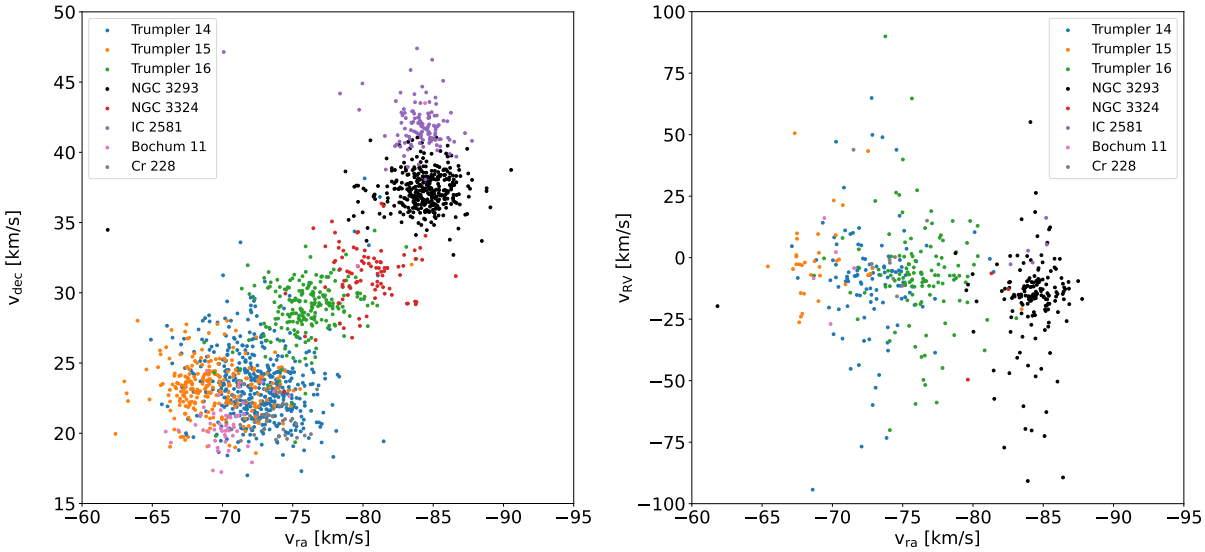

Figure 5.7: Tangential and radial velocities of the individual stars in each cluster.

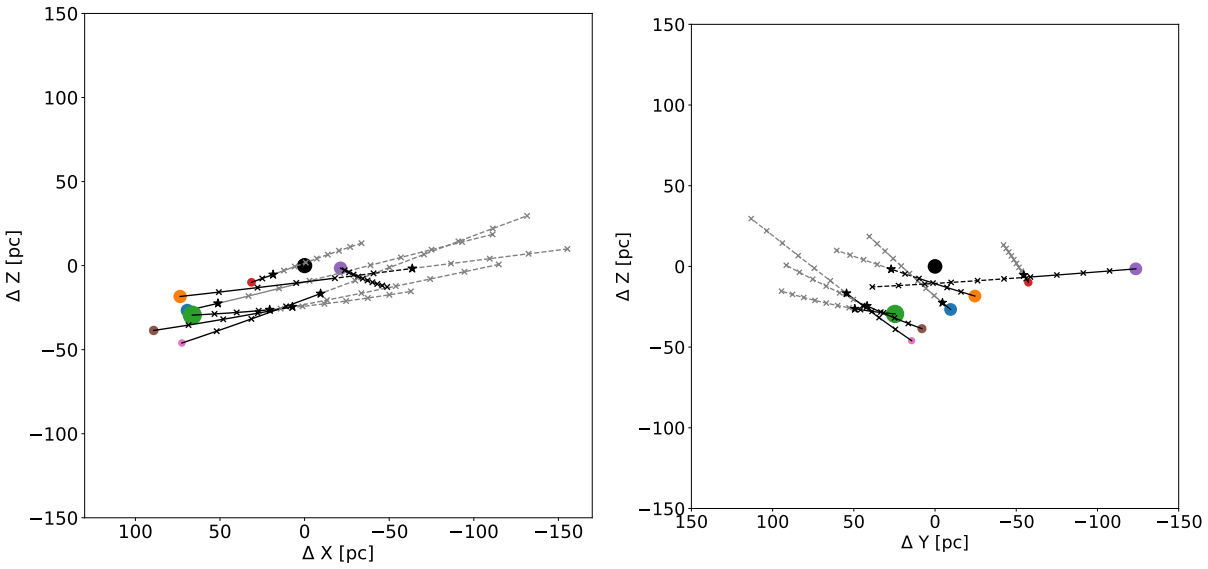

Figure 5.8: Paths of the clusters relative to NGC 3293 in the (X, Z) plane and the (Y, Z) plane. The path before 4 Myr ago is plotted dotted, and the crosses show the cluster position for each Myr. The asterisk visualizes the time at which the cluster is formed.

CHAPTER 6

SUMMARY AND OUTLOOK

In this thesis, a spatially complete characterization of the Carina OB1 association and a scenario for its star formation history were presented.

In the third chapter, we analysed *Gaia* DR3 data to carry out an unbiased search for stellar groups and clusters over the full extent of the Car OB1 association, resulting in 15 clusters and groups. We determined that four out of the six subgroups defined in Mel'Nik & Efremov (1995) for the Car OB1 agree well with our distribution of clusters and groups.

In order to better investigate the high-mass star population of the association, we first compiled a catalog of spectroscopically identified high-mass stars from the literature that have compatible distances. We then extended our catalog with stars whose *Gaia* effective temperature indicates them to be high-mass stars, which we denote as high-mass star candidates. This resulted in a list of 1374 spectroscopically confirmed high-mass stars and candidates, out of which 74% are part of the distributed population. This is a significant increase in the distributed population fraction, as previous surveys have found 49% through X-ray observations (Feigelson et al., 2011) and 53% for YSOs (Zeidler et al., 2016). Considering the young ages of high-mass stars, this shows that the majority of the distributed population was formed unbound outside of clusters. This, along with the high number of distributed stars, highlights the need for spectroscopic observations outside of clusters to learn more about the history of the association and the birthplace of the distributed population.

Combining our high-mass star and candidate catalog with the Kroupa IMF led to a total extrapolated stellar population of $\approx 8 \times 10^4$ in the association, which makes the Car OB1 the most massive, well-studied OB association in our Galaxy. Tracing back the positions of all the high-mass stars in the association, we found that the Car OB1 association had its smallest extent $3 - 4$ Myr ago.

We studied the kinematics of the individual clusters and determined that 80% of the Car OB1 clusters show signs of either expansion or contraction, with three clusters exhibiting them at significances larger than 2σ. This includes Tr 14, whose analysis resulted in

the highest expansion significance in our sample with a significance of 5.2σ. For clusters, which show higher significances of expansion, i.e., Tr 14 and Tr 16, the kinematic ages agree well with the ages determined in the literature using CMDs.

In the fourth chapter, we tested our method for analyzing cluster kinematics on numerical clusters. For this, we simulated a virialized non-expanding cluster and an expanding cluster modeled after Tr 14. We explored the impact of taking uncertainties into account for our method of expansion detection and found that our method recovers the underlying kinematic properties of the clusters, i.e., whether the cluster is expanding or static.

In the fifth chapter, we took a closer look at the proper motions of the individual clusters and constructed a star-forming scenario for the whole association. For this, we performed a traceback of the cluster positions over the last 13 Myr. We found that the oldest cluster of the association, NGC 3293, was located in the Sagittarius-Carina spiral arm at the time of its formation, 13 Myr ago. NGC 3293 used to host ten O-type stars during its lifetime, which led to the creation of a superbubble around it, sustained and pressurized by eleven supernovae. Considering the distances between NGC 3293 and other clusters in Car OB1 at the time of their formation, the compression of massive clouds by the shell of the superbubble contributed to the formation of Tr 14, 15, and 16.

With the release of *Gaia* DR4 at the end of 2026, positions, distances, and motions for the stars in Car OB1 will be available with even higher accuracy as DR4 is based on 66 months of observations, a significant increase compared to the 34 months for DR3. A larger improvement is especially expected for high-mass stars, as they are often part of multiple star systems, and DR4 will carry out astrometric fitting using the best-suited model, including binary-star models. *Gaia* DR3 astrometric fitting was by default based on a single-star model, which at times resulted in poor astrometric fits for multiple systems. Given the significant increase in available radial velocities from DR2 to DR3, it can be assumed that this trend will likely continue for DR4.

With more accurate astrometry and photometry for more stars, the kinematic past and present of the individual star clusters and the overall association can be probed in even more detail and at higher accuracy. *Gaia* DR4 will also contain improved astrophysical parameters for hot stars, which will make it possible to follow up on the distributed high-mass stars even further. This is crucial as they make up the majority of high-mass stars in the association.

As mentioned in Sect. 1.3.2, the FUV irradiation of proto-planetary disks influences their evolution and has likely consequences for the formation of exoplanets. While highly irradiated disks were observed in NGC 6537, e.g., XUE 1 (Ramírez-Tannus et al., 2023), which is exposed to a FUV field of $\approx 10^5\,G_0$, the Car OB1 contains high-mass stars that produce even stronger FUV fields. One of them is the massive multiple system HD 93129, which is located in the cluster Tr 14. It is comprised of HD 93129 A, which itself is a binary with two supergiants of spectral type O2 If* (Maíz Apellániz et al., 2017), and HD 93129 B with spectral type O3.5 V((f)) (Sota et al., 2014). At projected distances of 0.1 pc, the FUV field around this system can reach up to $10^6 - 10^7\,G_0$.

With the FUV field strength ranging from $\approx 10^3$ up to $\approx 10^7\,G_0$ in Tr 14, the cluster offers a wide range of local FUV environments to study the disk evolution, e.g., the lifetime of the disk, the disk fraction, and the chemical evolution. To investigate these questions, ≈ 340 proto-planetary disks in Tr 14 were observed with JWST in March, May, and June 2025 as part of Cycle 3 (GO-5791, PI: Michael Kuhn). The targets were imaged at wavelengths of 2.12 and 4.66 µm, which were complemented by NIRSpec mid-IR spectroscopy at wavelengths of $1.0 - 1.9$ µm and $2.9 - 5.3$ µm over a total observation time of 21.2 h.

As a large fraction of stars, and therefore a large fraction of exoplanets, in our Galaxy are born in associations like Car OB1, the association offers an ideal laboratory to explore their formation even more. With knowledge of the clusters and high-mass stars, both clustered and distributed, their impact on young stars can be quantified even more accurately. With further advancements in astrometric data and new observations of highly irradiated disks, the next years will bring exciting results about how the environment affects stars and exoplanets during their formation in Car OB1.

BIBLIOGRAPHY

Adams, F. C. 2010, ARA&A, 48, 47

Alexander, M. J., Hanes, R. J., Povich, M. S., & McSwain, M. V. 2016, AJ, 152, 190

Andrews, S. M., Huang, J., Pérez, L. M., et al. 2018, ApJ, 869, L41

Ansín, T., Gamen, R., Morrell, N. I., et al. 2023, MNRAS, 525, 4566

Arakawa, S. & Kokubo, E. 2023, A&A, 670, A105

Bamba, A. & Williams, B. J. 2022, in Handbook of X-ray and Gamma-ray Astrophysics, ed. C. Bambi & A. Sangangelo, 77

Berlanas, S. R., Mahy, L., Herrero, A., et al. 2025, A&A, 695, A248

Berlanas, S. R., Maíz Apellániz, J., Herrero, A., et al. 2023, A&A, 671, A20

Bica, E., Pavani, D. B., Bonatto, C. J., & Lima, E. F. 2019, AJ, 157, 12

Bik, A., Henning, T., Wu, S.-W., et al. 2019, A&A, 624, A63

Bovy, J. 2015, ApJS, 216, 29

Braun, R., Goss, W. M., & Lyne, A. G. 1989, ApJ, 340, 355

Bressan, A., Marigo, P., Girardi, L., et al. 2012, MNRAS, 427, 127

Briceño, C., Preibisch, T., Sherry, W. H., et al. 2007, in Protostars and Planets V, ed. B. Reipurth, D. Jewitt, & K. Keil, 345

Broos, P. S., Getman, K. V., Povich, M. S., et al. 2011, ApJS, 194, 4

Cantat-Gaudin, T., Anders, F., Castro-Ginard, A., et al. 2020, A&A, 640, A1

Cantat-Gaudin, T., Jordi, C., Vallenari, A., et al. 2018, A&A, 618, A93

Cantat-Gaudin, T., Mapelli, M., Balaguer-Núñez, L., et al. 2019, A&A, 621, A115

Carraro, G., Romaniello, M., Ventura, P., & Patat, F. 2004, A&A, 418, 525

Castro-Ginard, A., Jordi, C., Luri, X., et al. 2020, A&A, 635, A45

Castro-Ginard, A., Jordi, C., Luri, X., et al. 2022, A&A, 661, A118

Castro-Ginard, A., Jordi, C., Luri, X., et al. 2018, A&A, 618, A59

Chabrier, G. 2005, in Astrophysics and Space Science Library, Vol. 327, The Initial Mass Function 50 Years Later, ed. E. Corbelli, F. Palla, & H. Zinnecker, 41

Chen, B., D'Onghia, E., Alves, J., & Adamo, A. 2020, A&A, 643, A114

Colín, P., Vázquez-Semadeni, E., & Gómez, G. C. 2013, MNRAS, 435, 1701

Crompvoets, B. L., Di Francesco, J., Teimoorinia, H., & Preibisch, T. 2024, AJ, 168, 63

Damiani, F., Klutsch, A., Jeffries, R. D., et al. 2017, A&A, 603, A81

Damiani, F., Prisinzano, L., Pillitteri, I., Micela, G., & Sciortino, S. 2019, A&A, 623, A112

de Bruijne, J. H. J. & Eilers, A. C. 2012, A&A, 546, A61

de Geus, E. J. 1992, A&A, 262, 258

Delgado, A. J., Alfaro, E. J., & Yun, J. L. 2011, A&A, 531, A141

Della Croce, A., Dalessandro, E., Livernois, A., & Vesperini, E. 2024, A&A, 683, A10

Dias, W. S., Alessi, B. S., Moitinho, A., & Lépine, J. R. D. 2002, A&A, 389, 871

Dias, W. S., Monteiro, H., Caetano, T. C., et al. 2014, A&A, 564, A79

Dias, W. S., Monteiro, H., Lépine, J. R. D., & Barros, D. A. 2019, MNRAS, 486, 5726

Dias, W. S., Monteiro, H., Moitinho, A., et al. 2021, MNRAS, 504, 356

Doran, E. I., Crowther, P. A., de Koter, A., et al. 2013, A&A, 558, A134

Egorov, O. V., Lozinskaya, T. A., Moiseev, A. V., & Smirnov-Pinchukov, G. V. 2018, MNRAS, 478, 3386

Ekström, S. & Georgy, C. 2025, Galaxies, 13, 81

Elmegreen, B. G. & Lada, C. J. 1977, ApJ, 214, 725

Ester, M., Kriegel, H.-P., Sander, J., & Xu, X. 1996, in Proceedings of the Second International Conference on Knowledge Discovery and Data Mining, KDD'96 (AAAI Press), 226–231

Farias, J. P., Offner, S. S. R., Grudić, M. Y., Guszejnov, D., & Rosen, A. L. 2024, MNRAS, 527, 6732

Feigelson, E. D., Getman, K. V., Townsley, L. K., et al. 2011, ApJS, 194, 9

Fuchs, B., Breitschwerdt, D., de Avillez, M. A., Dettbarn, C., & Flynn, C. 2006, MNRAS, 373, 993

Gaia Collaboration, Prusti, T., de Bruijne, J. H. J., et al. 2016, A&A, 595, A1

Gaia Collaboration, Vallenari, A., Brown, A. G. A., et al. 2023, A&A, 674, A1

Getman, K. V., Feigelson, E. D., Kuhn, M. A., et al. 2014, ApJ, 787, 108

Gilmore, G., Randich, S., Asplund, M., et al. 2012, The Messenger, 147, 25

Göppl, C. & Preibisch, T. 2022, A&A, 660, A11

Göppl, C. & Preibisch, T. 2025, A&A, 695, A48

Graciá-Carpio, J., Wetzstein, M., Roussel, H., & PACS Instrument Control Centre Team. 2017, in Astronomical Society of the Pacific Conference Series, Vol. 512, Astronomical Data Analysis Software and Systems XXV, ed. N. P. F. Lorente, K. Shortridge, & R. Wayth, 379

Großschedl, J. E., Alves, J., Meingast, S., & Herbst-Kiss, G. 2021, A&A, 647, A91

Großschedl, J. E., Alves, J., Ratzenböck, S., et al. 2025, arXiv e-prints, arXiv:2509.19487

Gruner, D., Hainich, R., Sander, A. A. C., et al. 2019, A&A, 621, A63

Hamaguchi, K., Corcoran, M. F., Ezoe, Y., et al. 2009, ApJ, 695, L4

Hamann, W. R., Gräfener, G., Liermann, A., et al. 2019, A&A, 625, A57

Hanes, R. J., McSwain, M. V., & Povich, M. S. 2018, AJ, 155, 190

Hao, C. J., Xu, Y., Wu, Z. Y., et al. 2022, A&A, 660, A4

Hayashi, C. 1961, PASJ, 13, 450

Herczeg, G. J. & Hillenbrand, L. A. 2015, ApJ, 808, 23

Holmberg, J. & Flynn, C. 2004, MNRAS, 352, 440

Hourihane, A., Francois, P., Worley, C. C., et al. 2023, VizieR Online Data Catalog, J/A+A/676/A129

Humphreys, R. M. 1978, ApJS, 38, 309

Hunt, E. L. & Reffert, S. 2023, A&A, 673, A114

Hur, H., Lim, B., & Chun, M.-Y. 2023, Journal of Korean Astronomical Society, 56, 97

Hur, H., Park, B.-G., Sung, H., et al. 2015, MNRAS, 446, 3797

Hutschenreuter, S., Alves, J., Posch, L., et al. 2025, arXiv e-prints, arXiv:2509.13607

Iffrig, O. & Hennebelle, P. 2015, A&A, 576, A95

Itrich, D., Testi, L., Beccari, G., et al. 2024, A&A, 685, A100

Jerkstrand, A., Milisavljevic, D., & Müller, B. 2026, in Encyclopedia of Astrophysics, Vol. 2, 639–668

Kang, D. E., Itrich, D., Ksoll, V. F., et al. 2025, A&A, 697, A39

Karim, T. & Mamajek, E. E. 2017, MNRAS, 465, 472

Kennicutt, R. C., J. 1984, ApJ, 287, 116

Kerr, R., Farias, J. P., Prato, L., et al. 2025, ApJ, 985, 111

Kerr, R., Kraus, A. L., Krolikowski, D., Bouma, L. G., & Farias, J. P. 2024, ApJ, 975, 99

Kharchenko, N. V., Piskunov, A. E., Schilbach, E., Röser, S., & Scholz, R. D. 2013, A&A, 558, A53

Kharchenko, N. V., Piskunov, A. E., Schilbach, E., Röser, S., & Scholz, R. D. 2016, A&A, 585, A101

Kim, C.-G. & Ostriker, E. C. 2015, ApJ, 802, 99

Kiminki, M. M. & Smith, N. 2018, MNRAS, 477, 2068

Klaassen, P. D., Reiter, M. R., McLeod, A. F., et al. 2020, MNRAS, 491, 178

Krause, M., Diehl, R., Böhringer, H., Freyberg, M., & Lubos, D. 2014, A&A, 566, A94

Krause, M., Fierlinger, K., Diehl, R., et al. 2013, A&A, 550, A49

Krause, M. G. H., Burkert, A., Diehl, R., et al. 2018, A&A, 619, A120

Krause, M. G. H., Offner, S. S. R., Charbonnel, C., et al. 2020, Space Sci. Rev., 216, 64

Kroupa, P. 2001, MNRAS, 322, 231

Kroupa, P., Weidner, C., Pflamm-Altenburg, J., et al. 2013, in Planets, Stars and Stellar Systems. Volume 5: Galactic Structure and Stellar Populations, ed. T. D. Oswalt & G. Gilmore, Vol. 5, 115

Krumholz, M. R., McKee, C. F., & Bland-Hawthorn, J. 2019, ARA&A, 57, 227

Kuhn, M. A., Feigelson, E. D., Getman, K. V., et al. 2014, ApJ, 787, 107

Kuhn, M. A., Hillenbrand, L. A., Sills, A., Feigelson, E. D., & Getman, K. V. 2019, ApJ, 870, 32

Lee, H.-T. & Chen, W. P. 2009, ApJ, 694, 1423

Leung, H. W., Bovy, J., Mackereth, J. T., et al. 2023, MNRAS, 519, 948

Li, C., Zhao, G., & Yang, C. 2019, ApJ, 872, 205

Lim, B., Nazé, Y., Gosset, E., & Rauw, G. 2019, MNRAS, 490, 440

Lindegren, L., Bastian, U., Biermann, M., et al. 2021, A&A, 649, A4

Lindegren, L., Hernández, J., Bombrun, A., et al. 2018, A&A, 616, A2

Liu, L. & Pang, X. 2019, ApJS, 245, 32

Lloyd Evans, T. 1969, MNRAS, 146, 101

Lucas, W. E., Bonnell, I. A., & Dale, J. E. 2020, MNRAS, 493, 4700

Luhman, K. L. 2018, AJ, 156, 271

Mahy, L. 2026, in Encyclopedia of Astrophysics, Vol. 2, 13–30

Maíz Apellániz, J., Barbá, R. H., Molina Lera, J. A., Lambarri Martínez, A., & Fernández Aranda, R. 2025, in Highlights of Spanish Astrophysics XII, ed. M. Manteiga, F. González-Galindo, A. Labiano-Ortega, M. J. Martínez-González, N. Rea, M. Romero-Gómez, A. Ulla-Miguel, G. Yepes, C. Rodríguez-López, A. Gómez-García, & C. Dafonte, 225

Maíz Apellániz, J., Sana, H., Barbá, R. H., Le Bouquin, J.-B., & Gamen, R. C. 2017, MNRAS, 464, 3561

Martins, F., Schaerer, D., & Hillier, D. J. 2005, A&A, 436, 1049

Melnik, A. M. & Dambis, A. K. 2020, MNRAS, 493, 2339

Mel'Nik, A. M. & Efremov, Y. N. 1995, Astronomy Letters, 21, 10

Micelotta, E. R., Matsuura, M., & Sarangi, A. 2018, Space Sci. Rev., 214, 53

Miret-Roig, N., Alves, J., Ratzenböck, S., et al. 2025, A&A, 694, A60

Miyamoto, M. & Nagai, R. 1975, PASJ, 27, 533

Morel, T., Blazère, A., Semaan, T., et al. 2022, A&A, 665, A108

Navarro, J. F., Frenk, C. S., & White, S. D. M. 1997, ApJ, 490, 493

Oey, M. S., Watson, A. M., Kern, K., & Walth, G. L. 2005, AJ, 129, 393

Ohlendorf, H., Preibisch, T., Gaczkowski, B., et al. 2013, A&A, 552, A14

Olivares, J., Sarro, L. M., Bouy, H., et al. 2020, A&A, 644, A7

Oliveira, R. A. P., Bica, E., & Bonatto, C. 2018, MNRAS, 476, 842

Padmanabhan, T. 2001, Theoretical Astrophysics - Volume 2, Stars and Stellar Systems, Vol. 2

Pang, X., Yu, Z., Tang, S.-Y., et al. 2021, ApJ, 923, 20

Parravano, A., Hollenbach, D. J., & McKee, C. F. 2003, ApJ, 584, 797

Patat, F. & Carraro, G. 2001, MNRAS, 325, 1591

Patrick, L. R. 2026, in Encyclopedia of Astrophysics, Vol. 2, 470–487

Pecaut, M. J. & Mamajek, E. E. 2013, ApJS, 208, 9

Pekruhl, S., Preibisch, T., Schuller, F., & Menten, K. 2013, A&A, 550, A29

Plummer, H. C. 1911, MNRAS, 71, 460

Pöppel, W. G. L., Bajaja, E., Arnal, E. M., & Morras, R. 2010, A&A, 512, A83

Posch, L., Alves, J., Miret-Roig, N., et al. 2025, A&A, 693, A175

Posch, L., Miret-Roig, N., Alves, J., et al. 2023, A&A, 679, L10

Povich, M. S., Maldonado, J. T., Haze Nuñez, E., & Robitaille, T. P. 2019, ApJ, 881, 37

Povich, M. S., Smith, N., Majewski, S. R., et al. 2011, ApJS, 194, 14

Preibisch, T. 2012, Research in Astronomy and Astrophysics, 12, 1

Preibisch, T., Flaischlen, S., Gaczkowski, B., Townsley, L., & Broos, P. 2017, A&A, 605, A85

Preibisch, T., Flaischlen, S., Göppl, C., Ercolano, B., & Roccatagliata, V. 2021, A&A, 648, A34

Preibisch, T., Hodgkin, S., Irwin, M., et al. 2011a, ApJS, 194, 10

Preibisch, T., Mehlhorn, M., Townsley, L., Broos, P., & Ratzka, T. 2014a, A&A, 564, A120

Preibisch, T., Ratzka, T., Kuderna, B., et al. 2011b, A&A, 530, A34

Preibisch, T., Roccatagliata, V., Gaczkowski, B., & Ratzka, T. 2012, A&A, 541, A132

Preibisch, T., Schuller, F., Ohlendorf, H., et al. 2011c, A&A, 525, A92

Preibisch, T., Zeidler, P., Ratzka, T., Roccatagliata, V., & Petr-Gotzens, M. G. 2014b, A&A, 572, A116

Preibisch, T. & Zinnecker, H. 1999, AJ, 117, 2381

Quintana, A. L. & Wright, N. J. 2022, MNRAS, 515, 687

Quintana, A. L., Wright, N. J., & Jeffries, R. D. 2023, MNRAS, 522, 3124

Ramírez-Tannus, M. C., Bik, A., Cuijpers, L., et al. 2023, ApJ, 958, L30

Ramírez-Tannus, M. C., Bik, A., Getman, K. V., et al. 2025, A&A, 701, A139

Rathjen, T.-E., Naab, T., Girichidis, P., et al. 2021, MNRAS, 504, 1039

Ratzenböck, S., Großschedl, J. E., Alves, J., et al. 2023a, A&A, 678, A71

Ratzenböck, S., Großschedl, J. E., Möller, T., et al. 2023b, A&A, 677, A59

Rebolledo, D., Burton, M., Green, A., et al. 2016, MNRAS, 456, 2406

Rebolledo, D., Green, A. J., Burton, M., et al. 2017, MNRAS, 472, 1685

Rebolledo, D., Green, A. J., Burton, M. G., Breen, S. L., & Garay, G. 2021, ApJ, 909, 93

Reed, B. C. 2005, AJ, 130, 1652

Reid, M. J., Menten, K. M., Brunthaler, A., et al. 2019, ApJ, 885, 131

Reid, M. J., Menten, K. M., Zheng, X. W., et al. 2009, ApJ, 700, 137

Reiter, M., Morse, J. A., Smith, N., et al. 2022, MNRAS, 517, 5382

Rosen, A. L., Offner, S. S. R., Sadavoy, S. I., et al. 2020, Space Sci. Rev., 216, 62

Salpeter, E. E. 1955, ApJ, 121, 161

Sanchawala, K., Chen, W.-P., Lee, H.-T., et al. 2007, ApJ, 656, 462

Sander, A. A. C., Hamann, W. R., Todt, H., et al. 2019, A&A, 621, A92

Sander, J., Ester, M., Kriegel, H.-P., & Xu, X. 1998, Data Mining and Knowledge Discovery, 2, 169

Sasaki, M., Robrade, J., Krause, M. G. H., et al. 2024, A&A, 682, A172

Schönrich, R., Binney, J., & Dehnen, W. 2010, MNRAS, 403, 1829

Sellek, A. D., Booth, R. A., & Clarke, C. J. 2020, MNRAS, 492, 1279

Shenar, T. 2026, in Encyclopedia of Astrophysics, Vol. 2, 569–583

Smith, N. 2006a, MNRAS, 367, 763

Smith, N. 2006b, ApJ, 644, 1151

Smith, N. 2014, ARA&A, 52, 487

Smith, N. 2026, in Encyclopedia of Astrophysics, Volume 2, Vol. 2, 508–532

Smith, N. & Brooks, K. J. 2007, MNRAS, 379, 1279

Smith, N. & Brooks, K. J. 2008, ASP Monograph Publications, Vol. 5, The Carina Nebula: A Laboratory for Feedback and Triggered Star Formation, ed. B. Reipurth (Astronomical Society of the Pacific), 138

Smith, N., Egan, M. P., Carey, S., et al. 2000, ApJ, 532, L145

Smith, N., Povich, M. S., Whitney, B. A., et al. 2010, MNRAS, 406, 952

Smith, N., Stassun, K. G., & Bally, J. 2005, AJ, 129, 888

Sota, A., Maíz Apellániz, J., Morrell, N. I., et al. 2014, ApJS, 211, 10

Strawn, E., Richardson, N. D., Moffat, A. F. J., et al. 2023, MNRAS, 519, 5882

Tarricq, Y., Soubiran, C., Casamiquela, L., et al. 2021, A&A, 647, A19

Townsley, L. K., Broos, P. S., Chu, Y.-H., et al. 2011a, ApJS, 194, 15

Townsley, L. K., Broos, P. S., Corcoran, M. F., et al. 2011b, ApJS, 194, 1

Turner, D. G. 1978, AJ, 83, 1081

Ulla, A., Creevey, O. L., Álvarez, M. A., et al. 2022, Gaia DR3 documentation Chapter 11: Astrophysical parameters, Gaia DR3 documentation, European Space Agency; Gaia Data Processing and Analysis Consortium.

van Leeuwen, F. 2009, A&A, 497, 209

Žerjal, M., Ireland, M. J., Crundall, T. D., Krumholz, M. R., & Rains, A. D. 2023, MNRAS, 519, 3992

Wang, J., Feigelson, E. D., Townsley, L. K., et al. 2011, ApJS, 194, 11

Ward, J. L., Kruijssen, J. M. D., & Rix, H.-W. 2020, MNRAS, 495, 663

Weidner, C., Kroupa, P., & Pflamm-Altenburg, J. 2013, MNRAS, 434, 84

Winter, A. J. & Haworth, T. J. 2022, European Physical Journal Plus, 137, 1132

Wolk, S. J., Broos, P. S., Getman, K. V., et al. 2011, ApJS, 194, 12

Wright, N. J. 2020, New A Rev., 90, 101549

Wright, N. J., Drew, J. E., & Mohr-Smith, M. 2015, MNRAS, 449, 741

Wright, N. J., Jeffries, R. D., Jackson, R. J., et al. 2024, MNRAS, 533, 705

Wright, N. J., Kounkel, M., Zari, E., Goodwin, S., & Jeffries, R. D. 2023, in Astronomical Society of the Pacific Conference Series, Vol. 534, Protostars and Planets VII, ed. S. Inutsuka, Y. Aikawa, T. Muto, K. Tomida, & M. Tamura, 129

Yonekura, Y., Asayama, S., Kimura, K., et al. 2005, ApJ, 634, 476

Zari, E., Brown, A. G. A., & de Zeeuw, P. T. 2019, A&A, 628, A123

Zeidler, P., Preibisch, T., Ratzka, T., Roccatagliata, V., & Petr-Gotzens, M. G. 2016, A&A, 585, A49

Zeidler, P., Sabbi, E., Nota, A., et al. 2018, AJ, 156, 211

Zucker, C., Goodman, A. A., Alves, J., et al. 2022, Nature, 601, 334

Zucker, C., Speagle, J. S., Schlafly, E. F., et al. 2020, A&A, 633, A51

ACKNOWLEGDEMENTS

This research was supported by the Excellence Cluster ORIGINS which is funded by the Deutsche Forschungsgemeinschaft (DFG, German Research Foundation) under Germany's Excellence Strategy - EXC-2094 - 390783311. This work has made use of data from the European Space Agency (ESA) mission *Gaia* (`https://www.cosmos.esa.int/gaia`), processed by the *Gaia* Data Processing and Analysis Consortium (DPAC, `https://www.cosmos.esa.int/web/gaia/dpac/consortium`). Funding for the DPAC has been provided by national institutions, in particular the institutions participating in the *Gaia* Multilateral Agreement.

First, I want to thank my supervisor, Thomas Preibisch. Thank you for giving me the opportunity to pursue my PhD and for all of your support and guidance. I'm grateful that your door was always open to me and that you taught me a lot over the last four years.

I would also like to thank Andi Burkert for all your scientific ideas and support, and especially your enthusiasm.

Thank you also to our amazing secretaries for the administrative support.

I would also like to thank all the people at USM who made my time here truly special, in particular Sophie, Adi, Daniel, Thomas, Elena, and Stefan. Thank you for immediately including me as part of the Fun Office and for all our adventures, as well as the amazing trips to Croatia, Japan, Köln, Canada, and Dresden. I will miss the trips to Mensa, our coffee/tea time, and most of all, of course, Cake Wednesday.

Thank you also to my school friends, Alex, Dani, Eva, and Feli. I'm grateful that we are still close friends after all these years and that I could always count on you all. Thank you for all our Thalia evenings and breakfasts, our vacations, and café backup plans. And I'm glad most of you are also doing your PhDs, so I didn't have to suffer alone.

Lastly, I would also like to thank my mother, my father, and my sister. Thank you for always believing in me, especially in times when I didn't believe in myself. Thank you for your endless support; none of this would have been possible without you.